Detecting misfits of the ETAS for seismicity anomalies

Takao Kumazawa
Doctor of Philosophy

Department of Statistical Science
School of Multidisciplinary Sciences
The Graduate University for Advanced Studies

2011

Table of Contents

Ch1. Introduction

1,1 Why in search of anomalies in seismicity

It is a challenging task to predict a coming large earthquake. It is still fresh in our memory that basically none of scholars had ever assumed such a huge earthquake as M9.0 Tohoku-Oki earthquake would have occurred in that region. Besides the complex nature of crustal dynamics that underlies seismogenic faulting, one of the difficulties, in the statistical point of view, of the prediction lies in the limited number of previous precedents. The typical recurrence intervals of major active faults in Japan, for example, ranges from a few to several thousand years [Nomura et al. 2011], some of which earthquakes previously occurred before the history. Unlike weather forecasting, such limitation in the consultable precedents put us into a difficult situation that, if try to forecast an earthquake from seismicity data alone, we are in desperate need of carefully studying every unusual phenomenon which deviates from what we consider as normal. Putting this in other words, studying anomalies in seismicity and accumulating the knowledge from it is the key to understand what has been and will be going on in the ground beneath. There are possibly as many sources of anomalies as one can think of, but we may roughly summarize their qualities into two categories; disturbances from outside, and from inside. The external causes would include volcanic activities, which contaminate data with earthquakes driven by the mechanism different from the normal seismicity of the focal region. Another example is shear stress changes transferred from nearby faulting dynamics. We will explore the latter cause further more in the following section of 1-2. The internal causes would include slow slip events inside the fault of our concern.

In the remainder of this chapter, we review the ETAS model and its treatments. The ETAS model is intensively used in this thesis, hence the good understanding of the model is indispensable. In chapter 2, we extend the ETAS model to have change-points, across which some of the parameters in the ETAS model change. We use this method to examine if there were any anomalies in the seismicity before the 2008 Iwate-Miyagi earthquake of M7.0. In chapter 3, we introduce misfit functions of the ETAS model, and apply them to the cases in which more complicated anomalies are possibly expected.

1-2. Coulomb stress changes

There might be considerable reasons to have regional changes in seismicity. We will investigate the relation between regional changes of seismicity and stress that are caused by abrupt or slow slips in a local region on a fault. *Reasenberg and Simpson* [1992] and *Toda and Stein* [2003] report that changes in seismicity rate correlate with the calculated increment of the Coulomb failure stress:

$$\Delta CFS = \Delta(\textit{shear stress}) - \mu'\Delta(\textit{normal stress})$$

where μ' represents the apparent friction coefficient, and positive normal stress indicates compression. In the paper, we set $\mu' = 0.4$ to minimize the effect of uncertainties and to make ΔCFS patterns stable with respect to changes in μ' [*King et al*., 1994], unless receiver faults are very close to the ruptured fault. The change of Coulomb failure stress in an elastic half-space is calculated by assuming a shear modulus of 3.2×10^{11}dyn cm^{-2} and a Poisson ratio of 0.25 [*Okada*, 1992]. Positive values of ΔCFS promote failure and negative ones inhibit failure. In particular, *Simpson and Reasenberg* [1994] and *Harris* [1998] refer to a region of negative ΔCFS values as 'stress shadow.' Some retrospective case studies [*Ogata et al*., 2003; *Ogata*, 2005, 2006a, 2007, 2010] support the assertion that the stress shadow inhibits normal decay of aftershock activity, i.e., the activity becomes significantly lower than the decay rate predicted by the model.

The rate/state friction law of *Dieterich* [1994] provides the quantitative physical basis of the shadowing and activation of seismicity. For example, it implies that decreasing rate of aftershock occurrence in an aftershock area can be locally accelerated by either the negative ΔCFS due to abrupt slip [*Harris and Simpson*, 1998; *Toda and Stein*, 2003] on a fault or a transient stressing rate decrease due to a slow slip on a fault [*Dieterich et al*., 2000; *Ogata and Toda*, 2010; *Ogata*, 2010]. Numerical simulations based on the rate/state friction also demonstrated the detectable changes in seismicity rate can be reproduced by loading rate changes associated with a slow slip [*Ogata and Toda*, 2010; *Ogata*, 2010].

1,3 Point Process

The seismic activity tends to cluster in its own nature, due mainly to the following

aftershocks. The modeling of such an triggering effect needs to capture the clustering nature, and accordingly various attempts have been tried. The majority of them use (homogeneous) Poisson process to describe the primary events, and let each of the event produce a number of offsprings, or aftershocks. We now introduce briefly the idea and treatments of point process in general. A point process [*Daley and Vere-Jones*, 2003] represents the probability of an event occurrence within a small time interval of length Δ, as

$$\Pr\{N(t,t+\Delta)|\text{event history}\} = \lambda_\theta(t). \qquad (1\text{-}1)$$

Here $N(s,t)$ denotes the number of events in-between time *s* and *t*. The conditional intensity function $\lambda_\theta(t)$ then represents the occurrence rate of an event that depends on the history: the occurrence times and magnitudes of past events. The epidemic type aftershock sequence (ETAS) model [*Ogata,* 1988, 1989] is one of such models, and it has been widely used in the area of modeling seismic sequences. We will introduce the ETAS model in the next section 1-4. In the reminder of this chapter we first cover general treatment for point process analysis.

Provided a sequence of occurrence times of earthquakes coupled with their magnitudes in an observed period $[S,T]$, the parameter set θ are estimated by maximizing the log-likelihood function [*Daley and Vere-Jones*, 2003]

$$\ln L(\theta) = \sum_{\{i:S<t_i<T\}} \ln \lambda_\theta(t_i) - \int_S^T \ln \lambda_\theta(t), \qquad (1\text{-}2)$$

where t_i, represents the occurrence time of the i-th earthquake. We use maximum likelihood estimator (MLE) $\hat{\theta}$ to predict the future occurrence rate $\lambda_{\hat{\theta}}(t)$, $t > T$. *Utsu and Ogata* [1997] detail the computational aspects to obtain the MLE.

To see how the estimated model performs, we use the integrated occurrence rate,

$$\Lambda_{\hat{\theta}}(S,t) = \int_S^t \lambda_{\hat{\theta}}(u)du\,. \qquad (1\text{-}3)$$

This shows the estimated cumulative number of events over the period [*S,t*]. Plotting this together with the observed cumulative number of earthquakes *N*(*S,t*) makes its performance easily seen by the eye. See *Ogata and Shimazaki* [1984], *Matsu'ura* [1986], *Ogata* [1988, 1992, 1999a], *Utsu et al*. [1995] for examples. If we transform the

normal time t intoτso that $\tau = \Lambda(S,t)$, then the sequence of event occurrence $(t_1, t_1, \cdots, t_N)$ is transformed one-to-one into $(\tau_1, \tau_1, \cdots, \tau_N)$. This transformed sequence follows the Poisson process with unit rate, namely, uniformly random distribution on $[0, \Lambda(S,T)]$ if $\Lambda$is that of the true model.

Thus when the estimated rate of earthquake occurrence $\Lambda(S,t)$ approximates well enough the real seismicity, it closely overlaps the observed cumulative counts $N[S,t]$ for t larger than T, in other words $\Lambda_\theta(S,t)$ provides a reliable prediction. In the similar way the transformed sequence of data $(\hat{\tau}_1, \hat{\tau}_1, \cdots, \hat{\tau}_N)$ distributes uniformly over the period $[0, \Lambda_{\hat{\theta}}(S,T)]$ if the estimation is good.

1-4.ETAS model

The ETAS model, first introduced by Ogata [1986, 1988] has the following specific expression;

$$\lambda_\theta(t) = \mu + \sum_{\{i:S<t_i<t\}} K_i (t - t_i + c)^{-p}. \qquad (1\text{-}4)$$

The term $(t - t_i + c)^{-p}$ represents the empirical rule of modified Omori-Utsu formula for aftershock decay. This model treats the case in which an event (earthquake) i that occurring at time t_i triggers its offspring events, hence the seismicity rate at time t is given by the linear superposition of all aftershock effects in its past. The sum is taken for all events i occurred before time t. The constant μ wraps up all the factors of occurrence rate that cannot be explained by aftershock effect of the past available data. The coefficient K_i uses G-R law, i.e., it depends on its magnitude M_i as well as the cut-off magnitude M_z of the data set, in such a way that

$$K_j = K_0 e^{\alpha(M_i - M_z)}. \qquad (1\text{-}5)$$

The parameter set θ thus consists of five elements of (μ, K_0, c, α, p). We have used "Statistical Analysis of Seismicity-updated version (*SASeis2006*)" [*Ogata*, 2006b] to calculate the MLE of θ, and to visualize model performances as well.

Ch.2: Change-point Method

2.1 Introduction to change-point method

At times it is reasonable to believe that one or more of a model's parameters change at certain point in time. In such case treating those parameters independently before and after that point may give better results. Or, we can say the model is improved. Our concern of whether the seismicity changes after some time T_0 in a given period [S, T] is a problem among such model selections, i.e. whether the model fitted separately before and after T_0 then combined together, outperforms the model fitted throughout the period [S, T]. On comparing the performances between models, we consult the Akaike information criterion (AIC) [*Akaike,* 1973, 1974, 1977], described as

$$AIC = -2 \max_{\theta} \ln L(\theta) + 2k , \qquad (2\text{-}1)$$

with k being the number of parameters to be estimated. Under this criterion, the model with smaller value of AIC performs better. Our comparison here is made between the AIC_{12} for the combined model and AIC_0 for the model fitted throughout the whole period. Precisely, we consider following

$$AIC_0 = -2 \max_{\theta_0} \ln L(\theta_0; S, T) + 2k_0$$
$$AIC_1 = -2 \max_{\theta_1} \ln L(\theta_1; S, T_0) + 2k_1$$
$$AIC_2 = -2 \max_{\theta_2} \ln L(\theta_2; T_0, T) + 2k_2$$

and

$$AIC_{12} = AIC_1 + AIC_2 + 2q , \qquad (2\text{-}2)$$

where q represents the degree of freedom imposed on searching the time T_0 based on the data over whole period, and each log likelihood $\ln L(\theta; A, B)$ is to be maximized over the parameter set θ using the data from the time period [A, B]. The minimum of AIC_{12} calculated throughout the target period [A, B] gives the MLE of the change point T_0.

AIC_{12} being smaller than AIC_0 marks the time T_0 as the significant change-point, which means the seismicity pattern has significantly changed across the time T_0. If T_0 is determined independently of the data, in such a case when T_0 is prefixed before the parameter estimation, then q is zero hence comparing AIC_0 with AIC_{12} as the sum of

AIC_1 and AIC_2 alone will tell the significance of the prefixed change-point. Our treatment is otherwise and hence in need of quantifying q. In the next section we will discuss a heuristic evaluation procedure of the penalty q. In our applications to the Iwate-Miyagi earthquakes, we set T_0 at every interval of events, then chose the one that minimize the AIC_{12}, then compared it with the AIC without a change-point.

One may also be interested in the error range of the change-point. Although the standard theory for the MLE error estimate is not applicable to the change-point problem, we can provide confidence intervals in terms of the AIC differences. See section 2-3 for the detail.

2.2 The degree of freedom for a change-point

Assume that a model H_0 is included in a model H_1 that has k extra number of parameters. Then, the large sample theory implies that the likelihood ratio statistic $(-2)\log\left(\hat{L}_0/\hat{L}_1\right)$ distributes according to χ^2_k with degree of freedom k. The penalty term of the AIC is derived based on this property and has the following relationship

$$(-2)\log\left(\hat{L}_0/\hat{L}_1\right) = \mathrm{AIC}(H_0) - \mathrm{AIC}(H_1) + 2k \quad . \qquad (2\text{-}3)$$

However, the ordinary large sample theory cannot be applied to the change-point problem [*Chernoff and Rubin*, 1956]. Therefore, we apply a Monte-Carlo simulation for the likelihood ratio as follows. Simulate uniformly random points on the unit interval [0, 1] with a number $N_1 = N[0, 1]$ as the null hypothesis H_0 (stationary Poisson process), and consider the alternative model H_1 to be uniform distributed in respective separated intervals $[0, T_0]$ and $[T_0, 1]$ with any change-point T_0 (piecewise stationary Poisson processes). Then we calculate the likelihood ratio of the form

$$(-2)\log\left(\hat{L}_0/\hat{L}_1\right) = 2\max_{0<T_0<1}\left[N_{T_0}\log\frac{N_{T_0}}{T_0} + \left\{N_1 - N_{T_0}\right\}\log\frac{N_1 - N_{T_0}}{1-T_0} - 2N_1\log N_1 \right], \qquad (2\text{-}4)$$

with $N_t = N[0, t]$. To see the distribution of the values, we repeat the simulation 10,000 times. For example, the histogram in Fig. 2-01 shows the distribution of

$(-2)\log\left(\hat{L}_0/\hat{L}_1\right)-1$ with N = 1000, which removes one degree of freedom due to the fact that the alternative have the one more occurrence rate for the latter period. It turns out that, unlike the case of the ordinary likelihood ratio statistic, this distribution differs depending on the different number of N on the unit interval [0, 1], and the average of this distribution are given by the ratio of polynomials

$$q(N)=1+\frac{15.325\left(\frac{N}{10}\right)+3.9376\left(\frac{N}{10}\right)^2+0.045644\left(\frac{N}{10}\right)^3}{1+5.0900\left(\frac{N}{10}\right)+0.95595\left(\frac{N}{10}\right)^2+0.0090963\left(\frac{N}{10}\right)^3} \qquad (2\text{-}5)$$

This function is graphed in Fig. 2-02. It is a smoothly increasing concave function that approaches to around 6 with N increases. With the size of data set we dealt with, it ranges from 4 to 5. This Pade approximant in (2-5) is obtained by the least squares of the simulation experiments with the different numbers $10 \le N \le 2000$. We note here that $q(N)$ in *Ogata* [1992, 1999b] includes an error, and should be corrected as the above.

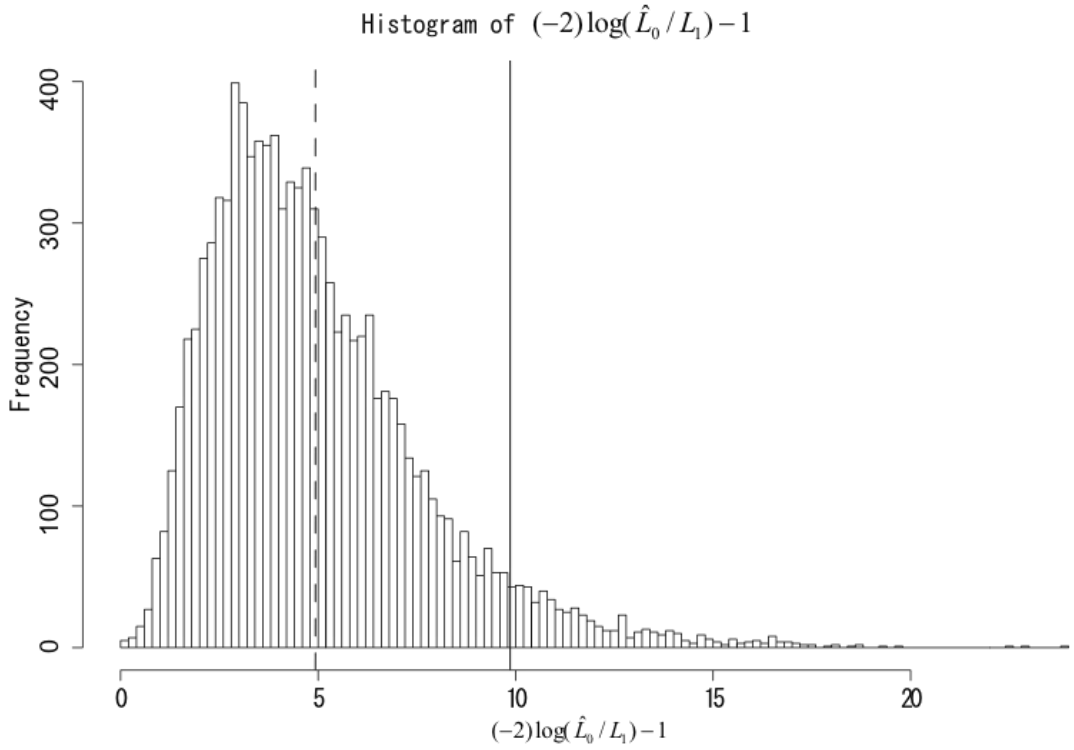

Figure 2-01. The distribution of $(-2)\log\left(\hat{L}_0 / \hat{L}_1\right) - 1$ by simulation, with *N*=1,000. The red line shows their mean. The blue line shows twice the mean, that is, the AIC for the change-point.

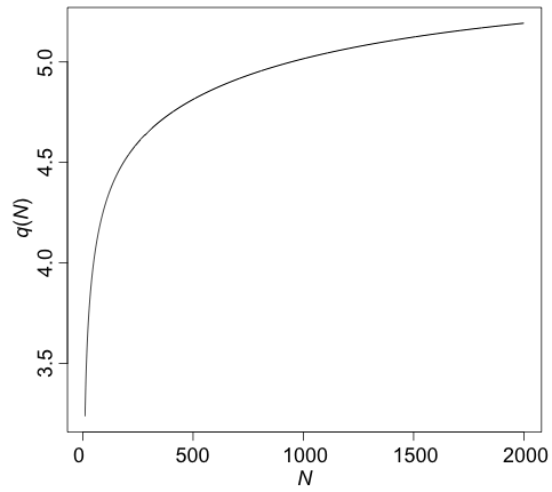

Figure 2-02. A plot of Equation 2-5, with number of events *N* from 10 to 2000.

2-3. Error bound of the change-point estimate

Error bounds of the MLE are calculated by the normal distribution approximation of the likelihood function around the MLE. For example, see *Aki* [1965] for the *b*-value estimate of the magnitude frequency. However, this procedure cannot be applied to the change-point problem [e.g., *Chernoff and Rubin*, 1956]. Alternatively, we calculate them based on the theory from which the AIC is derived. Fundamentally, the AIC is the unbiased estimator of the logarithm of probability getting a future sample (the true) distribution from a predictor [Akaike, 1985], which originally attributed to the idea of the relative entropy by Bortzmann [1878]. It is natural to adopt the most likely model that minimizes the relative entropy for inference. For example, the MLE is the value of parameter that minimizes the relative entropy in case where the parameter dimension is fixed. Therefore, we consider the likelihood of the models with different change-point candidates T_0 in terms of the AICs [e.g., Akaike, 1978a, b], given by $\exp\{-AIC'/2\}$ where the AIC' is defined by $AIC_1 + AIC_2$. The normalization of these likelihoods regarding all T_0 assigns probability mass around the MLE $\hat{T}_0$, which provides error bounds. Unlike the ordinary MLE, the likelihood can be multi-modal, which provides longer error bars.

2-4. Change-point in seismicity

An earthquake rupture transfers stress in neighboring faults, which normally leads to increased off-source seismicity [*Harris and Simpson*, 1998; *Toda and Stein*, 2002]. Seismicity drop-off associated with coseismic stress changes is also found in several cases in which high background seismicity allows us to detect the rate of decrement [e.g., *Toda and Stein*, 2003]. A significant common finding from the majority of stress triggering studies is that seismicity is highly sensitive to small stress changes down to 0.1 bar (0.01 MPa), if these occur in a stepwise fashion. It allows us to forecast roughly the areas where subsequent seismicity activates, and consequently the occurrence of the potential next large shock.

However, such hazard estimates can be computed only after a large earthquake has been observed. Majority of large earthquakes are neither apparently doublet nor clear-triggered events but rather isolated singletons, which nature requires us to seek further tiny signals of triggering that lead a larger event. The important steps are

hence to survey triggering background of a large earthquake by smaller leading events, and also to detect anomalies in seismicity due to stress changes by predictable causes. Many leading works [e.g., *Inouye*, 1965; *Utsu*, 1968; *Ohtake et al*., 1977; *Wyss and Burford*, 1987; *Kisslinger*, 1988; *Keilis-Borok and Malinovskaya*, 1964; *Sekiya*, 1976; *Evison*, 1977; *Sykes and Jaume*, 1990] in fact report anomalies, either quiescence or activation, in seismicity before the occurrence of a large event. Fitting a reasonable model to a seismic sequence then extrapolating or modifying it provides a method to search for such anomalies in seismicity due to stress changes transferred from outside. Specifically, diagnostic analysis with the epidemic-type aftershock sequence (ETAS) model applied to regional seismicity will help in detecting and testing external stress changes [*Ogata et al*., 2003; *Ogata*, 2001, 2004a, 2004b, 2005].

2.5 Application to the 2008 Iwate-Miyagi Nairiku, Japan, earthquake

Our application of this change-point analysis is on the active regions over all northern Honshu, Japan, around the source of the 2008 Iwate-Miyagi earthquake of M7.2 (Mw6.9). This earthquake is thought to have been activated by the preceding two large earthquakes on the Pacific side to the east, which are the 2003 southern Sanriku-coast earthquake of M7.0 (or Miyagi-Ken-Oki earthquake) and the 2003 northern Miyagi-Ken earthquake of M6.2 (see Fig. 1). Both earthquakes raised the Coulomb failure stresses over the NS-trending reverse fault systems in the northern Honshu inland including the fault of our concern [*Ogata*, 2005]. We hypothesize that, years before the 2008 event, slow slips have also been triggered on its own fault plane or its down-dip extension, and then perform statistical diagnostic analysis in line with this.

2-5-1. The 2008 Iwate-Miyagi Nairiku earthquake

The 2008 M7.2 (M_w6.9) Iwate-Miyagi Nairiku, Japan, earthquake occurred on 14 June 2008, in the southern inland Iwate prefecture, around 90km north of Sendai city. There are a number of fault models including by *Asano and Iwata* [2008], *Geographical Survey Institute of Japan* (*GSI*) [2008], *Hirose* [2008], *Ohta et. al.* [2008] and *Takada et al.* [2009]. The common features of these fault models are almost N-S strike angles and reverse fault dipping to the west except that the southern segment of the fault model by *Ohta et. al.* [2008] has significantly different strike angles. Since we will additionally

examine the local stress changes around the source, we adopt the model by *Ohta et. al.* [2008] that uses the geodetic records of the universities' continuous dense array of GPS stations around the rupture source (28stations) in addition to the GEONET stations of the GSI (29 stations). This well agrees not only with the fault model inverted by the strong-motion records [Asano and Iwata, 2008] but also the deformation image obtained by InSAR analysis [Takada, et al., 2009; http://www.aob.geophys.tohoku.ac.jp/info/topics/20080614_news/GPS/].

As described in the above, this earthquake has the mechanism of NS-trending reverse faulting corresponding to EW compressional stress, The source faults extend from Southern Iwate prefecture to Northern Miyagi prefecture in the Northern Honshu (Tohoku District) of Japan. This is the typical mechanism in the northern Honshu inland (North American Plate) due to differential movement between the Eurasian and Pacific plates. Geomorphologic and seismological evidence shows that the majority of earthquake faults within the continental plate in the Tohoku inland region is of dip-slip type and strike approximately North-South [e.g., *Ichikawa*, 1971]. As such the inland of Tohoku District is known to be tectonically homogeneous in the principal stress field.

Under this stress field, *Ogata* [2005] showed that the 26 May 2003 southern Sanriku-coast earthquake of M7.0 enhanced the seismic activity in the region of highly positive ΔCFS values, which includes the present Iwate-Miyagi Nairiku source area. It particularly triggered strong earthquakes in northern Miyagi prefecture. This leads us to a speculation that some aseismic slips were also triggered or enhanced on the source. After some comprehensive matching of the seismicity and stress field in and around the source region in Tohoku District, we have come to hypothesize that aseismic slipping took place only on the southern part of the two fault segments (see Fig. 2-1).

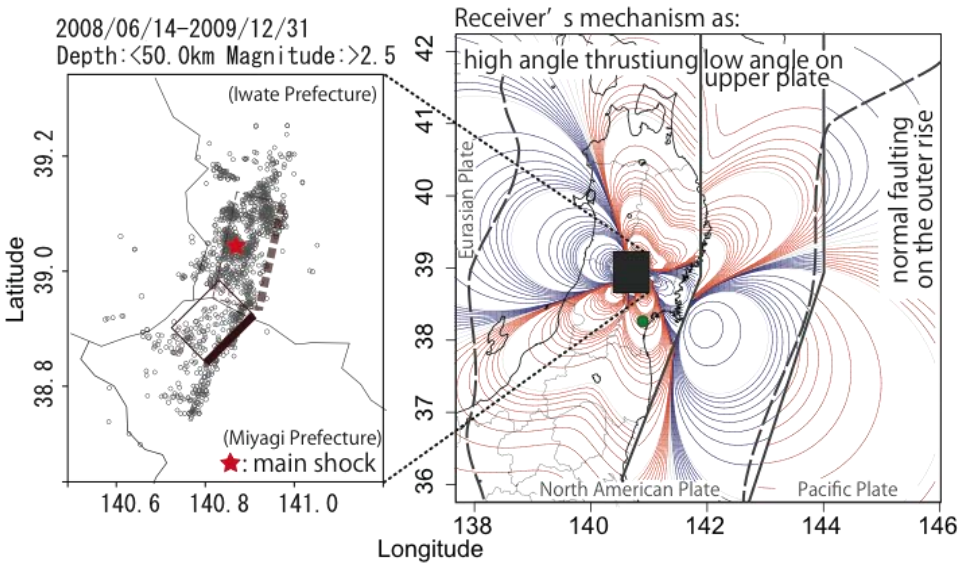

Figure 2-1. Mainshock (red star) and aftershocks (gray circles) of the 2008 Iwate-Miyagi Nairiku earthquake with the fault models (rectangles) by *Ohta et. al,* [2008] (left panel, cf., Table 1) and theoretical stress changes in the far field seismicity zones (right) assuming the southern segment of the fault as the source. The red and blue contours indicate positive and negative CFS increments, respectively, with logarithmically equidistant values due to the assumed slip on the fault as the source (see text in Section 3). The green dot on the right shows the location of Sendai City and the inland lines show prefecture boundaries.

	longitude (east)	***latitude (north)***	***depth (km)***	***length (km)***	***width (km)***	***strike (deg.)***	***dip (deg.)***	***rake (deg.)***	***slip (m)***
Northern	140.979	39.109	0.46	20.57	12.06	195.2	44.9	105.5	1.83
Southern	140.907	38.927	0.40	12.57	10.10	225.3	25.0	80.9	3.53

Table 2-1. The source faults solution of the Iwate-Miyagi prefecture inland earthquake [*Ohta et al*., 2008].

As for the receivers' dominating mechanism in the district, roughly three types of north-south striking fault mechanisms can be considered based on the tectonic environments; that is to say, high angle thrusting in Tohoku inland and Sea of Japan area, low angle thrusting on the upper plate boundary regions on the subducting Pacific Plate and normal faulting in the outer rise regions in the eastern side of the Japan trench (cf.,

Fig. 2-2). Fig. 1 provides the Δ*CFS* in such zones at either the average depth of earthquakes there or along the upper boundary surface of the Pacific plate. Regions of red and blue contours show positive and negative Δ*CFS* values, respectively, in logarithmically equidistant scales. Thus, we tentatively determine the seismicity regions by referring the mapped patterns of Δ*CFS*.

2-5-2. The seismicity zoning around the source

In conducting statistical analysis of seismic activity, we use the Hypocenter Catalog of the Japan Metrological Agency [*JMA*, 2009]. Our objective is to investigate seismicity rate anomalies relative to the ETAS model and their relation to stress changes. To make an analysis using the ETAS model with a stable solution, we should select zones that include enough earthquakes in a closed manner, i.e., having less interaction with seismic activities in other areas. Zone of the seismicity analysis should be set as small as possible in case where it includes an intensive cluster in space, while the zone can be set wider, covering sufficiently many events, in case of the seismicity with spatially uniform or sparse. Furthermore, to explore the relationship between the seismic changes and Δ*CFS* patterns, we only select regions where we can reasonably assume a set of predominant orientations of the receiver fault. Thus, the receiver fault angles of each zone are evaluated in terms of the stress field, alignments of the hypocenters, and the fault mechanisms of past large earthquakes in the region, which are taken from the full-range seismograph network (F-net) catalog of the National Research Institute of Earthquake and Disaster Prevention [*NIED*, 2010].For example, strike, dip, and rake angles can be inferred from the alignments of the hypocenters, focal mechanisms, and active fault orientations, which is mostly consistent with the E–W compressional stress in this region. Fig. 2-2 summarizes those mechanisms in and around northern Honshu island.

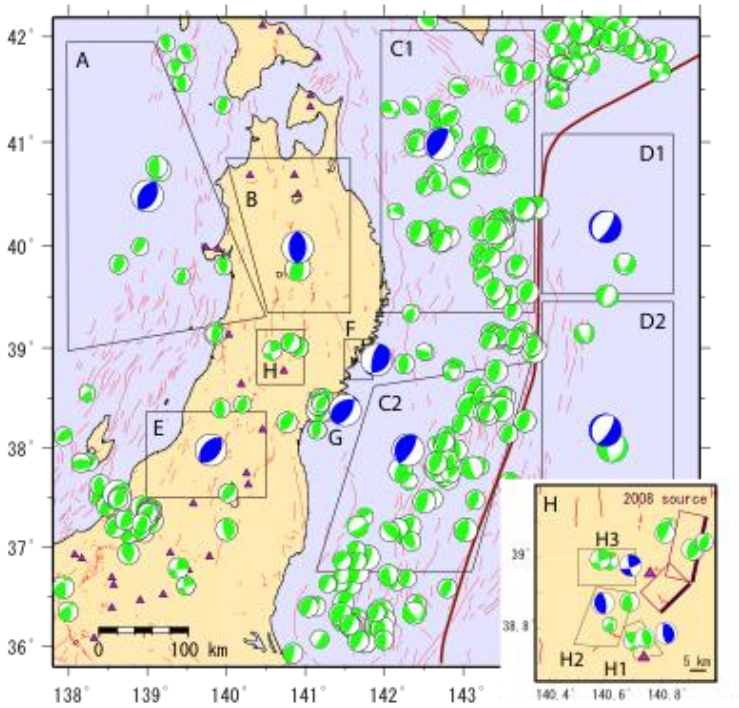

Figure 2-2. The considered polygonal regions of A~H3 with well-determined focal mechanisms for M≥4.5 earthquakes (green beach balls), as covered by the F-net broadband network during the period between January 1997 and June 13 2008 [*NIED*, 2010], and mapped active faults [red lines, *Research Group for Active Faults of Japan*, 1991]. Purple triangles are active volcano, and thick red line is plate boundary. A typical faulting mechanism in each borded region is illusted as a blue beach ball, and listed in Table 2-2. An inset in the bottom right corner is the magnified view of the region H, in which we used the observed mechanisms as the representative ones for H1, H2 and H3 subregions. All determined focal mechanisms (M≥3.5) are plotted in the inset. Note that strike-slip faulting earthquakes in H3 subregion might be associated with heterogeneous crustal structure around volcanoes.

Based on regional differences of faulting mechanisms and characteristics of earthquake occurrence, we defined the nine far-field regions of A ~G as in Fig. 2-2, the regions which are more clearly visualized in Fig. 2-3: (A), seismicity including the aftershocks of the 1983 Central Japan Sea Earthquake of M7.7; (B) and (E), the northern and southern Tohoku inland area relative to the rupture fault, respectively; (C1) and (C2), the northern and southern part of the interplate zone along the subducting Pacific plate, respectively; (D1) and (D2), the northern and southern parts of outer rise area, respectively; (F) and (G), aftershock zones of the M7.0 southern Sanriku-coast

earthquake of 26 May 2003 and the M6.2 Northern Miyagi-Ken earthquake of 26 July 2003, respectively. In addition, the three near field zones H1, H2 and H3 (see magnified map in Fig. 2-2) are selected in view of the clustering of earthquakes, where the stress changes are calculated using the F-net mechanism of the largest earthquake of the activity (see Table 2-2). Table 2-2 lists the receivers' mechanisms (blue beach balls in Fig. 2-2) together with ranges of ΔCFS values for each zone calculated based on the receiver mechanism.

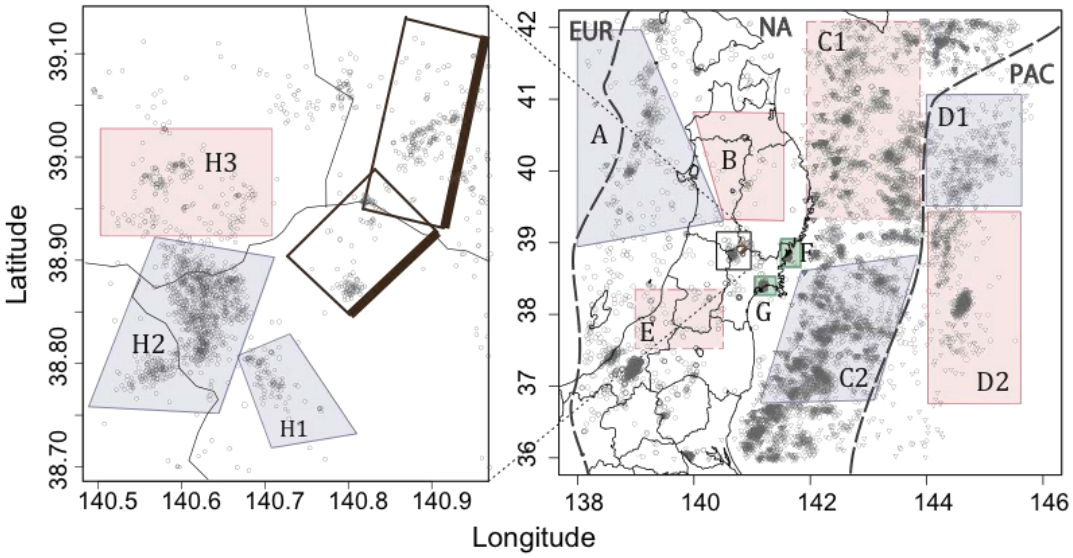

Figure 2-3. The colored polygonal regions of A~H3 as in Fig. 2-2 with earthquakes (gray circles) before the rupture for the ETAS diagnostic analysis. The coloring of each region represents the sign of the dominant ΔCFS assuming the southern segment of the fault as the source; negative for light-blue shaded regions (A, C2, D1, H1, H2), positive for pink shaded regions (B, C1, D2, E, H3), and neutral for green shaded regions (F, G); also see text for the real and dotted boundaries. EUR, NA and PAC represents Eurasian, North American and Pacific plate, respectively.

Region	Strike	Dip	Rake	depth (km)	ΔCFS (mbar)
A	210	45	90	20.0	-7400. ~ -1.4
B	180	45	90	7.5	0.9 ~ 500.
C1	198	20	76	10.~50.	-32. ~ -0.98
C2	198	20	76	10.~50.	0.17 ~ 15.
D1	198	20	-104	10.0	-0.45 ~ -0.093
D2	198	20	-104	10.0	0.30 ~ 3.8
E	220	45	90	10.0	2.8 ~ 54.
F	192	68	73	70.0	-100. ~ 71.
G	243	40	117	15.0	-70. ~ 22.
H1	174	66	101	7.5	-11000. ~ -830.
H2	351	68	90	12.5	-20000. ~ 710.
H3	73	73	168	2.5	-5.0 ~ 540.

Table 2-2. Angles of the receiver's faults and the range of ΔCFS values (5th column) in each region.

We examine the seismic activity in each zone during a roughly 10-year period since October 1997 (see Table 2-3 for the details), also shown in Fig. 2-3. The record of earthquakes with lower threshold of magnitude, listed as M_z in Table 2-3, is taken to be complete throughout the period, by the inspection of the magnitude frequency distribution of the region in comparison with the fitted Gutenberg-Richter's (G-R) law. The detection rate of an earthquake depends on the region; for example, the cut-off magnitude for offshore regions becomes higher than the inland regions. Table 2-3 also summarizes the analyzed results detailed below, based on the methods described in the earlier section. As far as the same G-R law holds throughout the period, we can expect the similar values of the ETAS parameters except for μ and K for the earthquake sequences with different cutoff magnitude M_z [see *Utsu et al*., 1995].

2-5-3. Seismic anomalies in and around northern Honshu

Here we detail the result of our diagnosis with the ETAS model to the selected regions as in Fig. 3, the numerical summary of which are listed in Table 2-3.

Region	*S*	*T*	M_z	*m*	K_0	*c*	*a*	*p*	*AIC0* *AIC1* *+AIC2* *ΔAIC*	*2q(N)*
	10.0	3905.0	2.5	0.138	695.83	0.0074	2.01	0.95	3498.3	
A	10.0	2936.6	2.5	0.129	335.24	0.005	1.82	0.89	3478.1	
	2936.6	3905.0	2.5	0.131	2015.1	0.0024	2.93	1.09	20.2	9.7(899)
	335.9	3907.0	1.5	0.175	1.44	0.0044	1.39	1.13	3186.1	
B	335.9	2203.6	1.5	0.163	3.97	0.0141	1.67	1.24	3140.3	
	2203.6	3907.0	1.5	0.168	0.69	0.0056	0.86	0.97	45.9	9.8(1050)
	100.0	3900.0	4.0	0.058	9.41	0.0041	1.58	0.95	2192.3	
C1	100.0	2475.0	4.0	0.045	8.58	0.0024	1.52	0.86	2189.6	
	2475.0	3900.0	4.0	0.090	5.47	0.0523	2.14	2.53	2.6	9.0(361)
	100.0	3871.0	4.0	0.052	0.298	0.0076	1.51	1.03	1992.0	
C2	100.0	2600.0	4.0	0.057	107.8	0.0066	2.29	0.95	1973.2	
	2600.0	3871.0	4.0	0.039	5.91	0.0051	1.41	1.04	18.7	9.1(369)
	100.0	3898.0	3.0	0.072	12.42	1.863	0.79	1.32	3118.6	
D1	100.0	2752.9	3.0	0.086	20.06	3.295	0.73	1.51	3108.4	
	2752.9	3898.0	3.0	0.063	0.92	0.1086	0.60	1.01	10.2	9.4(548)
	100.0	3882.0	3.0	0.070	544.76	0.1382	1.86	1.19	1105.6	
D2	100.0	2511.2	3.0	0.047	0.2715	0.0601	0.34	0.89	1042.4	
	2511.2	3882.0	3.0	0.058	1480.3	0.1542	2.39	1.11	63.2	9.7(920)
	100.0	4901.0	2.2	0.025	750.43	0.0004	1.84	0.99	1635.2	
E	100.0	2780.0	2.2	0.020	455.52	0.0001	1.70	0.96	1633.4	
	2780.0	4901.0	2.2	0.040	858.73	0.0026	2.01	1.21	1.8	9.4(545)
F	0.1	1983.0	2.5	0.019	803.37	0.0004	2.86	0.91	-1076.3	(1260)
G	0.1	1922.0	2.0	0.012	7.22	0.0194	2.27	1.10	-2761.4	(784)
	200.0	4490.0	1.5	0.013	40.87	0.0018	2.01	1.32	445.0	
H1	200.0	2690.9	1.5	0.016	17.91	0.0008	1.73	1.26	435.6	
	2500.0	4490.0	1.5	0.010	--	--	--	--	9.8	7.9(108)
	1.0	4490.0	1.5	0.000	23.52	0.0287	1.66	1.25	-4830.0	

H2	1.0	1247.6	1.5	0.000	25.21	0.0333	1.68	1.24	-4857.0	
										9.8
	1247.6	4490.0	1.5	0.010	--	--	--	--	26.9	(1048)
	150.0	4404.0	1.5	0.010	1.141	0.0015	0.87	1.15	521.5	
H3	150.0	4086.0	1.5	0.009	0.0133	0.0013	0.00	1.11	492.5	
	4086.0	4404.0	1.5	0.049	2.287	0.0021	1.00	1.22	29.0	8.3(192)

Table 2-3. The MLE and AIC values of the ETAS model.

The data of the region A ~ D are taken for the period from October 1997 till 13 June 2008. The period for the region E is from 1995, the region E from 26 May 2003, the region G from 26 July 2003, and the region H from October 1996, all till 13 June 2008. The S and T represent the periods through which the ETAS model is fitted to each region, counted in days from the beginning of the data period. M_z indicates the cut-off magnitude. For each region except for F and G, the first row lists the result of ETAS model fitted to the entire period, the second row till the change-point, and the third from the change-point. In the AIC column, the first row in each region is AIC_0, the second is $AIC_1 + AIC_2$: the AIC sum of two models separated by a change-point. The third row shows $\Delta AIC = AIC_0 - (AIC_1 + AIC_2)$. The last column shows twice the degree of freedom in searching a change-point (see text and Appendix A). Here, $\Delta AIC > 2q$ indicates that the searched change point is significant.

The Japan Sea region (region A in Fig. 2-3 and 2-4a) is largely in the stress shadow (i.e., the region where ΔCFS is negative). The large cluster of earthquakes dominating the central part of this region consists of aftershocks of the 1983 Central Japan Sea earthquake of M7.7. Therefore, we regard the mainshock fault model [*Kanamori and Astiz*, 1985; see Table 2-2] as the representative receiver fault of this region. The ~150-km NS trending seismic cluster contains large earthquakes of M5.4 and M5.3 that successively occurred on 18 October 2005 associated with a very short-term cluster, after which however the seismicity rate lowered, or became quiet, relative to the predicted rate (Fig. 2-4b and c). This is clearly seen by the lowered slope of the cumulative curve. This seismicity change is significant in terms of AIC as described in Table 2-3. In Fig. 2-5 (a), the solid curve shows the improved amount of AIC by setting a change-point at each interval of events, without taking into account the penalty of searching a change-point (i.e., $AIC_1 + AIC_2 - AIC_0$ by the notation of chapter 2-2). The red horizontal line represents the penalty of searching a change-point from the data

alone. We hence can say any point as a significant change-point as long as the solid curve there is above the red line. Our choices here and the following regions are the ones with the best AICs. Here the change-point with the best AIC is at T=2936.594. The curve in Fig. 2-5 (b) is the scaled AIC, in such a way as

$$\exp\left(-\left(AIC_1 + AIC_2 - AIC_0\right)/2\right),$$

so that it shapes like standard normal around its peak. The error bars in Fig. 2-4 (b) is calculated from this scaled AIC, by regarding it as a probability density.

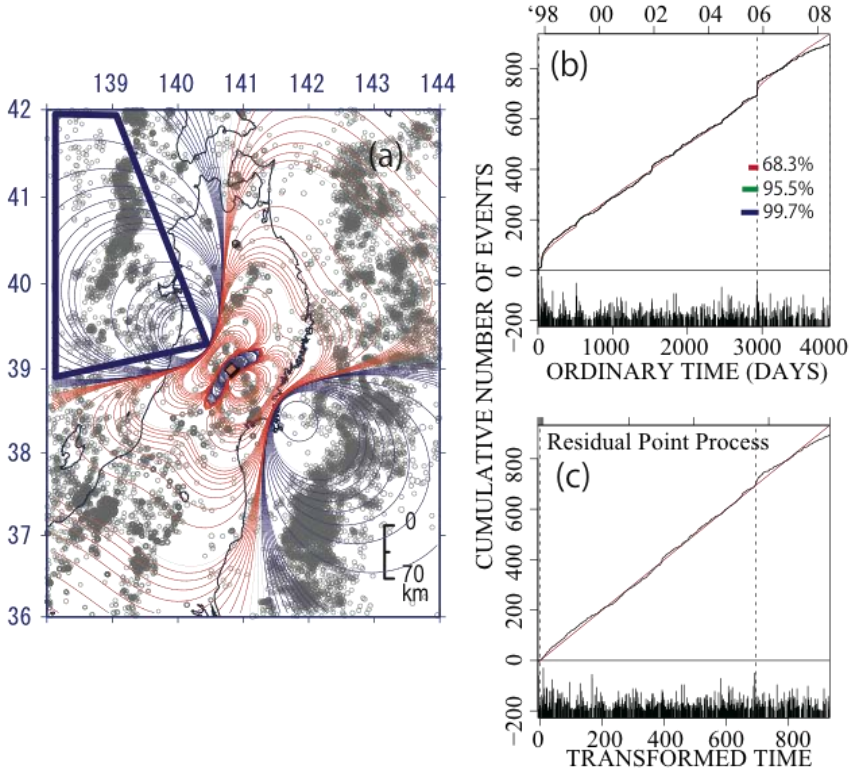

Figure 2-4, a~c. The focal polygonal region in (a) corresponds to A region in Fig. 2. The red and blue contours indicate positive and negative CFS increments (cf., Table 2), respectively, with logarithmically equidistant values due to the assumed slip on the fault as the source (see Table 1 and Fig. 2). The right panels show the empirical (black) and theoretical (red) cumulative curves with respect to regular (b) and transformed (c) time for the occurrence sequence of earthquakes. The theoretical curves (red) are fitted for the period till the change-point (the middle vertical dashed line; see Table 1) then extrapolated to cover the entire period. The colored bars on the panel (b) represent change-point's confidence intervals of 68.3% (red), 95.5% (green) and 99.7% (blue), which are (2804, 2937), (2738, 2937), and (2735, 2937),

respectively.

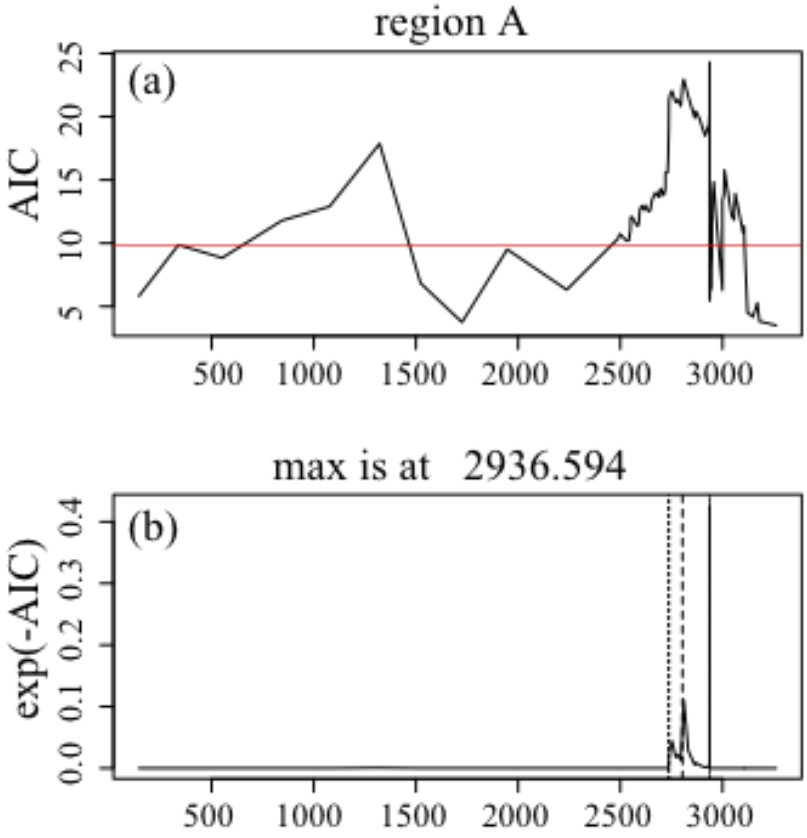

Figure 2-5. (a) The solid curve is the difference of the AIC; $\Delta AIC = AIC_0-(AIC_1+ AIC_2)$, and the red horizontal line is 2q. The unit in horizontal axis is a day. (b) The solid curve is $\exp(-\Delta AIC/2)$. The dashed lines are error boundaries in Fig. 2-4 (b).

The inland area of Aomori and Iwate prefecture (B region in Fig. 2-3, and 2-6 (a)) to the north of the source has positive ΔCFS values throughout the entire region, where we assumed the north-south striking reverse faults for the receivers in the northern Tohoku inland. We fitted the earthquake sequence after September 1998, or T = 330 days from the beginning, till the end to avoid the beginning period of volcanic swarm [*Nishimura et al*., 2001; *Ueki and Miura*, 2002; *Nishimura et al*., 2005] which has very different ETAS parameter values from those of the tectonic seismic activity. In this case, the seismic sequence activated relative to the predicted ETAS rate since the middle of 2003 (see Fig. 2-6 (b) and (c)), which is very significant according to the AIC difference.

As can be seen in Fig. 2-7, a significant change-point ranges wide, with the best being at T=2203.631.

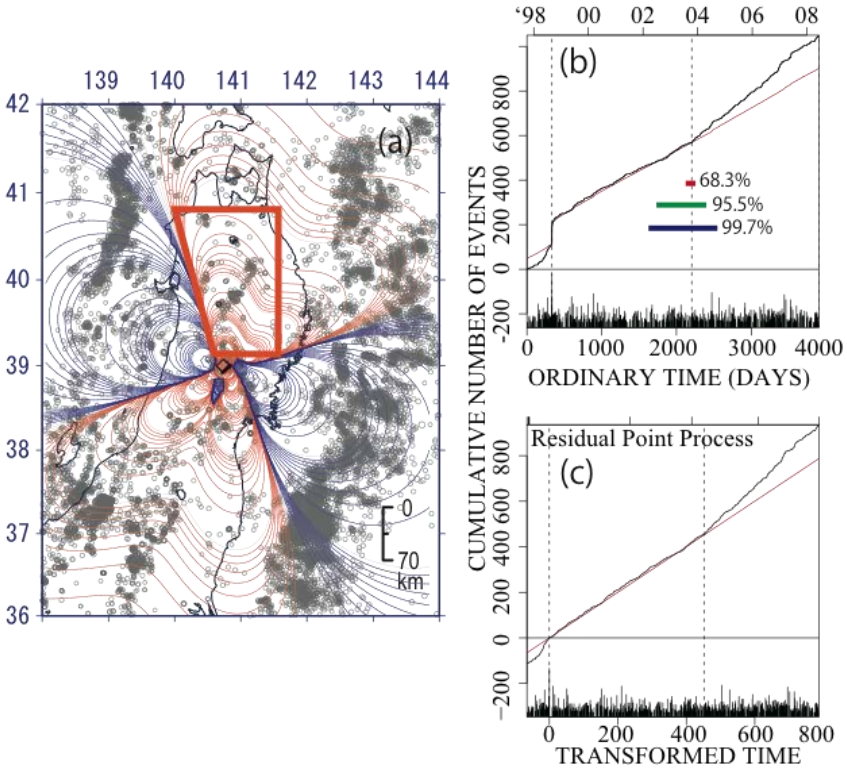

Figure 2-6, a~c. The seismicity in B region, where captions are the same as Fig. 2-2. The colored confidence intervals of 68.3%, 95.5% and 99.7% are (2153, 2259), (1681, 2363) and (1540, 2599), respectively.

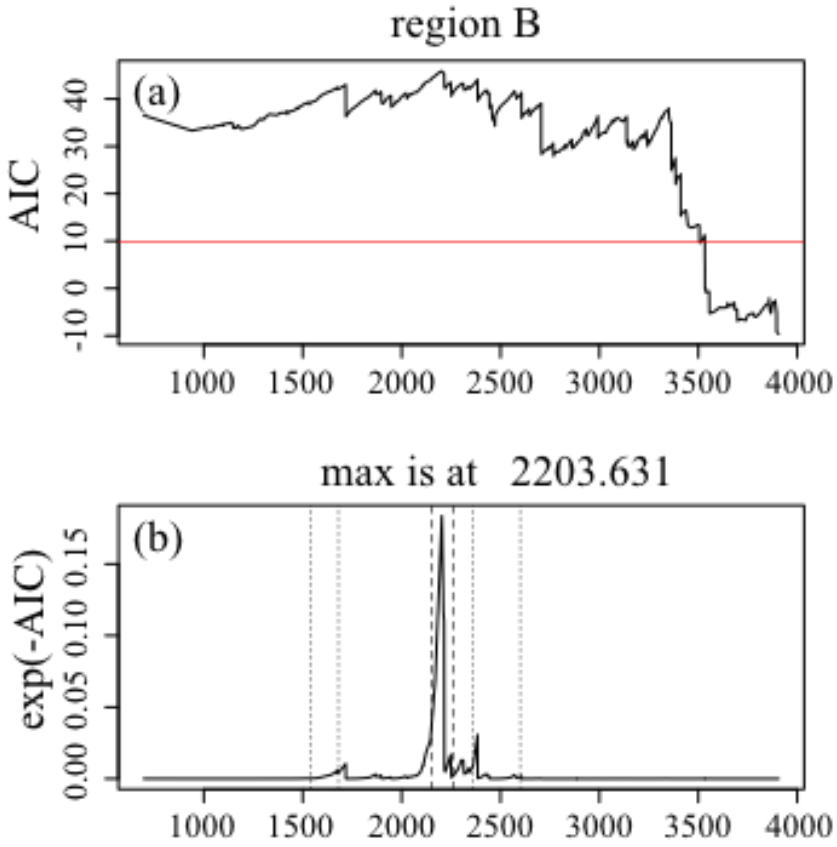

Figure 2-7. (a) The solid curve is $\Delta AIC = AIC_0 - (AIC_1 + AIC_2)$, and the red horizontal line is 2q. (b) The scaled AIC.

In the Pacific upper plate boundary zones (regions C1 and C2 in Fig. 2-3 and 2-8 (a)) and the outer rise zones (regions D1 and D2 in Fig. 2-3 and 2-8 (a)), the seismicity appears to change consistently with the ΔCFS sign, where we assumed typical reverse faulting of the plate boundary and normal faulting in outer rise area, respectively. The activation in the region C1 of Fig. 2-3 is not significant whether or not we take account of the change-point penalty *2q* over whole period (see Fig. 2-9), while the lowering in the region C2 on the other hand is significant in a narrow interval around T=2658.546 (see Fig. 2-10); the observed swarm of around August 2005 (T = 2800 days) in C2 region does not catch up with what the earlier seismicity predicts. Similar patterns can be observed in the outer rise regions of D1 and D2. D1 has a significant change-point within narrow range around T=2752.202, whereas D2 has wide range of significance (Fig. 2-12 and 13). In the region D2 especially the prediction by the earlier seismicity fails to follow the observed swarms at around T = 2900 days. Because of the regions

being offshore, we have to set higher cut-off magnitude, M_z, for these regions than those in inland regions.

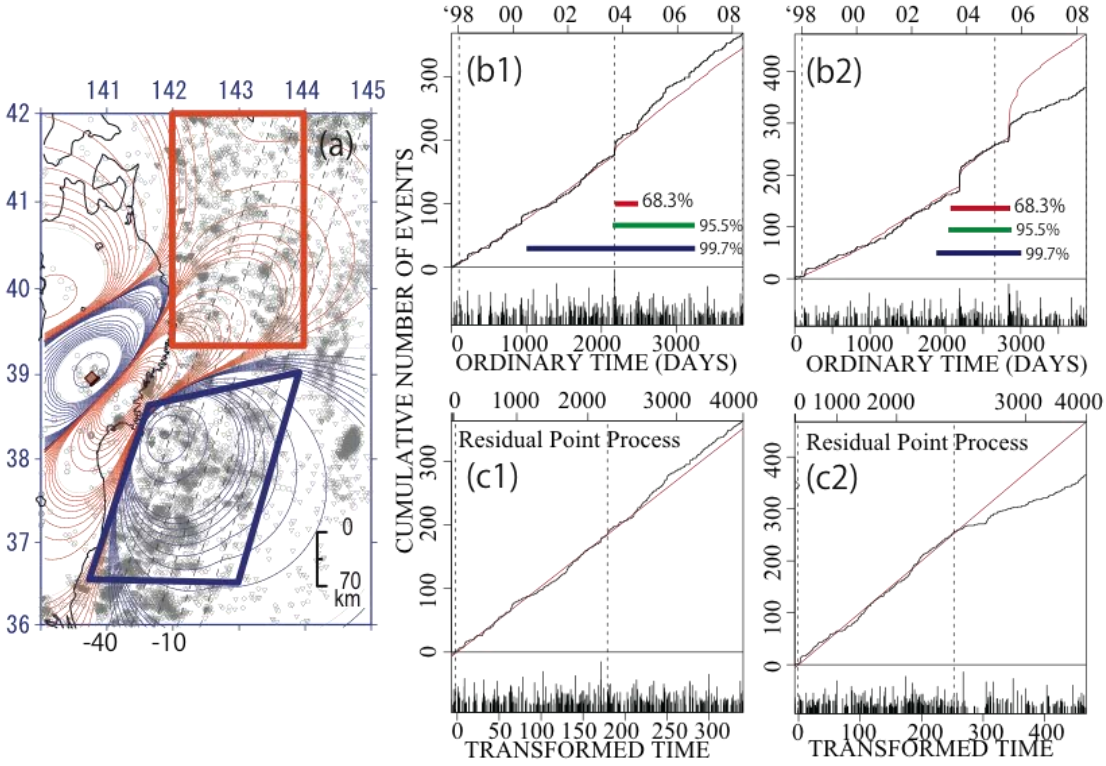

Figure 2-8, a~c. The seismicity in C1 (panel (b1) and (c1)) and C2 (panel (b2) and (c2)) region. The colored confidence intervals of 68.3%, 95.5% and 99.7% for the region C1 are (2209, 2474), (2190, 3327) and (942, 3327), respectively. For the region C2, they are (2006, 2858), (1956, 2867) and (1802, 3019), respectively.

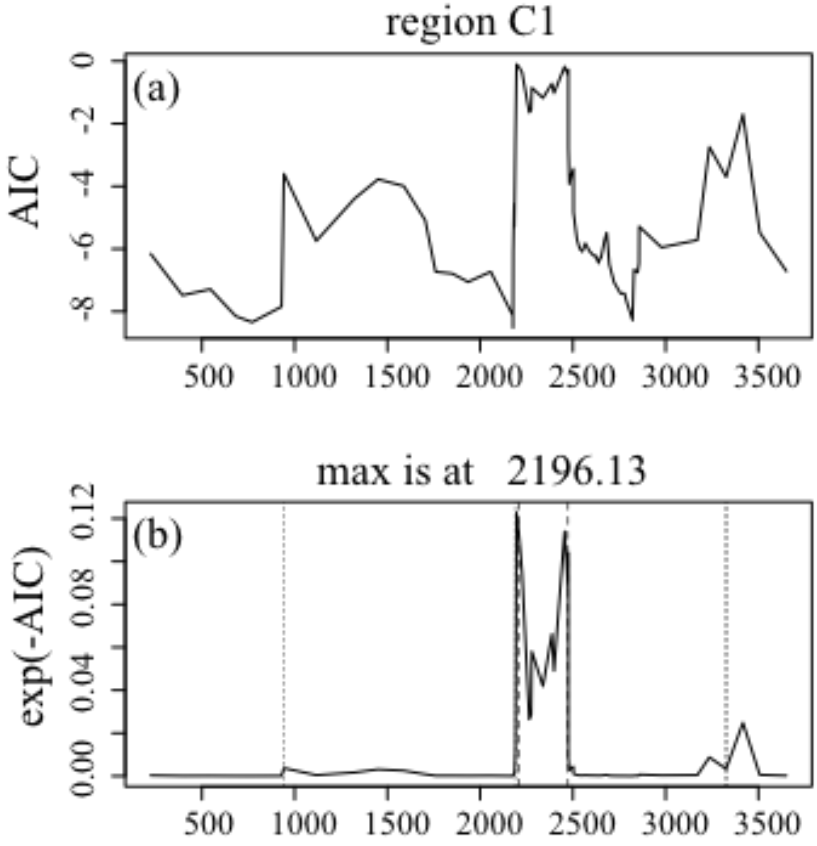

Figure 2-9. The solid curve is $\Delta AIC = AIC_0 - (AIC_1 + AIC_2)$.

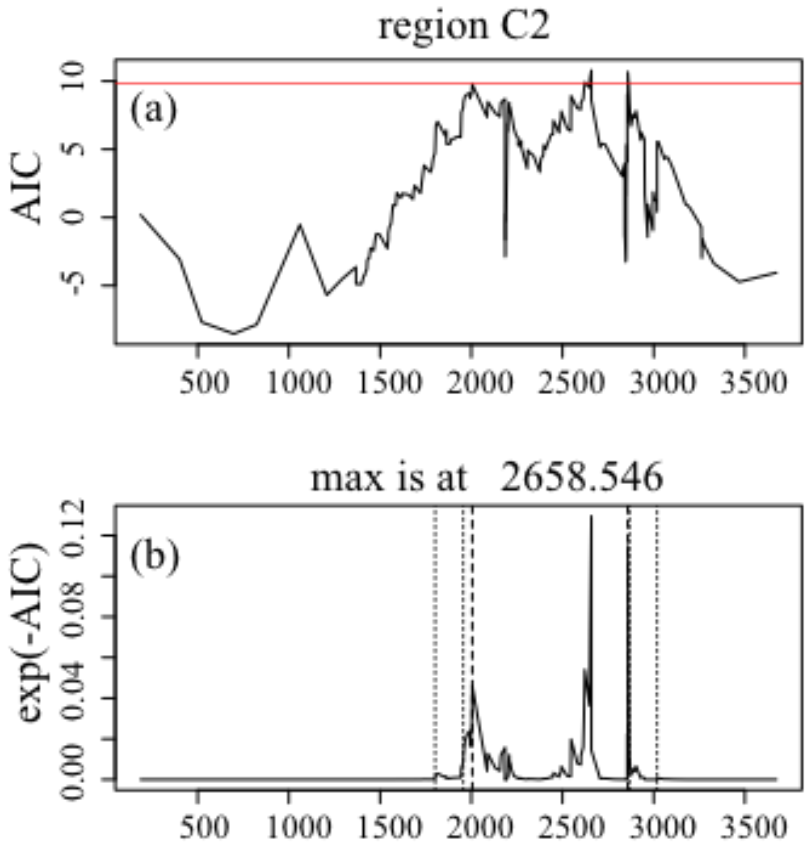

Figure 2-10. The solid curve is $\Delta AIC = AIC_0 - (AIC_1 + AIC_2)$, and the red horizontal line is 2q.

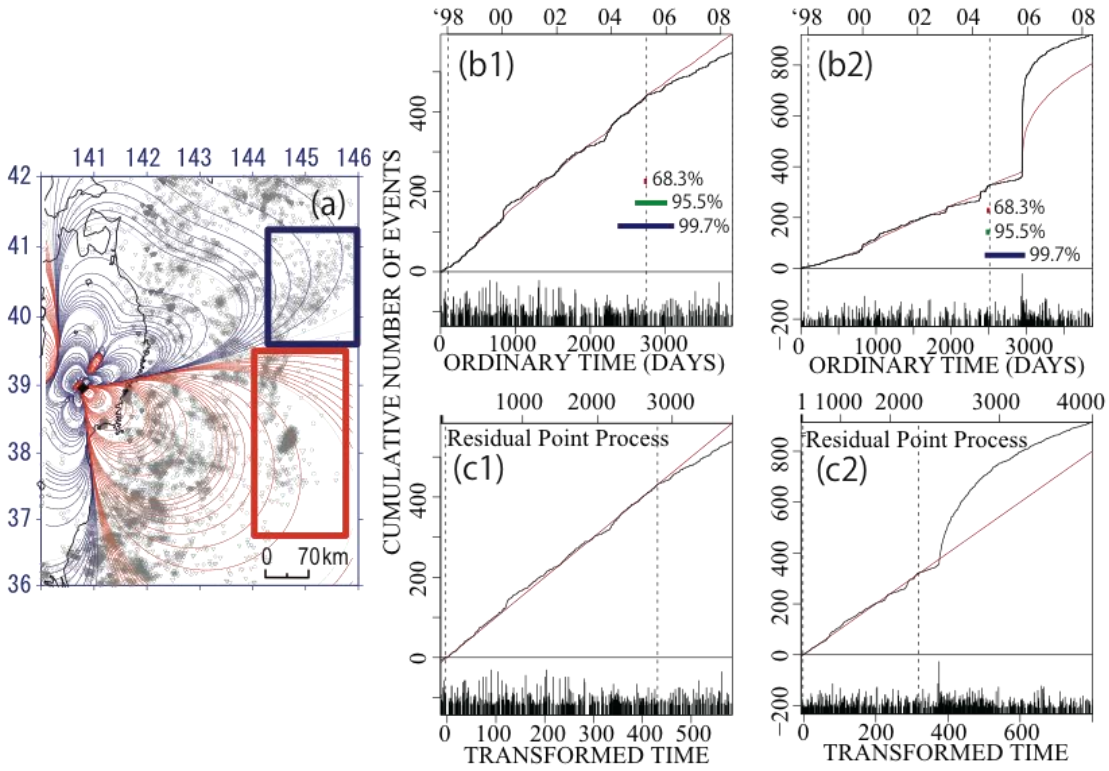

Figure 2-11, a~c. (a) The seismicity in D1(pane l(b1) and (c1)) and D2 (panel (b2) and (c2)) region. The colored confidence intervals of 68.3%, 95.5% and 99.7% for the region D1 are (2739, 2753), (2621, 3025) and (2326, 3132). For the region D2, they are (2511, 2498), (2484, 2511) and (2483, 2936), respectively.

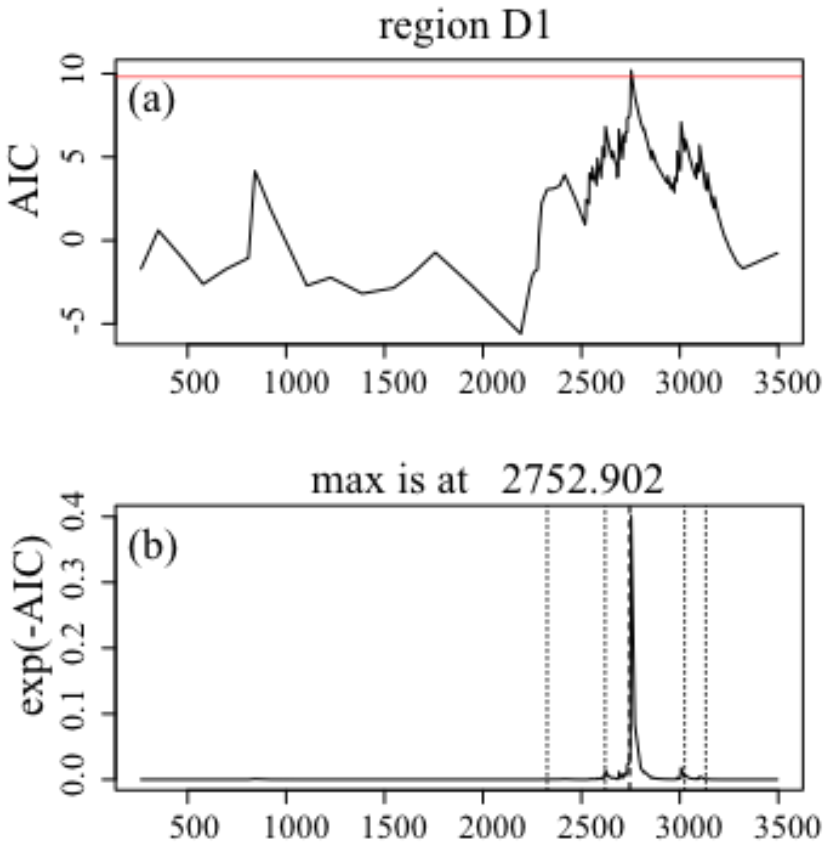

Figure 2-12. The solid curve is $\Delta AIC = AIC_0 - (AIC_1 + AIC_2)$, and the red horizontal line is 2q.

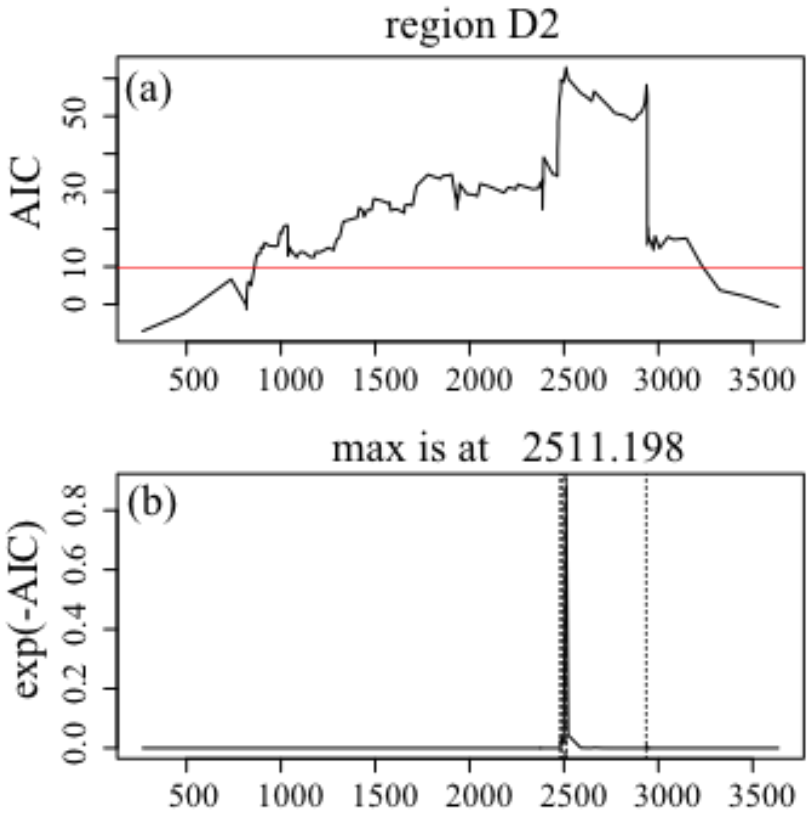

Figure 2-13. The solid curve is $\Delta AIC = AIC_0 - (AIC_1 + AIC_2)$, and the red horizontal line is 2q.

The southwest neighboring region of the fault (E region in Fig. 2-3 and 2-14 (a)) is also the area where the seismicity is affected by pre-, co- and postseismic slips due to the nearby 2004 Chuetsu Earthquake of Mw6.6 [*Ogata*, 2005]. This region is totally neutral relative to the Chuetsu earthquake source including regions of both positive and negative ΔCFS, but it is entirely positive in ΔCFS relative to the Iwate-Miyagi Nairiku slip. Here we assumed NE-trending reverse faulting as the receiver fault corresponding to the general trend of active faults in this area. However, the ETAS analysis of its change-point effect is not significant in AIC whether or not the change-point penalty of $2q$ is taken into consideration (see Fig. 2-15). We will revisit this problem later, in Ch 2-9.

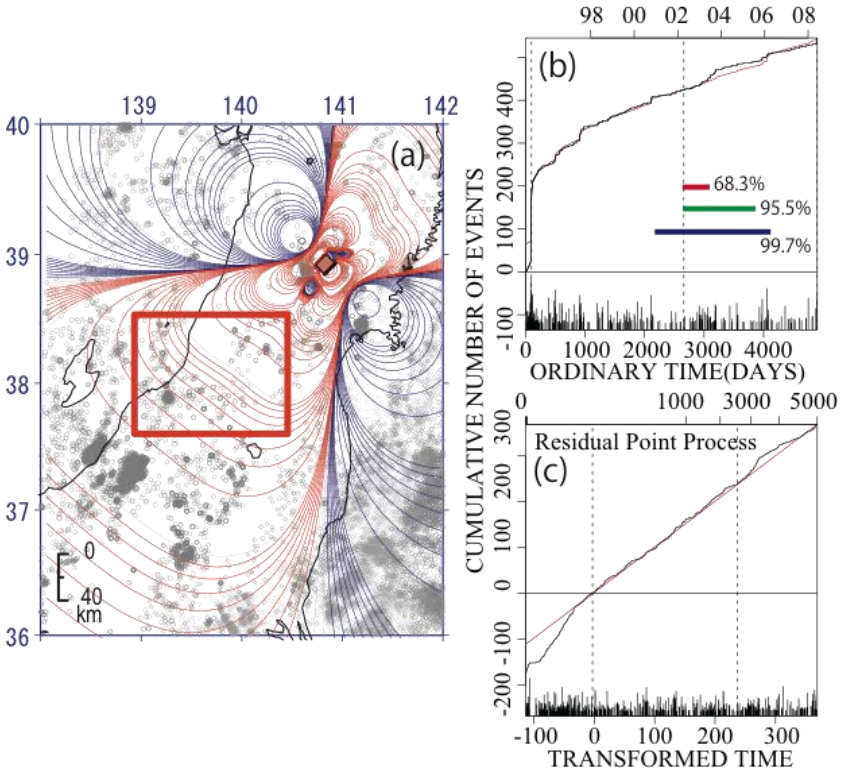

Figure 2-14, a~c. The seismicity in E region. The colored confidence intervals of 68.3%, 95.5% and 99.7% are (2658, 3193), (2658, 3976) and (2101, 4073), respectively.

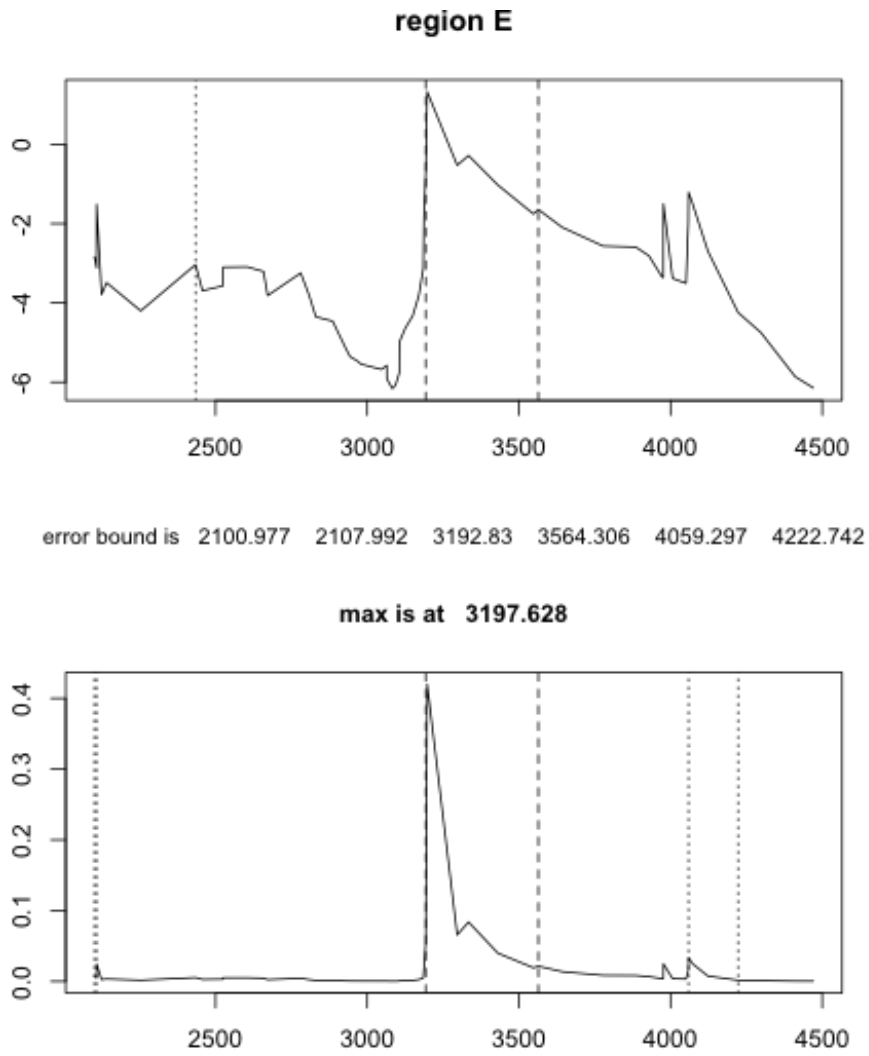

Figure 2-15. The solid curve is $\Delta AIC = AIC_0 - (AIC_1 + AIC_2)$, and the red horizontal line is 2q.

The small regions of F and G of Fig. 2-3 covers major aftershock clusters of the 2003 southern Sanriku coast earthquake of M7.0 (Fig. 2-16 (a)) and northern Miyagi-Ken earthquake of M6.4 (Fig. 2-17 (a)), respectively. For these regions we focus on their aftershock activity. There is no significant change-point since each cluster spreads across or near the boundary of changing sign in ΔCFS: see Table 2-2 and *GSI* [2004] for respective fault angles of the main shock.

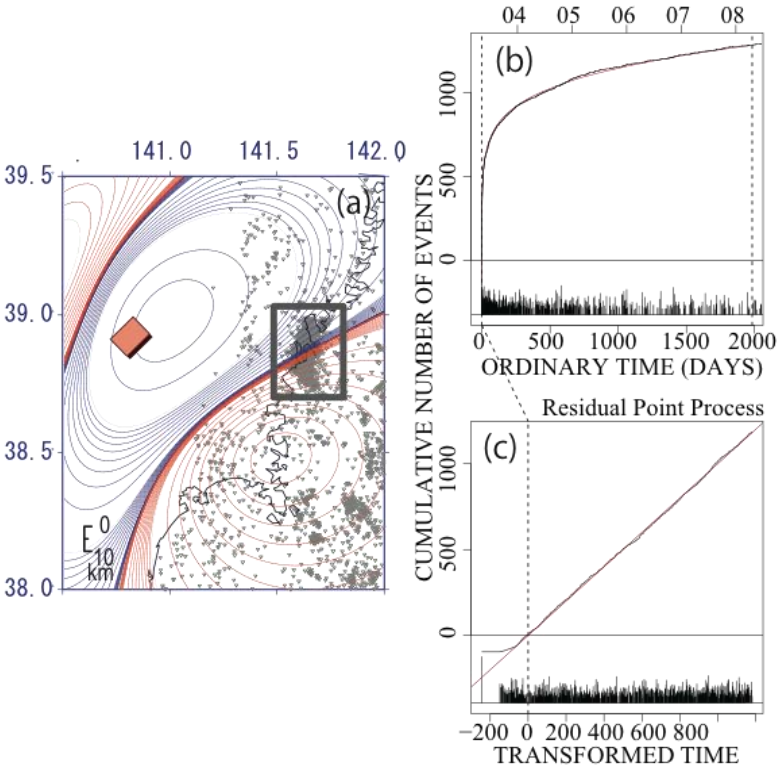

Figure 2-16. The seismicity in F region.

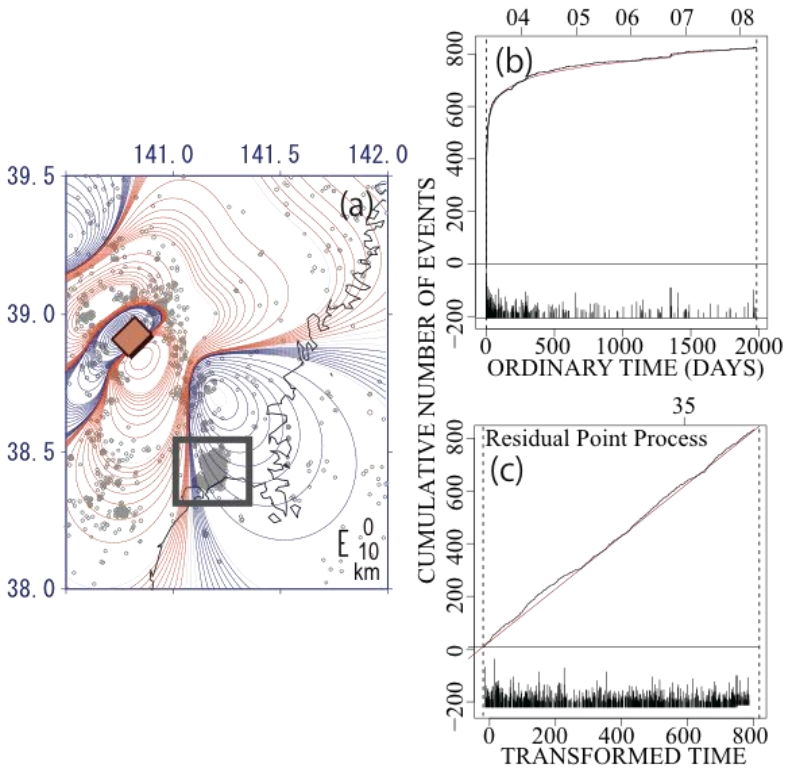

Figure 2-17. The seismicity in G region.

The clusters in the near field to the source can be divided up into three small regions (regions H1, H2, H3 in Fig. 2-3, and 18(a), 20(a), 22(a), respectively), each of which has a unique seismicity change. For the receiver fault angles of each region, we have used a fault mechanism of the largest earthquake available from F-net catalog [see the inset map of Fig. 2-2 and Table 2-2; *NIED*, 2010], and Δ*CFS* pattern does not change much with the alternative conjugate mechanism. Possible high fluid pressure associated with hydrothermal activity in the volcanic regions may have reduced the apparent friction coefficient, but the Δ*CFS* patterns with such low friction still remain similar to those with μ'=0.4 which is assumed throughout the present paper. The clusters in the regions H1 and H2 of Fig. 2-2 fall in stress shadow, and accordingly show quiescence as seen in Fig. 2-18 and 2-20, which are significant in terms of the AIC. The former region has narrow range of significance around T=2690.946, whereas it ranges widely in the latter (Fig. 2-19 and 21). From the extrapolated ETAS cumulative curve after the change-point in Fig. 2-20, the quiescence relative to the theoretical cumulative curve is

hard to see unless the figure is magnified substantially. However, the region has had only a few earthquakes for a long period over 2000 days after 2001, which makes the quiescence very significant in the sense of the AIC difference.

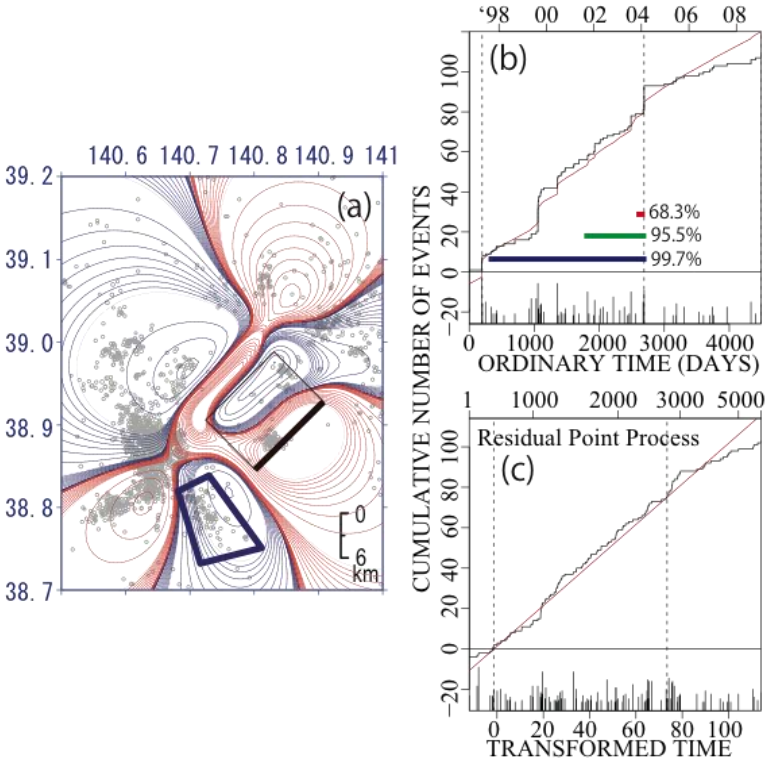

Figure 2-18, a~c. The seismicity for H1 region. The colored confidence intervals of 68.3%, 95.5% and 99.7% are (2563, 2691), (1687, 2691) and (160, 2691), respectively.

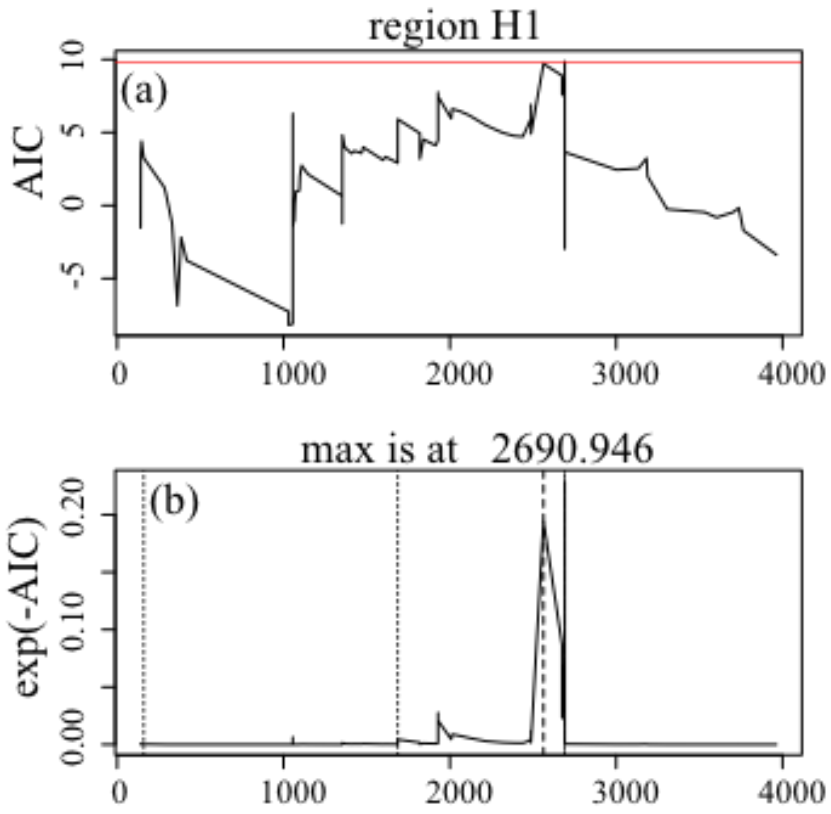

Figure 2-19. The solid curve is $\Delta AIC = AIC_0 - (AIC_1 + AIC_2)$, and the red horizontal line is 2q.

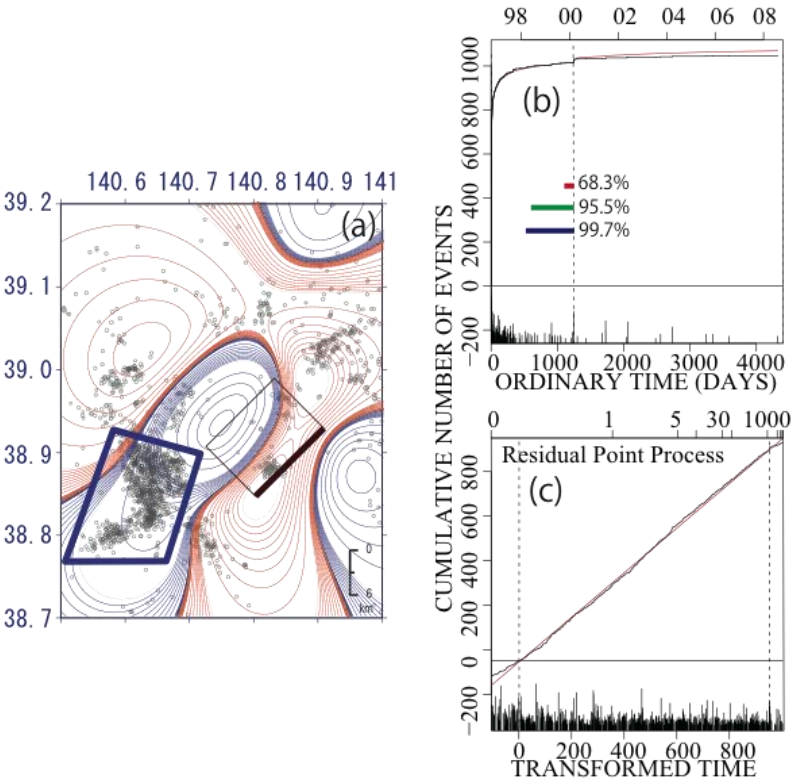

Figure 2-20, a~c. The seismicity in H2 region. The colored confidence intervals of 68.3%, 95.5% and 99.7% are (1053, 1227) and (342, 1227) and (299, 1248), respectively.

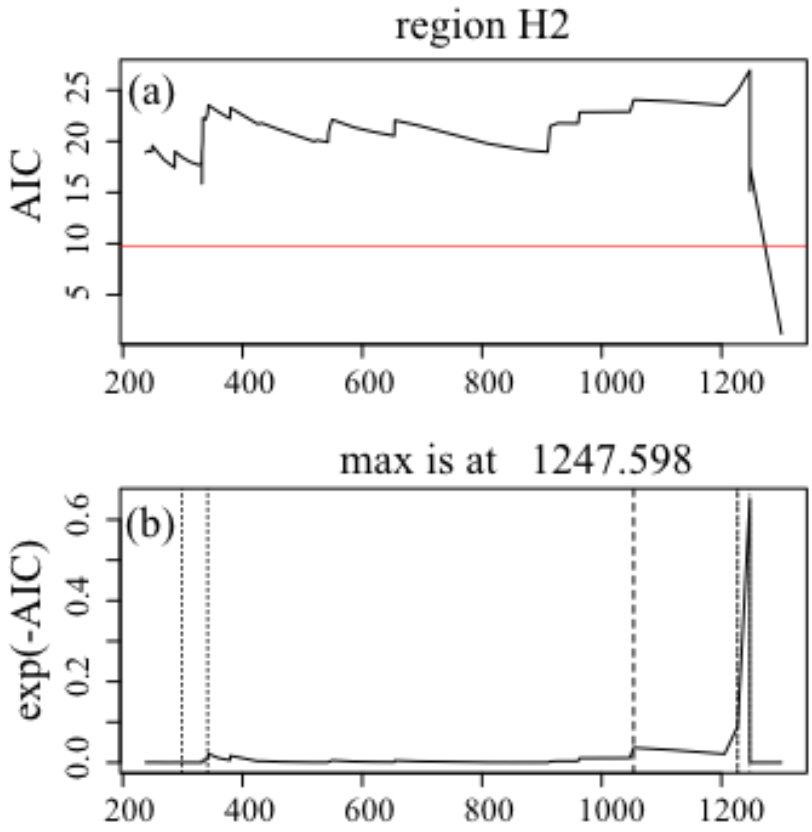

Figure 2-21. The solid curve is $\Delta AIC = AIC_0 - (AIC_1 + AIC_2)$, and the red horizontal line is 2q.

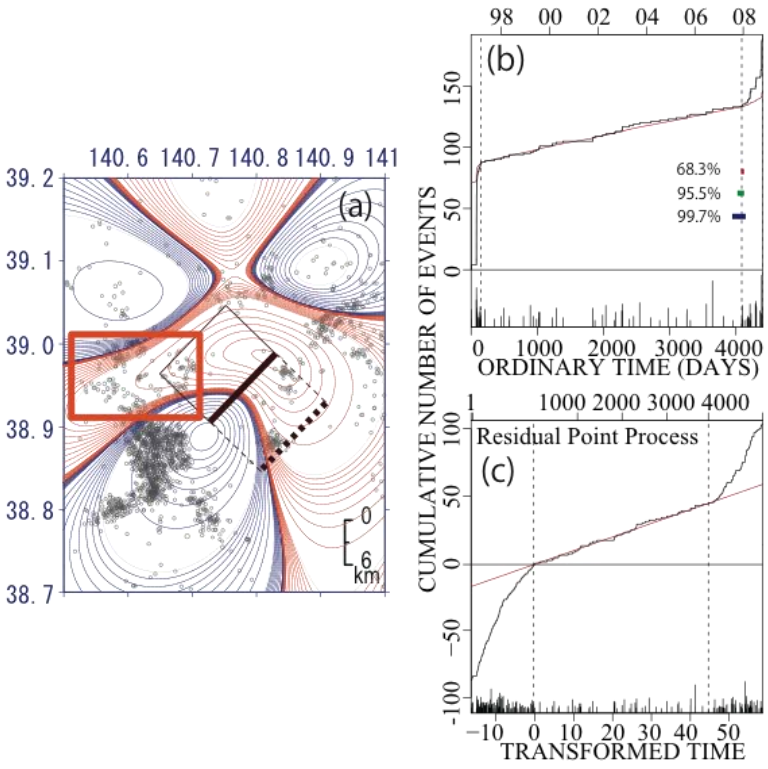

Figure 2-22, a~c. The seismicity in H3 region. The colored confidence intervals of 68.3%, 95.5% and 99.7% are (4087, 4129), (4022, 4168) and (3920, 4198), respectively.

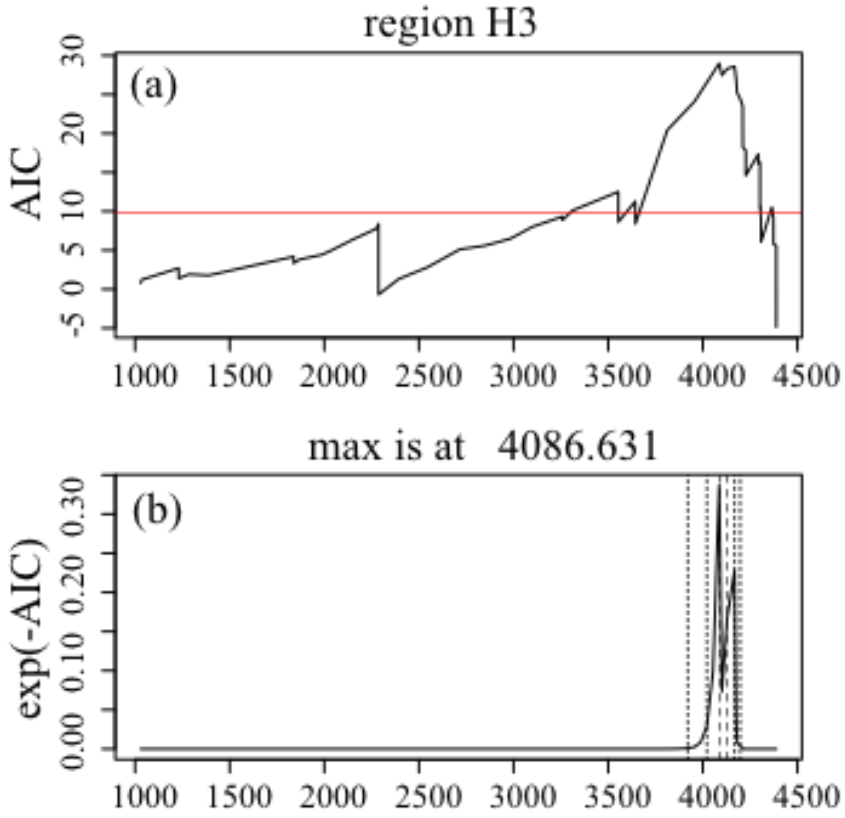

Figure 2-23. The solid curve is $\Delta AIC = AIC_0 - (AIC_1 + AIC_2)$, and the red horizontal line is 2q.

Region H3 has been activated since around 2007 (see Fig.2-22 (b) and (c)) while this region is entirely in stress shadow under the assumed slip (Fig.2-24 (a)). In the figure 2-22(a), we assumed slips in the deeper extension of the southern fragment. We will verify this assumption of slips in deeper extension in the next section, with the observed crustal deformation by GPS network. If we focus on the period before this activation, we see clear quiescence after 150 days from the beginning of 1996. Fig.2-24 (b1) and (c1) show ETAS estimate in [S,T]=[1,150], while (b2) and (c2) show estimate in [S,T]=[82.72, 150]. Both change point at T=150 improves the AIC by 31 and 24.4 respectively. Note that the earlier half of this estimation period, before T=82.72, includes swarm like events, hence including that period or not changes largely the estimated parameters. One observation deserves mentioning; only a few aftershocks followed the M4.4 at around 2006. This is clearly be seen by the extrapolated ETAS fittings and clearly suggests quiescence. Since this region is very close to the source, slight slip may have enough effect on seismicity changes here, while leaving other relatively far regions unaffected. We end this section by adding that this assumption, of

active site having moved deeper along the fault, does not conflict the detected changes in seismicity in the other two nearby regions H1 and H2. Fig.2-25 shows the Δ*CFS* 's in both regions still being in shadow, or neutral.

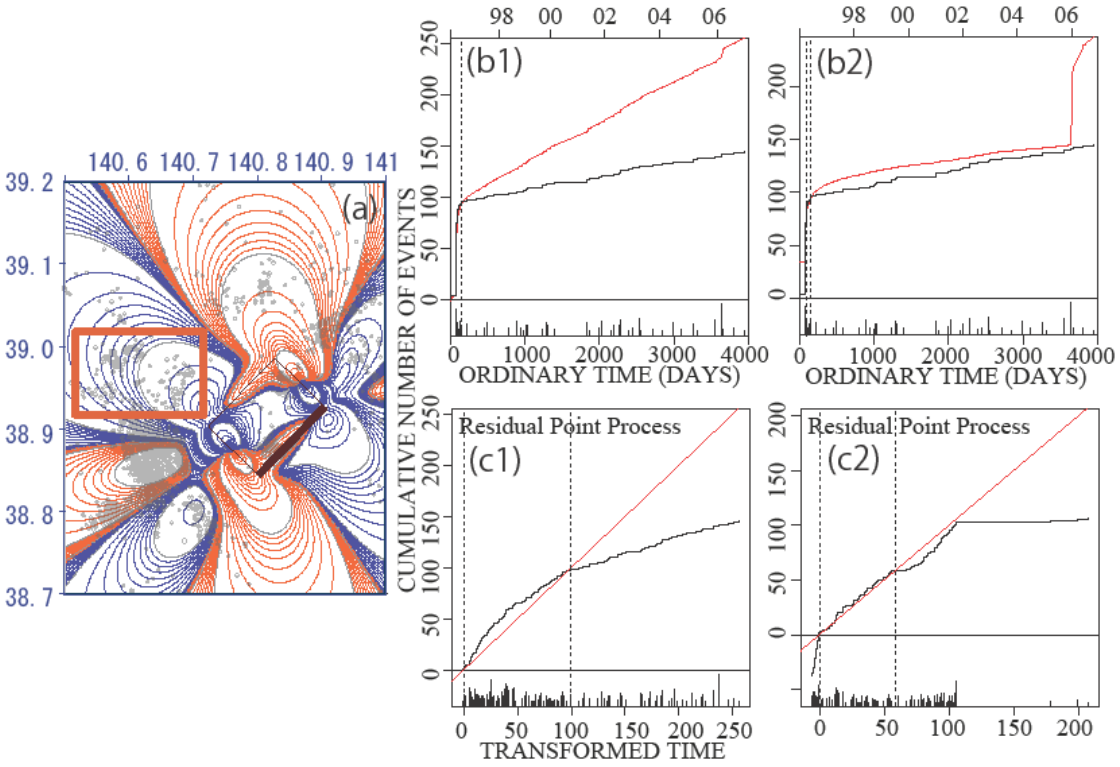

Figure 2-24, (a) ΔCFS is cast by the slips in the southern fragment. (b1,c1) ETAS estimation (red) from from T=1 till T=150, which parameters are (0.0267, 0.0554, 0.0202, 0.936, 1.252). (b2,c2) ETAS estimation (red) from from T=82.72, (after relatively large M3.9) till T=150, which parameters are (0.0, 0.00498, 0.0067, 2.588, 0.957).

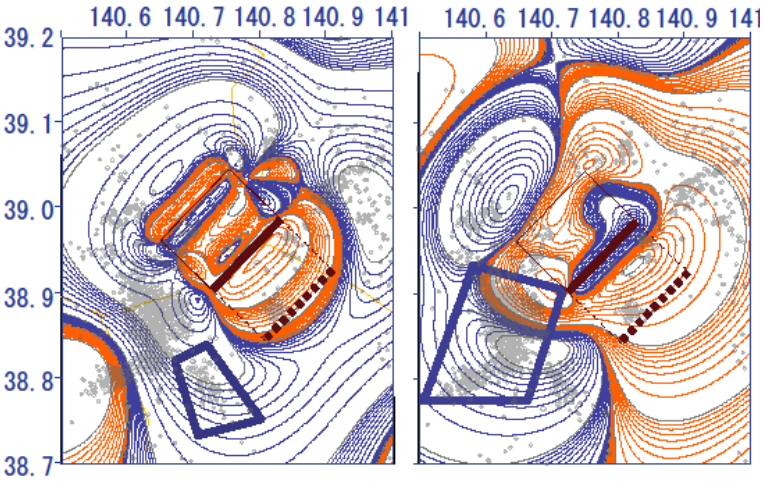

Figure 2-25. Δ*CFS* for H1(left) and H2(right), with the source that of deeper extension of the southern fault.

In summary, the solid blue and red zone boundaries in Fig. 2-3 show significant relative quiescence and activation, while solid greens show activities just as predicted by the single ETAS model. Dashed boundaries show that the anomaly is not significant by the AIC. These results indicate that the seismicity in most zones had changed consistently with the Δ*CFS* calculated from the pre-existing stress field in this region, from several years before the M7.0 occurred.

2-5-4. Crustal deformations by GPS network

The data from the GPS Earth Observation Network System (GEONET) by *the Geographical Survey Institute of Japan* [*GSI*, 2009a] are used to observe the surface deformations. The GEONET stations are located at roughly every 20km, providing their daily coordinates since 1996 for the earliest stations. The data are also sensitive to any non-crustal disturbances such as maintenance on and around the stations, as well as shading by surrounding trees, hence we removed any such disturbances of known causes if found.

In this study, we consider baseline distances between the stations because we expect that the baseline distance, in comparison with the displacement of the station locations relative to a station set as the coordinates origin, can cancel or reduce the various

common effects of wide tectonic crustal movement, so that we can concentrate on the analysis of relative displacements around the source fault.

During a number of years before the focal earthquake, several stations around the considered fault were installed for the purpose of monitoring magma source in volcanic activity. In particular, the station "Kurikoma2" (station H in Table 2-4 and in the inset of Fig. 2-26) is located at the foothills of the Kurikoma volcanic mountain, which turned out to be also right atop the focal fault. During about the same period of our concern with the seismic anomaly, some anomalous displacement of the Kurikoma2 station was observed by the GSI, who suspected volcanic activation beneath the Kurikoma2 station behind this displacement, installed an additional temporary station nearby to confirm the geodetic anomaly [*GSI*, 2008, Internal report for the *Coordinating Committee for Prediction of Volcanic Eruptions* at 8 October 2008; also see *JMA*, 2008].

The data from Kurikoma2 station became available from July 2004, and Fig. 2-26 shows that Kurikoma2 station moved toward southeast relative to its neighboring stations over the earlier 3 years during the period from July 2004 to November 2007. In the inset figure, arrows and numbers represent the average changed distances per year, calculated by using the difference of distances over the periods in Table 2-4 [*Kumazawa et al*., 2009c and d]. Meanwhile, *GSI* [2009b] reported that these particular movements observed at Kurikoma2 were due to neither instrumental error nor very local event such as land slide, by means of the additional observation of the temporary station (green dot in the inset of Fig. 2-26) on another ridge 500 meters east of Kurikoma2. The background for the Kurikoma2 and temporary stations installation was to monitor subterranean volcanic activities around the Kurikoma volcanic mountain. However, no sign of volcanic activity was found even after the June 2008 mainshock [*JMA*, 2008] up to the present. Also, *GSI* [2010] reported, by an independent analysis, that the model [*Kumazawa et al*., 2009a, 2009b] with slip rate of 2 cm/year could explain the transient crustal deformation around this region without the possible volcanic magma migration. Thus, these observations are strong collateral evidence that precursory slips took place in the southern segment.

Station	*Name*	*ID*	*lon(deg.)*	*lat(deg.)*	*Baseline change (mm)*
A	Isawa	970796	140.9885	39.1270	1.8
B	Higashinaruse	20928	140.7150	39.1462	0.8
C	Minase	950193	140.6296	39.0519	6.7
D	Ogachi	20929	140.4473	39.0544	5.0
E	Mogami	20931	140.4973	38.7522	-0.8
F	Naruko	950174	140.8016	38.7489	-3.5
G	Kurikoma	950173	140.9906	38.8153	-9.8
H	Kurikoma2	20913	140.8332	38.9340	
I	Yuzawa	960554	140.5067	39.1991	

Figure 2-4. The focal polygonal region in (a) corresponds to A region in Fig. 2-2. The red and blue contours indicate positive and negative CFS increments (cf., Table 2-2), respectively, with logarithmically equidistant values due to the assumed slip on the fault as the source (see Table 2-1 and Fig. 2-2). The right panels show the empirical (black) and theoretical (red) cumulative curves with respect to regular (b) and transformed (c) time for the occurrence sequence of earthquakes. The theoretical curves (red) are fitted for the period till the change-point (the middle vertical dashed line; see Table 1) then extrapolated to cover the entire period. The colored bars on the panel (b) represent change-point's confidence intervals of 68.3% (red), 95.5% (green) and 99.7% (blue), which are (2804, 2937), (2738, 2937), and (2735, 2937), respectively.

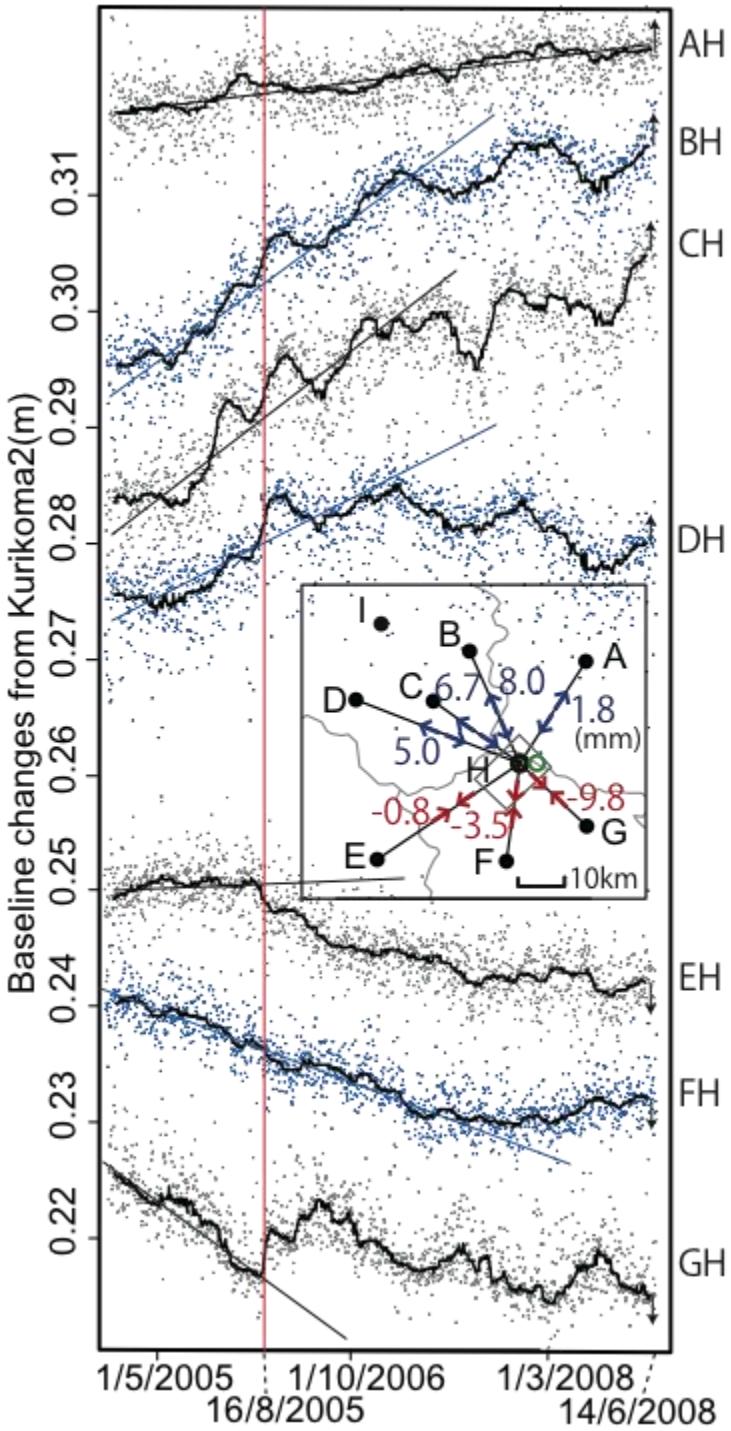

Figure 2-26. Daily time series (grey and blue dots) of the baseline distance changes from Kurikoma2 to each stations in the inset, over 4 years' period from July 2004 till 13 June 2008 (just before the rupture). The details of the stations are listed in Table 2-4. The thick curves link medians of moving window over a month (31 days) of base-line distance changes, and thin straight lines illustrate their linear trends. The vertical red lines correspond to the timing of the 16 Aug 2005 Miyagi-Ken Oki earthquake of M7.1 and

the 14 Jun 2008 Iwate-Miyagi Inland earthquake of M7.2. In the inset map, the numbers between station H (Kurikoma2) and each other station show changed distance in milli-meters per-year during the period with overlaid liner trends, which details are listed in Table 2-4. The right end arrows show the directions of jumps at time of the 2008 mainshock.

Furthermore, Fig. 2-26 also indicates the distance changes within the last two years preceding the mainshock. Notably, the slopes of the linear trends of the baseline distances have changed after around the end of 2006. This is also true for the baseline between Krikoma and Krikoma2, even taking account of the distinct postseismic deformation due to the M7.2 Miyagi-Ken-Oki earthquake of 16 Aug 2005 (the vertical red line in Fig. 2-26). These changes in trends suggest that the movement of Kurikoma2 relative to the surrounding stations either became relatively silent or moved toward northwest which counters their earlier trends. It appears that Kurikoma2 and the southeastern two stations become more stationary, while the northwestern two stations are weakly enhanced to move toward Kurikoma2. Thus the Kurikoma2 station seems to move relatively toward northwest.

2-6. Discussion for change-point analysis

We are concerned with the sign of the *CFS* increment of the region although the ranges of the *CFS* increments are very wide depending on the area size of the region as given in Table 2-2. This paper does not evaluate the quantitative effect of ΔCFS but assumes that there is no threshold value of ΔCFS capable of affecting seismic changes. The stress changes due to aseismic slip can be small values on the order of millibars (10^{-4} MPa) or less, which are comparable to or even smaller than fluctuations in daily earth tides. However, unlike the tidal changes that are oscillatory and too brief to nucleate abundant earthquakes [*Dieterich*, 1988; *Beeler and Lockner*, 2003], this kind of slips is, possibly intermittently, one way. Hence the number of actual and potential earthquakes of small sizes to be triggered or inhibited in a seismic zone can be substantially many to statistically detect significant activation and quiescence relative to the ETAS model in the respective zones under such small Coulomb stress changes.

About the end of Section 5 we reserved the discussion about the conspicuous activation in region H3 during the last one year before the rupture in spite of the stress shadow under the assumed slip on the fault. According to Fig. 2-26, the trends of crustal deformation changed to lie flat at least during the last one year. This would suggest that the slow slip had either ceased or migrated deeper along the fault. In the former case, having the slow slip terminate around an asperity makes the stress shadow disappear in the region H, which can recover or activate the seismicity from quiescence owing to the rate/state friction law of *Dieterich* [1994], as shown in *Ogata* [2010] . For the latter case, Fig. 2-27 shows transition of surface movement assuming the migration of slip toward the down-dip extension of the fault, where we assume 1% slip size of the coseismic main rupture of the Iwate-Miyagi Nairiku earthquake (Table 1) determined in accordance with the observed relative displacement of Kurikoma2 station. This migration consequently drives the positive ΔCFS domain to cover the major cluster of the H3 region, as shown in Fig. 2-22 (a). This assumed migration of slip still provides a consistent ΔCFS pattern (stress shadow) for the seismicity shadow in the regions H1 and H2.

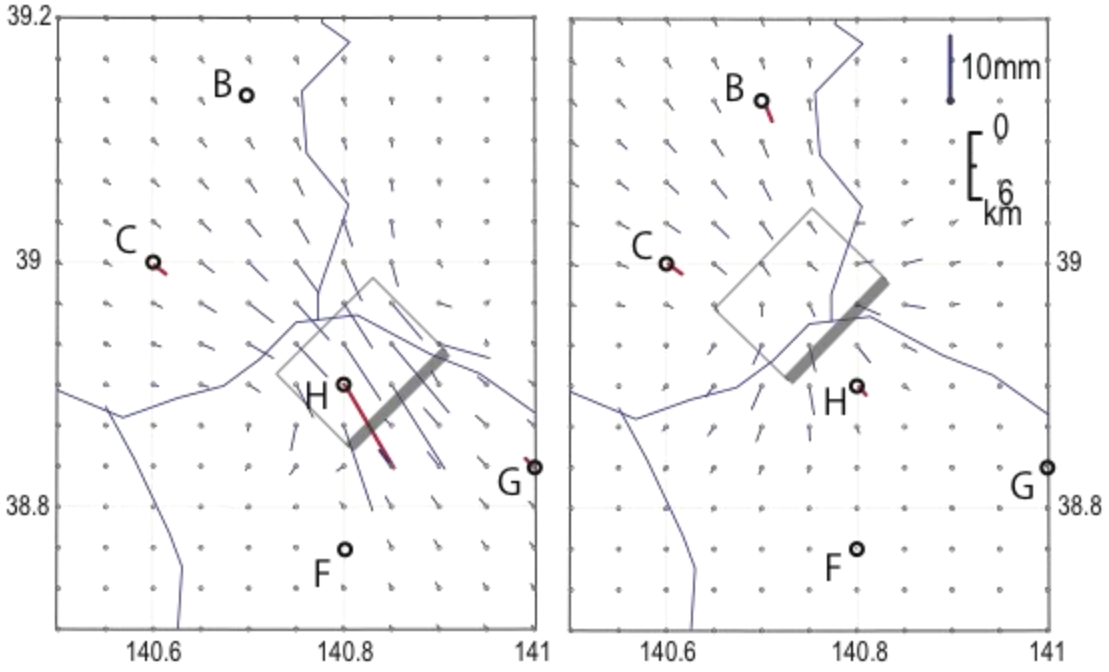

Figure 2-27. Vectors show the theoretical surface movement by assuming the fault (gray rectangle) slip, in the 1/100 scale (see text) of the Iwate-Miyagi Inland earthquake. The rectangle in the left panel represents one of the rupture fault model, and the one in the right panel its down-dip extension. The

GPS stations within the maps are marked by disks and their vectors are in red color.

Incidentally, in Fig. 2-26, we see that the last two months' distance changes of the perpendicular baselines BH, CH, DH and GH to the strike angle of the reverse fault appear synchronized. This could suggest the slip on the fault restarted during the period. Indeed, the seismic activity in region G concurrently becomes quiet.

The result of our diagnostic analysis with the ETAS model is mostly consistent with the stress changes transferred from hypothesized precursory slow slips in the southern part of the coseismic source fault model by *Ohta et al*. [2008]. Besides the normal aftershock activity in regions F and G of the neutral ΔCFS, the seismicity changes are mostly significant in terms of the AIC difference that takes the change-point penalty into consideration. The exceptions are the regions C1 and E which are not quite significant in view of the change-point penalties, on which we comment further below.

We have seen that the change-points of the seismic activities do not fall in a common narrow period; actually these range from 2002 to 2007. One reason for this wide variance may be that the slow slip took place intermittently during the period as is shown by the geodetic records of crustal deformations. Another reason may be that other exogenous stress changes came into play, enhancing or reducing the slow slip on the focal fault or its down-dip extension. At least five large earthquakes occurred that probably had measurable impact in the region. They are, in chronological order, southern Sanriku-coast earthquake of M7.0 (26 May 2003), Northern Miyagi-Ken earthquake of M6.2 (26 July 2003), Tokachi-Oki earthquake of M8.0 (26 September 2003), Chuetsu earthquake of M6.8 (23 October 2004), and Miyagi-Ken Oki earthquake of M7.2 (16 August 2005). Nevertheless, the change-points in many regions overlap during the 2004 - 2006 if we take the error bars of the change-point into account. Although the respective change-point for region C1 and E are not significant enough according to Table 3, their error bars covers such a period. If a change-point is set from the overlapping period, the AIC_{12} value in (7) is given without $2q$, unlike the case where the change-point is searched using its own data (see Section 2.1). This raises the significance of the seismicity changes in the region C1 and E.

We have assumed that aseismic slipping took place only on the southern part of the two fault segments. Neither the northern part of the faults model by *Ohta et al*. [2008] nor the other fault models given in Section 3 can explain the changes in seismic activities for the neighboring clusters in several regions. For example, we consider ΔCFS patterns when the northern segment is assumed as the source. The other fault models have similar strike angles to that of the north fault segment, and thus have similar ΔCFS patterns. Fig. 2-28 shows that the activated regions of H3 falls in stress shadow, and further that the seismicity shadow regions of H1, H2 and the neutral regions of F and G becomes the region of increased CFS. Together with the geodetic anomalies seen only at the Kurikoma2 GPS station as described in Section 6, these observations would suggest that slips on the southern part of the fault are more likely as for the preceding seismic activities.

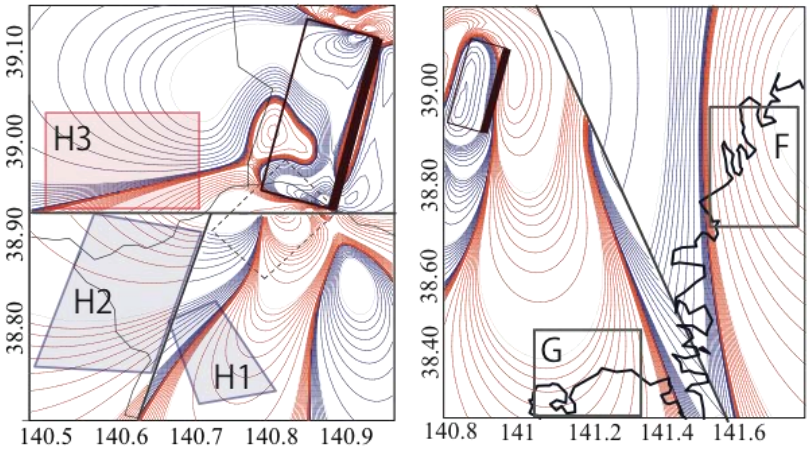

Figure 2-28. ΔCFS assuming the north segment as the source

This study of detecting slow slip events which is precursory of a large shock is probably at the simplest stage, in the sense that we considered only one and the most prominent event as the source of external forces in the stress changes. Further studies with more than one major event taken into account as sources will of course improve and detail the diagnosis, but the conclusion will remain the same; that the ETAS model can be a useful tool to detect stress changes and testing the consistency of a source mechanism with what has been observed in the surrounding regions.

2-7. Conclusion so far

Since the ETAS model predicts an occurrence rate of yet oncoming earthquakes as a function of past occurrence times and magnitudes, it lets us relatively easily see by eye the time at which its prediction deviates from the actual occurrence rate of earthquakes. These observations suggest that even small changes in Coulomb failure stresses do appear as changes in the seismicity. With comprehensive ETAS diagnosis, this then suggests that the sensitivity of the model to the stress changes could provide us with a method in return to estimate and evaluate slip locations.

Using the ETAS model, we have examined seismicity rate changes at the selected regions in and around the northern Honshu (Tohoku District) areas to detect deviations from the expected rates. Such deviations are found in the seismic activities before the 2008 Iwate-Miyagi Inland Earthquake. The deviations are either activation or quiescence relative to the estimated ETAS rate, which agree with the positive and negative increment of CFS caused by the assumed slow slip on the fault that will rupture. The two aftershock activities, where the receiver faults are located in the neutral region, went through normally as predicted by the respective ETAS rates.

These interpretations of the seismicity anomalies are supported by the transient crustal movements around the focal source, namely, the time series of baseline distances between the GPS stations have velocity changes at common time points that are basically consistent with the horizontal displacements of the stations due to the assumed slip, compared to the linear trends due to regular deformation in the stressing field.

The slips on the northern and southern fault and the down-dip extension of the latter fault transfer increasing shear stresses to one another. Hence, in view of our ETAS diagnosis a likely scenario for the sequence of events leading to the 2008 Iwate-Miyagi inland earthquake is that first the precursory slow slips on the southern fault had been enhanced by the preceding two large earthquakes in 2003 on the Pacific side. After migrating deeper, they eventually triggered the rupture starting on the north part of the fault.

2-8. Some afterthoughts (with respect to Tohokuo earthquake of M9.0)

The M=9.0 Tohoku-Chiho Taiheiyo (hereafter, 'Tohoku') earthquake of 11 May 2011 caused considerable crustal deformation throughout wide range of Japan islands as a result of slip on the 500 km long by 200 km wide megathrust source [Wei et al., 2011]. Assuming that there had been precursory slips on the southern part of the fault some years before the events, Ogata [2011] reported that the resulting ΔCFS matches well with the detected activation or quiescence in the regions of A, B, lower half of C, and D. Here we show the ΔCFS assuming that the entire fault had precursory slips (Fig. 2-29), and the pattern of ΔCFS is very close to his. These suggest that we might have looked at the stress transferring effects caused by this, M=9.0 earthquake rather than by the M=7.2 Iwate-Miyagi inland earthquake. Weak or almost no activation in the northern part of our region C can be explained by that the zero boundary of ΔCFS from this source crosses the region. Observing no activation in region E may also be attributed to the ΔCFS by this source.

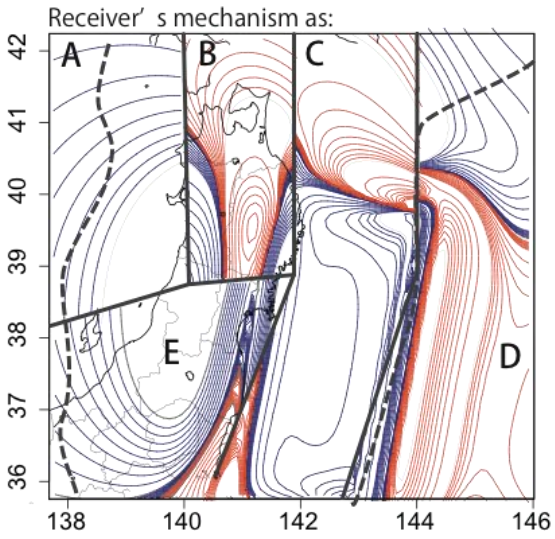

Figure 2-29. ΔCFS assuming by the fault of the Tohoku earthquake.

It probably deserves mentioning some issues on triggering models at this point. We have by far assumed static triggering model described in section 1-2. In static triggering, stress change decays relatively rapidly with distance. This casts suspicion on our finding of seismicity changes in Pacific offshore regions matching well with ΔCFS by Iwate-Miyagi earthquake. The dynamic triggering model does allow such long ranging

triggering, as long as 3600km away (Denali, Alaska earthquake triggering seismicity in the Coso geothermal field in southeastern California; Prejean et al. 2004). The dynamic model assumes triggering by the passage of dynamic seismic wave which decay is much slower. However, our assumption of precursory slow slip as the source does not suit the emission of such far reaching wave. For our “remote triggering”, much simpler explanation is what we speculated above, in the previous paragraph. For the nearby regions to the source, on the other hand, short reaching nature of static triggering enforces our conclusion because no other earthquake with this magnitude in recent years is closer.

Ch.3 Misfit functions

3-1. Introduction to misfit functions

We have so far considered that the physical properties represented by the ETAS parameters remain constant throughout the fitted period, and that they change more or less suddenly only at certain change-points. This simple assumption is quite reasonable in such a case for instance when a triggering event can sharply change the properties of our concern. In the field of seismology, triggering of regional seismicity by nearby large events is a good example. We have seen in the previous chapter that a large earthquake activates or suppresses its surrounding seismicity, by way of transferring Coulomb stress changes through crustal medium.

A problem arises when such stress changes sneak in rather gradually over certain duration of time, accumulate or die off slowly, kick in during too short period of time relative to the whole span of consideration, or even when they come into play so often that dividing entire period into a few is hardly sufficient. We can of course tackle those situations by simply splitting the period into many short fragments and fitting one or more of the parameters separately, as long as the number of data allows such an elaborate task. Although the idea of the change-point method remains simple even in such a case, it becomes more subtle a work to decide where to set change-points. This decision becomes increasingly troublesome with increased number of suspected changes in parameters. To be honest, setting even one change point is often an arbitrary work. For the purpose of getting around those difficulties, hereafter we propose another

triggering, as long as 3600km away (Denali, Alaska earthquake triggering seismicity in the Coso geothermal field in southeastern California; Prejean et al. 2004). The dynamic model assumes triggering by the passage of dynamic seismic wave which decay is much slower. However, our assumption of precursory slow slip as the source does not suit the emission of such far reaching wave. For our “remote triggering”, much simpler explanation is what we speculated above, in the previous paragraph. For the nearby regions to the source, on the other hand, short reaching nature of static triggering enforces our conclusion because no other earthquake with this magnitude in recent years is closer.

Ch.3 Misfit functions

3-1. Introduction to misfit functions

We have so far considered that the physical properties represented by the ETAS parameters remain constant throughout the fitted period, and that they change more or less suddenly only at certain change-points. This simple assumption is quite reasonable in such a case for instance when a triggering event can sharply change the properties of our concern. In the field of seismology, triggering of regional seismicity by nearby large events is a good example. We have seen in the previous chapter that a large earthquake activates or suppresses its surrounding seismicity, by way of transferring Coulomb stress changes through crustal medium.

A problem arises when such stress changes sneak in rather gradually over certain duration of time, accumulate or die off slowly, kick in during too short period of time relative to the whole span of consideration, or even when they come into play so often that dividing entire period into a few is hardly sufficient. We can of course tackle those situations by simply splitting the period into many short fragments and fitting one or more of the parameters separately, as long as the number of data allows such an elaborate task. Although the idea of the change-point method remains simple even in such a case, it becomes more subtle a work to decide where to set change-points. This decision becomes increasingly troublesome with increased number of suspected changes in parameters. To be honest, setting even one change point is often an arbitrary work. For the purpose of getting around those difficulties, hereafter we propose another

way.

Consider a time variant function that measures when and how a given model misfits, or deviates from data. If this reference model reflects what thought to be the normal property of the focal field from which the data come, then the degree of misfit suggests us when (and what kind of, in some sense) anomalies occur. We shall call this time variant function as a 'misfit function'. In the next sections we introduce two different types of misfit functions both of which are specifically linked to the ETAS model.

3-2. Misfit functions

Here we introduce two methods with two different types of misfit functions, namely the multiplicative modifier to the ETAS intensity, and non-homogeneous background seismicity. As those names imply, the misfit here means a modifier that improves the baseline model best under certain criterion (ABIC, for example), within a given framework. Both of the functions estimate the degree of misfits of the referenced ETAS model from the data in their own ways. The methods are built based upon the normal ETAS model.

3-2-1. Misfit function as a multiplier to the intensity function

The first model modifies the ETAS model by multiplying the misfit function $q_{\lambda}(t)$ to the whole intensity function $\lambda(t)$ of the reference ETAS model.

$$\begin{aligned}\hat{\lambda}(t) &= \lambda(t) \times q_{\lambda}(t) \\ &= \left\{ \mu + \sum_{i:t_i<t} K_0 e^{\alpha(M_i - M_z)} \Big/ (t - t_i + c)^p \right\} \times q_{\lambda}(t) \end{aligned} \qquad (3\text{-}1)$$

The misfit function being unity (meaning one) indicates that the reference ETAS model has statistically no misfit. The misfit function $q_{\lambda}(t)$ is smoothed under transformed time line by Bayesian smoothing method. One of the reasons for the time transformation is to reduce the time inhomogeneity.

The idea and procedure is as follows. Suppose we have a reference parameter set $\theta = (\mu, K, c, \alpha, p)$ of the ETAS model at hand. Then the integral of its intensity

$$\Lambda_\theta\left(t|H_t\right)=\int_0^t \lambda_\theta\left(u|H_u\right)du \qquad (3\text{-}2)$$

defined the theoretical cumulative number of events over time interval [0,t]. The time transformation from t to τ,

$$\tau_i = \Lambda\left(t_i|H_i\right) \qquad (3\text{-}3)$$

takes original occurrence time sequence of $(t_1,t_1,\cdots,t_N)$ into the sequence $(\tau_1,\tau_1,\cdots,\tau_N)$ in the transformed time interval [*0,Λ(T)*]. Assume the intensity of the reference model $\lambda_\theta\left(t|H_t\right)$ is a good approximation of the real seismicity, then we can expect its integral $\Lambda_\theta\left(t|H_t\right)$ and the empirical cumulative function $N(t)$ of the event occurrence closely overlap each other. This means the transformed event sequence are uniformly distributed. In general the reference model potentially contains misfits, hence the transformed sequence should be thought to have come from inhomogeneous process. We regard this process being close enough to inhomogeneous Poisson process, and thus we estimate a time variant intensity $\pi(\tau)$ of an inhomogeneous Poisson process by Bayesian smoothing method. This inhomogeneous intensity serves as a multiplicative modifier to the misfits of reference intensity, or as the misfit function on transformed time. Finally, transforming back the time, we obtain $q_\lambda(t) = \pi(\Lambda(t))$.

$$\begin{aligned}\hat{\lambda}\left(t\right) &= \lambda\left(t\right)\times\pi\left(\Lambda\left(t\right)\right)\\ &= \lambda\left(t\right)\times q_\lambda\left(t\right)\end{aligned} \qquad (3\text{-}4)$$

Besides the relative simplicity in smoothing process, the time transformation has another advantage. Because the time transformation distribute events more evenly, with expanding intervals where events are dense and compressing where sparse, the smoothing is operated by , in some sense, rather event-wise than by fixed time unit. This means the resulting misfit function can detect any anomalies within very short period of time as long as the period contains enough number of events.

3-2-2. Misfit function as a time variant parameter

The second method add a simple modification to the ETAS model in such a way that the background seismicity μ now can vary over time while holding other parameters of (K, c,α,p) constant,

$$\hat{\lambda}(t) = \mu(t) + \{\text{triggering terms of the ETAS}\} \quad , \qquad (3\text{-}5)$$

where the background $\mu(t)$ is evaluated at each occurrence time of event. In the same manner as the previous misfit function, we can write background term of the equation 3-5 as;

$$\mu(t) = \mu \times q_{\mu}(t) \quad . \qquad (3\text{-}6)$$

It is well known that the ETAS parameters change over space [Ogata 2003, Chu et. al., 2011 for example], and studies also reported that they change over time [Llenos et. al. 2009, Okutani and Ide 2010]. It is hence a reasonable to introduce time dependence into one or more of the ETAS parameters. It is possible to allow each one of the parameters to vary over time, but our choice in this study is the background seismicity μ, mainly because it is the simplest in terms of modeling, and most likely and largely to change, by the scale of as much as a few order [Llenos et. al. 2009, Okutani and Ide 2010]. If the estimated $\mu(t)$ stays unchanged over the entire period, we can think that the reference ETAS model has statistically no misfit. We use Bayesian smoothing technique to estimate $\mu(t)$ under ordinary time line, unlike the previous method.

This model has difficulty in estimating meaningful misfit functions especially when suspected anomalies occur within too short a period of time compared with the entire period of consideration. This problem will be revisited in later chapter, with simulation experiments.

The introduced two models are thus built upon the "misfit function" $q(t)$'s of the target quantities so that the intensities with them provide better fits. Thus the methods come down to estimate the "$q(t)$'s".

3-2-2. Bayesian smoothing

Our methods need about the same number of parameters as the events, namely q_k's at each occurrence time of event in the form

$$q(t) = \sum_{k=1}^{N} q_k F_k(t) \quad . \qquad (3\text{-}7)$$

Here $q(t)$ represents either $q_{\lambda}(t)$ or $q_{\mu}(t)$, and the q_k's represent the corresponding parameters. $F_k(t)$ is a function that connects neighboring q_k's with straight lines.

Because of this large number of parameters to be estimated, we use penalized log likelihood [Good and Gaskins, 1971], instead of usual log likelihood, to avoid rapid fluctuation in the estimated curve. With the roughness penalty

$$\Phi(q|w) = \int_0^U \left\{ w \left(\frac{dq}{du} \right)^2 \right\} du \qquad (3\text{-}8)$$

where w represents weight parameter controlling the strength of the penalty, our penalized log likelihood becomes as follows;

$$Q(q|w) = \log\{L(q)\} - \Phi(q|w) . \qquad (3\text{-}9)$$

Considering the form of the function $q(t)$ (eq. 3-7), the penalty term Φ has quadratic form with respect to the parameters q with non-negative definite matrix Σ;

$$\Phi(q|w) = \tfrac{1}{2} q \Sigma q^t . \qquad (3\text{-}10)$$

Now considering the prior distribution $\pi(\theta|w)$ characterized by the hyper parameter w be proportionate to $\exp(-\Phi)$, the prior π has multi Gaussian distribution. Since the matrix Σ is degenerate and has rank(Σ) = N-1 (Ogata, 1993), the prior becomes improper. To avoid difficulties, we divide q into (q',q_N) so that the prior below has a finite integral with respect to q';

$$\pi(q'|w, q_N) = \frac{(\det \Sigma')^{1/2}}{\sqrt{2\pi}^{N-1}} e^{\frac{1}{2} q \Sigma q^t} \qquad (3\text{-}11)$$

where Σ' is the cofactor of the last diagonal element of Σ.

The hyper parameters (w, q_N) are then obtained so as to maximize the integral of the posterior with respect to q';

$$\Psi(w, q') = \int L(q)\pi(q|w) dq' . \qquad (3\text{-}12)$$

By using the Gaussian approximation, the logarithm of the integrand of (3-12)

$$\begin{aligned} Q_0(q; w) &= \log[L(q)\pi(q|w)] \\ &= Q(q|w) + \tfrac{1}{2} \log \det \Sigma' - \tfrac{3}{2}(K-1) \log 2\pi \end{aligned} \qquad (3\text{-}13)$$

is approximated by the quadratic form

$$Q_0(q;w) \cong Q_0(\hat{q};w) - \tfrac{1}{2}\left(\theta - \hat{\theta}\right) H\left(\hat{\theta}|w\right)\left(\theta - \hat{\theta}\right)^t \qquad (3\text{-}14)$$

where $\hat{\theta}$ maximize Q_0, or the penalized log-likelihood Q, for a fixed weight. The $H(\hat{\theta} \mid w)$ is the Hessian matrix (second derivatives) of the penalized log likelihood at $\hat{\theta}$;

$$H\left(\hat{\theta}|w\right) = \frac{\partial^2 \log L\left(\hat{\theta}\right)}{\partial\theta\partial\theta^t} - \Sigma\,. \qquad (3\text{-}15)$$

Using the quadratic form (3-14) with (3-15), we have the approximated log Bayesian likelihood;

$$\log \Psi\left(w, q_N\right) = Q_0\left(\hat{q} \mid w\right) - \tfrac{1}{2}\log(\det H) + \tfrac{3N}{2}\log 2\pi\,. \qquad (3\text{-}16)$$

Now optimizing (3-9) with respect to *q'* and (3-16) with respect to (w,q_N) in turn achieves our objective. This method is largely following the preceding works by Ogata et. al. (1993, 2003, 2004a for example).

Instead of imposing penalty on roughness (or unsmoothness) of $q(t)$ as in Eq. 3-8, we also consider the penalty on merely the amount of modifications;

$$\Phi(q|w) = w\sum_{k=1}^{N} {q_k}^2\,. \qquad (3\text{-}17)$$

With this penalty we hope to avoid unnecessary difficulty of enforced smoothness.

3-3. Applications to the earthquakes of selected regions

In this section we will apply the methods of misfit functions to detect anomalies in seismicity, to several cases where the change-point method is supposed to encounter difficulties. The first set of applications is on two regions where swarms were reported. The data sets used here came from the off shore of Boso peninsula and around Tokyo Bay. In 2000s the former region had two swarms both of which lasted around 10 days, and both are supposed to be caused by underlying slow slips (Ozawa et al. 2007, Okutani and Ide 2010). The latter contains one swarm event in the midst of 2000s

(Okutani and Ide 2010), and possible a few more since then. We can hence think those data compositions as earthquakes with the seismicity normal to the region, mixed with temporally spiked cluster of events under different mechanisms. The second set of applications is on the data sets from largely divided regions covering all major islands of Japan. Our interest here is to study what anomalies shall be observed, even though retrospectively, in those regions before the M9.0 Tohoku earthquake of 2011. The period of the data span over very long period dating back as early as 1923, hence a few to several changes in seismicity can be expected. The third set of applications treats selected data sets triggered by the M9.0 Tohoku earthquake.

3-4. Data with swarms

3-4-1. Boso peninsula

The Boso peninsula has been the site of recurring slow slip events on the subducting thrust interface, recently in 1996, 2002, 2007 [Ozawa et al. 2003, Sagiya 2004, Ozawa et al. 2007], and the last one was in 2010. These events, detected by GPS monitoring, last around 10 days each. Ozawa et al. [2007] suggested that those slow slips were the major triggering force of the accompanied earthquake swarms. Our data are taken from the polygonal region in Fig. 3-1, with the depth shallower than 90 km.

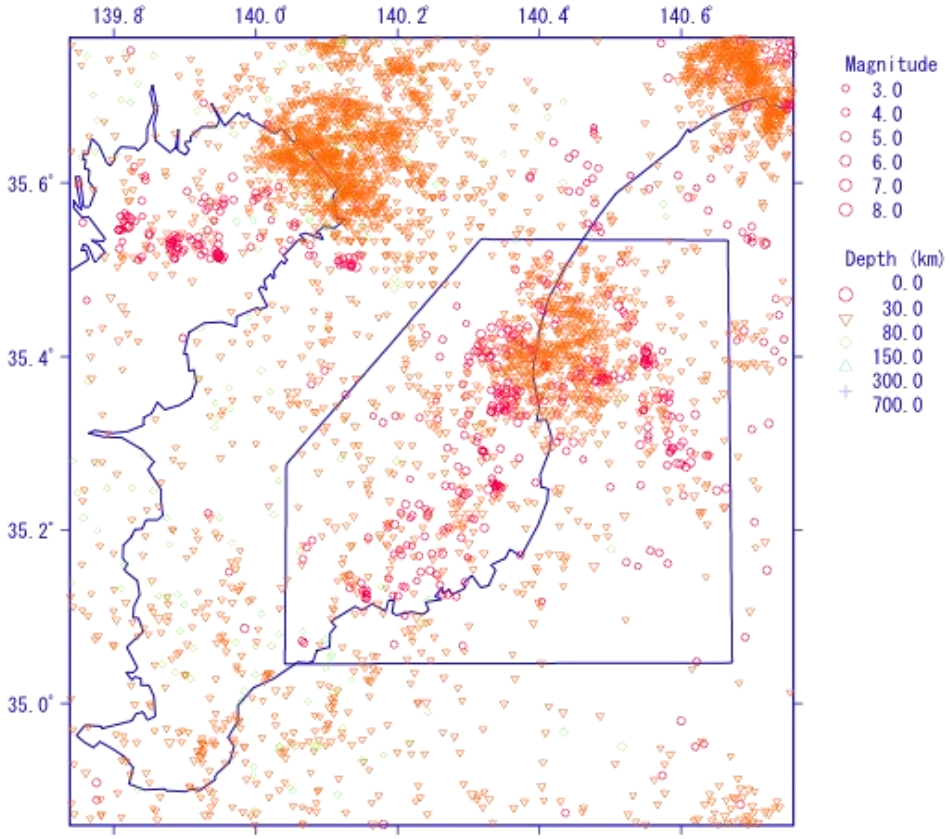

Figure 3-1. The polygonal regions of offshore of Boso peninsula, with hypocenters (colored marks) of M≥2, from Oct 1 1997 to Dec 31 2010.

3-4-1a, with the Data from 1980 to 2011

Our first data set is from the beginning of 1980 to the end of 2011, with the minimum magnitude of 2.5. The estimated misfit function for multiplicative modifier $q_{\lambda}(t)$ is shown as the black curves in the right panels of Fig. 3-2, with the reference parameters estimated from the beginning to the end of 2010 of the same data; (μ, K, c, α, p) = (0.012388, 0.031764, 0.0033545, 0.71559, 1.0668), which cumulative estimates are shows in red curves in the left panels of Fig. 3-2. The dashed lines above and below the $q_{\lambda}(t)$ represent one σ error bars. The peaks in the $q_{\lambda}(t)$ correspond to swarm events, indicating that the reference model fails to capture those swarms. We suspect that, because of slow slips, the mechanisms underlying the earthquakes are different from what thought to be normal in this region. Putting this in another way, it is possible to detect slow slip events from misfits of the ETAS model. Left lateral tails of the misfit

function in the $q_{\lambda}(t)$ on the normal time are merely the byproduct of asymmetricity in the time transformation. The smoothing by itself tends to generate symmetric shape of broken line, as can clearly be seen in the right lower panel.

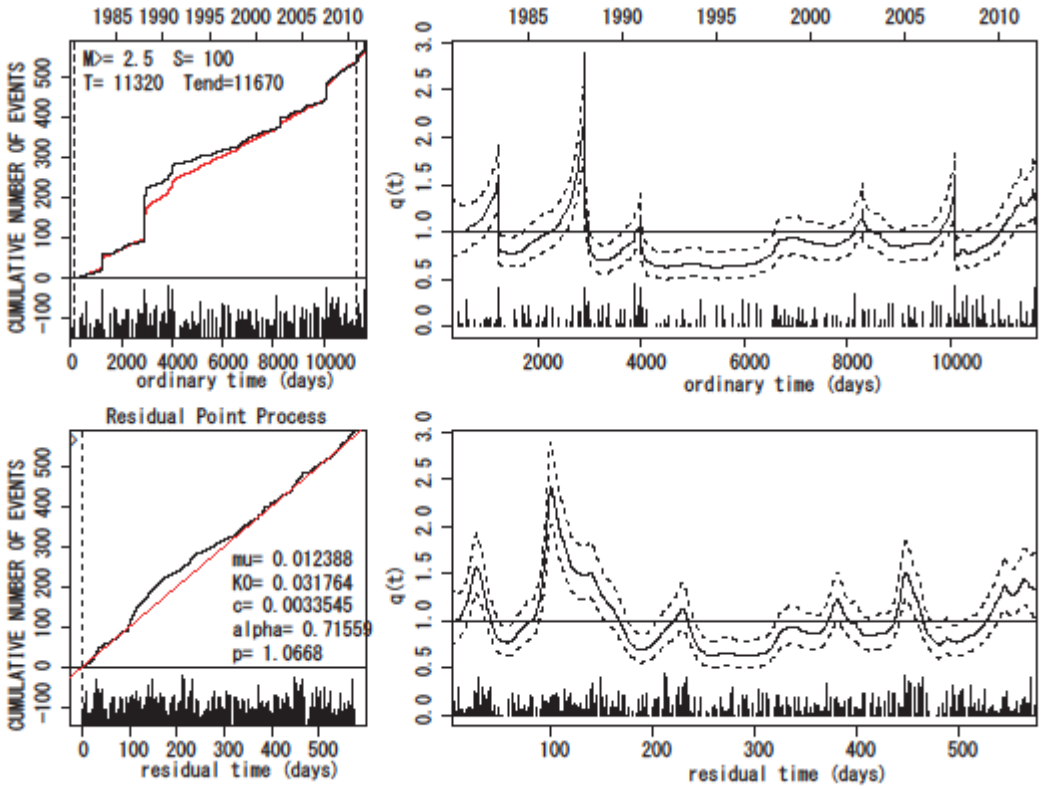

Figure 3-2.

(left): reference ETAS estimate (red curve) and observed cumulative count (black curve) under ordinary time. The reference parameters are (μ, K, c, α, p) = (0.012388, 0.031764, 0.0033545, 0.71559, 1.0668), estimated in-between two broken line of [S,T]=[100, 11320] , corresponding to the period from 19890 to 2010. The vertical half lines in the lower part represent events with heights as their magnitudes.

(right): misfit function $q_{\lambda}(t)$ under respectively ordinary (upper) and transformed (lower) time. The dashed lines show one σ error bars.

The thick blue line in Fig. 3-3 shows the estimated $\mu(t)$ of time-variant background, with the same reference parameters used above. The gray band around the $\mu(t)$ shows one σ error bar, although it is tight here and hardly be seen. The red curve represents $\lambda(t)$. The $\mu(t)$ being flat and equal to the reference back ground all over the period means no misfit is detected. This is probably because the periods of slow slips are too short (around 10 days each compared with the whole period of over 20 years). The lower

panel of Fig. 3-3 shows the same $\mu(t)$ with each event evenly spaced by the index order. This rearrangement is the substitute for the residual time transformation. Like the $q_\lambda(\tau)$ on the residual time, this rearrangement helps us to see closely the shape of misfit function where the events are densely clumped.

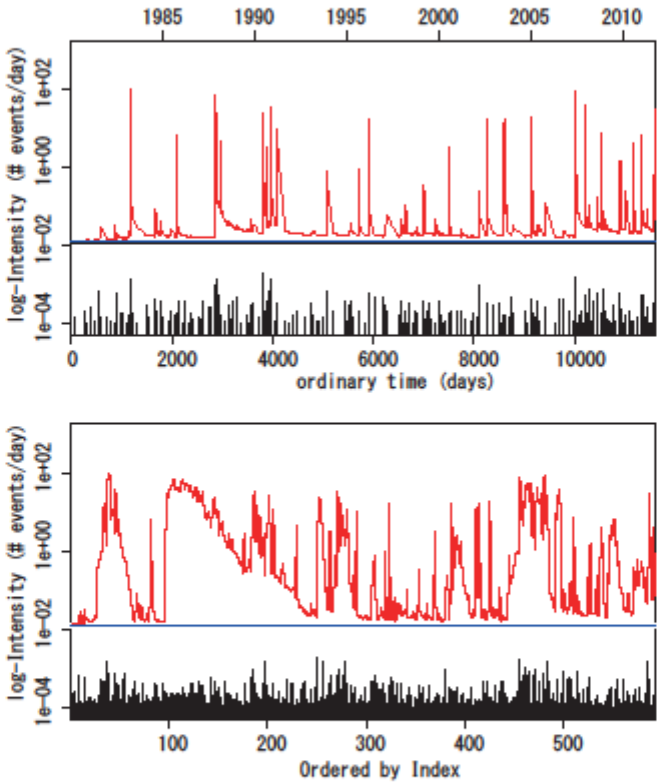

Figure 3-3. (Upper, on the ordinary time) Estimated time variant background seismicity ($\mu(t)$) in blue curve, and the intensity $\lambda(t)$ (events/days) in red curve. The gray band around the $\mu(t)$ represents one σ error bar. (Lower) same, rearranged by index order.

3-4-1b, from 1997 to 2011

Here we limit our attention on more resent period, from the Oct. of 1997 to the end of 2011, with the minimum magnitude of 2.0 which is slightly lower than the previous case. The estimated misfit function for multiplicative modifier $q_\lambda(t)$ is shown as the black curves in the right panels of Fig. 3-4, with the reference parameters estimated before 2011; (μ, K, c, α, p) = (0.027607, 0.027696, 0.0025633, 0.74832, 1.0216). The earlier two peaks in the $q_\lambda(t)$ in Fig. 3-4 correspond to the reported swarms of 2002 and 2007, and the last peak corresponds to the swarm event in the Oct. of 2010. For the $\mu(t)$, we

now see a gradual increase in the last few years. This increase in the background is probably due to the Tohoku earthquake of M9.0 in 11 Mar 2011. This increase that we have now while we did not in the previous application is simply because the period is longer in the previous case and that the ABIC accordingly favored flatter landscape of $\mu(t)$.

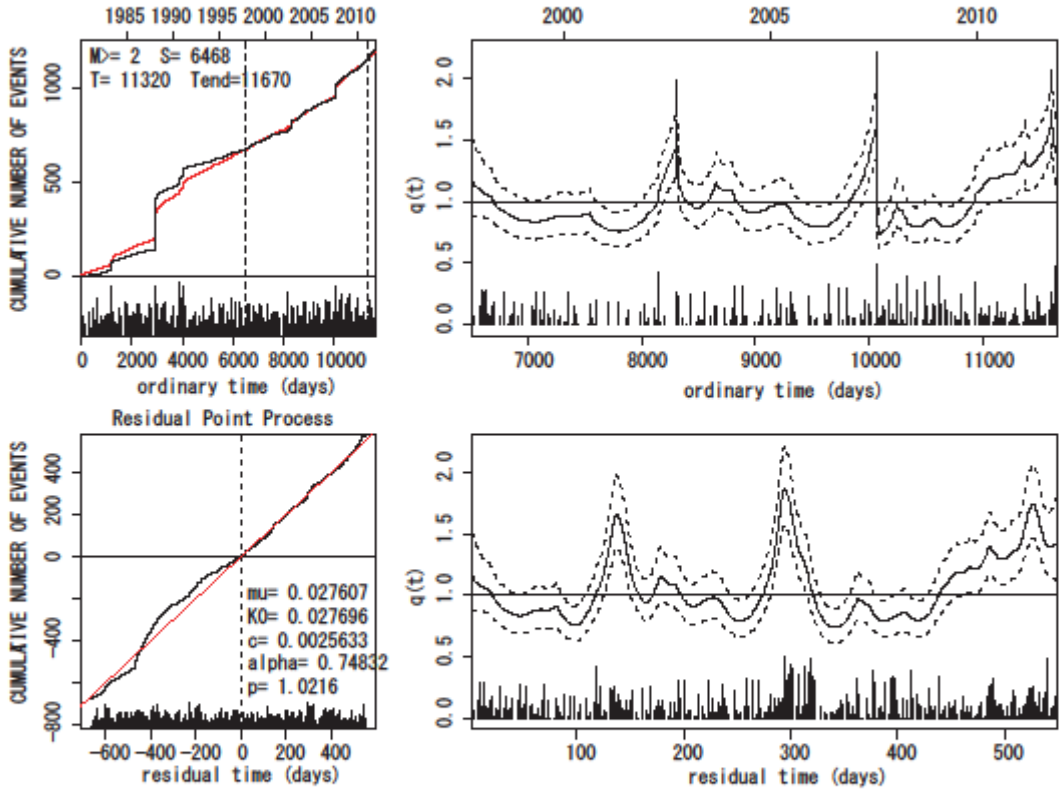

Figure 3-4.

(left): reference ETAS estimate from [S,T]=[6468, 11320], corresponding to the period from Oct. of 1997 to the end of 2010.

(right): misfit function $q_{\lambda}(t)$ under respectively ordinary (upper) and transformed (lower) time. The dashed lines show one σ error bars.

For the $\mu(t)$, we now see a gradual increase in the last few years. This increase in the background is probably due to the Tohoku earthquake of M9.0 in 11 Mar 2011. This increase that we have now while we did not in the previous application is simply because the period is longer in the previous case and that the ABIC accordingly favored flatter landscape of $\mu(t)$. This example and some simulations in the later chapter suggests that we needs certain fraction of period of anomalies to see it as a non-flat

landscape of $\mu(t)$. When we can further narrow down the period of our interest, we can close up more the landscape of $\mu(t)$. Fig. 3-6, for example, details the anomalies in only 2011. The first hump corresponds to the Tohoku earthquake, and the last one to the swarm events in October.

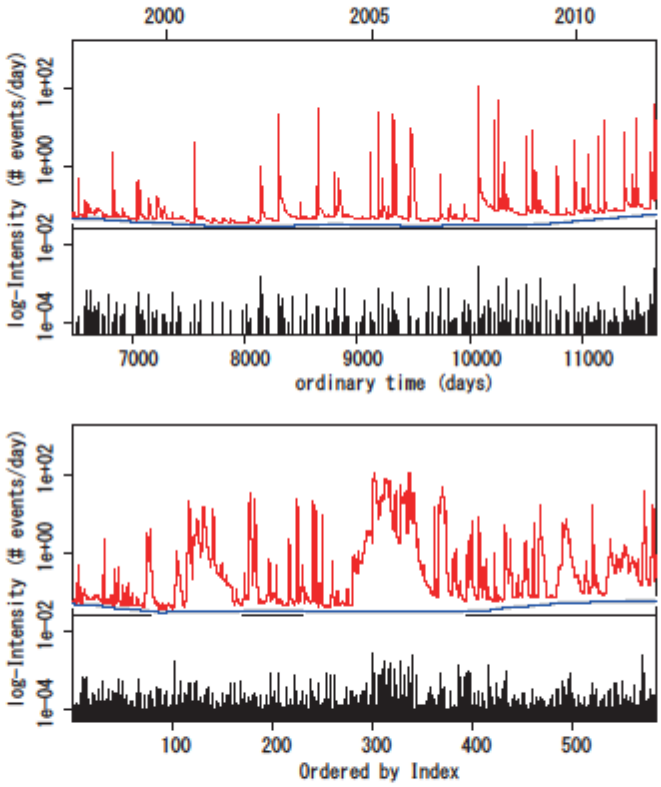

Figure 3-5. Estimated time variant background seismicity $\mu(t)$ in blue curve with gray band of one σ error bar, and the intensity $\lambda(t)$ in red curve, on the normal time (upper) and in the index order (lower).

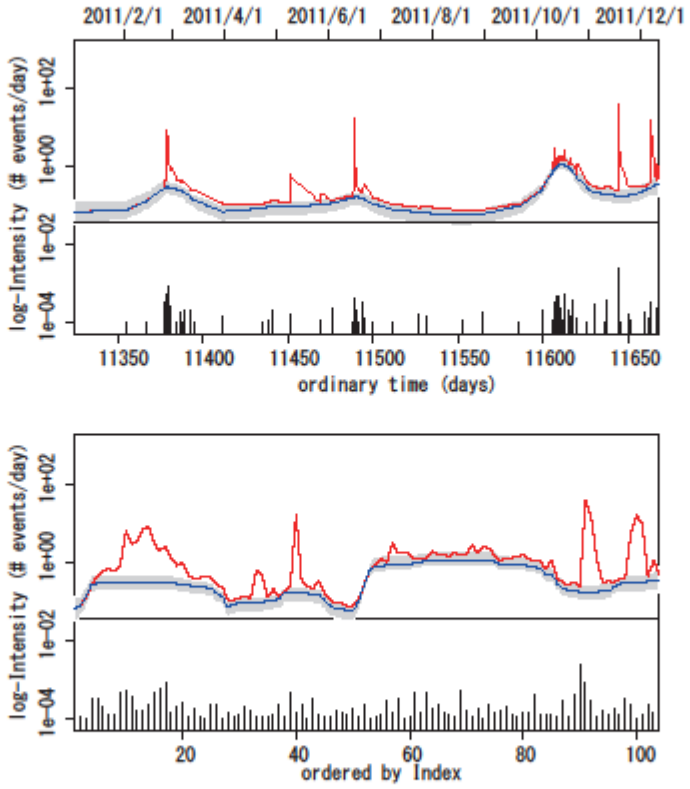

Figure 3-6. $\mu(t)$ estimated from 2011, with the same reference parameters as before.

3-4-2. Tokyo Bay

3-4-2a, with the Data from 1980 to 2011

The earthquake data is taken from the rectangle region in Fig. 3-7, from 1980 to 2011 with magnitude larger than 1.8. The reference ETAS parameters are estimated from the period of (S,T)=(100,11320), which is from 1980 to the end of 2010, to avoid the triggering effect by the Tohoku earthquake in 2011. The misfit function $q_{\lambda}(t)$ in Fig. 3-8 shows that the seismicity had increased since 2005 then has been decreasing after the Tohoku earthquake. In Fig. 3-9, $\mu(t)$ shows gradual increase from 2005, although it fails to capture details, as in the previous case of Boso peninsula.

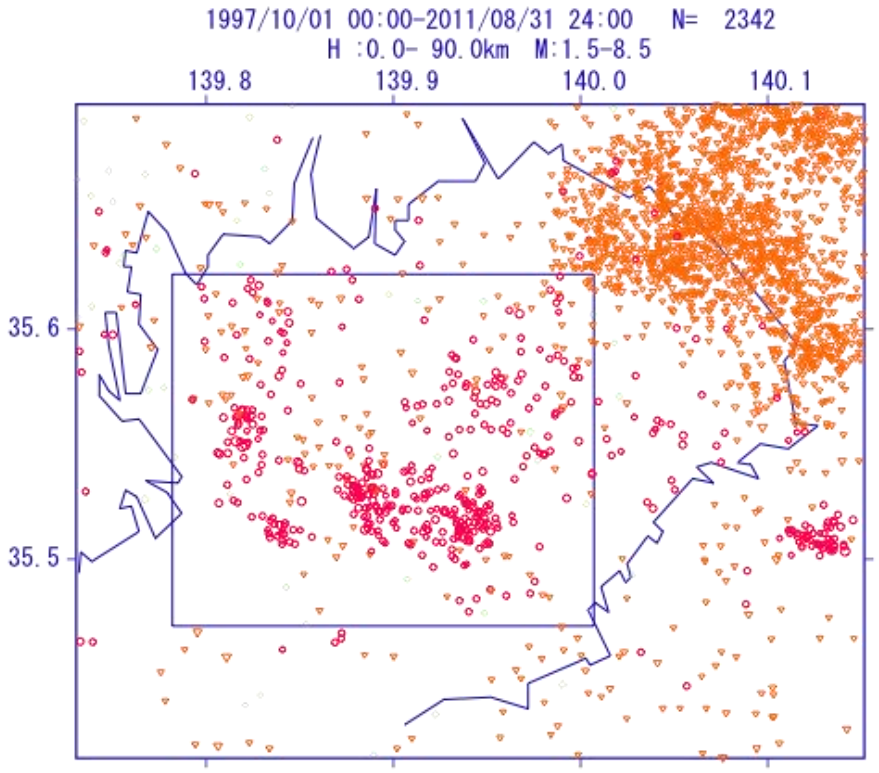
1997/10/01 00:00-2011/08/31 24:00 N= 2342
H :0.0- 90.0km M:1.5-8.5
139.8
139.9
140.0
140.1
35.6
35.5

Figure 3-7. The data are from the rectangle region in Tokyo Bay. The colored marks represent hypocenters of M≥1.8, from 1997 to 2011.

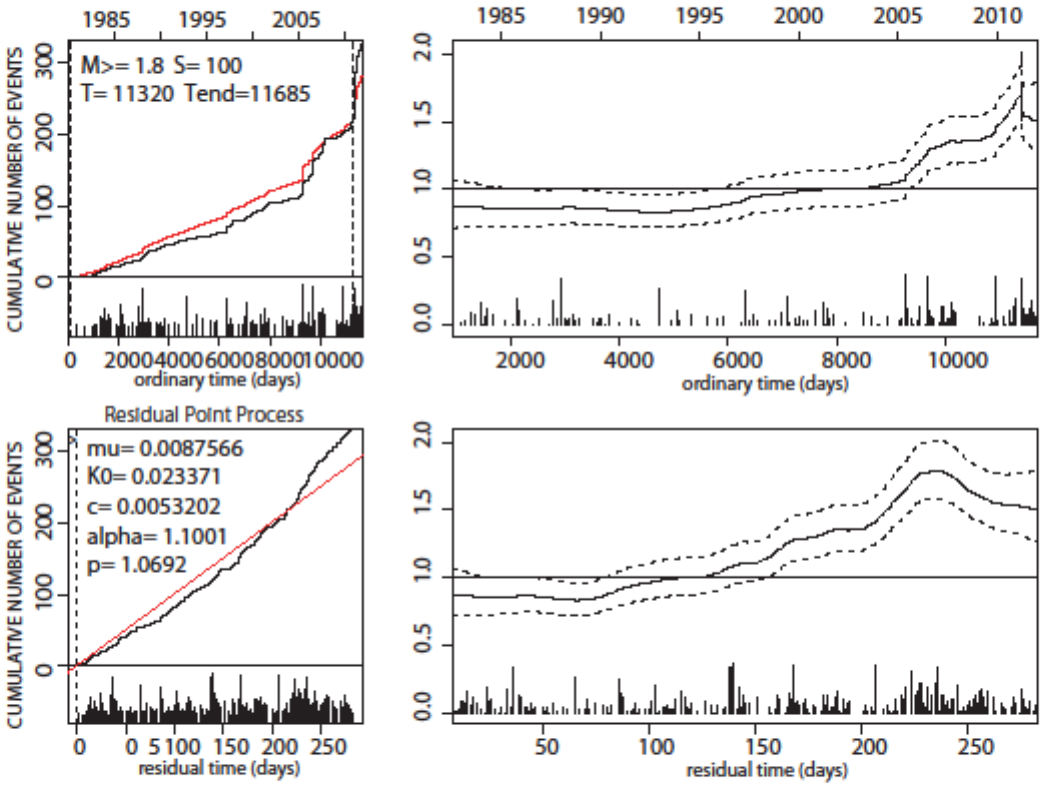

Figure 3-8.

(left): reference ETAS estimate from [S,T]=[100, 11320], corresponding to year 1980 to 2010.

(right): misfit function $q_{\lambda}(t)$ under respectively ordinary (upper) and transformed (lower) time. The dashed lines show one σ error bars.

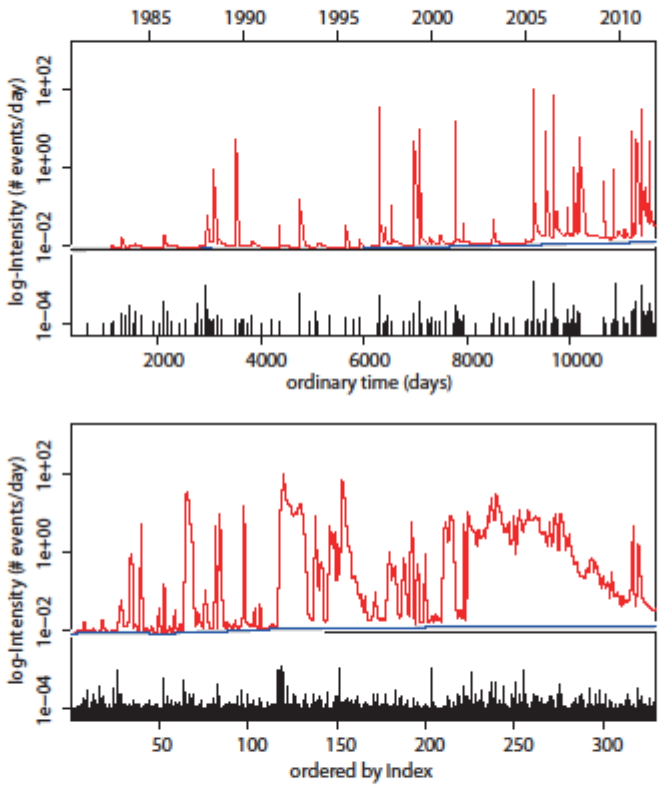

Figure 3-9. Estimated time variant background seismicity $\mu(t)$ in blue curve with gray band of one σ error bar, and the intensity $\lambda(t)$ in red curve, on the normal time (upper) and in the index order (lower).

3-4-2b, with the Data from Oct 1997 to 2011

Within the same region, we now focus on more recent events, from Oct 1997 to 2011, with slightly smaller minimum magnitude of 1.5. The reference parameters are taken from the beginning of the data to the end of 2010, again to avoid the triggering effect by the Tohoku earthquake. In Fig. 3-10 the seismicity has been increased after 2005, and in Fig. 3-11, $\mu(t)$ shows clearer increased from around 2009. The difference of this later and steeper increase and the $\mu(t)$ in Fig. 3-9 in the previous example is that shorter period with smaller minimum magnitude resulted in more detailed landscape of $\mu(t)$.

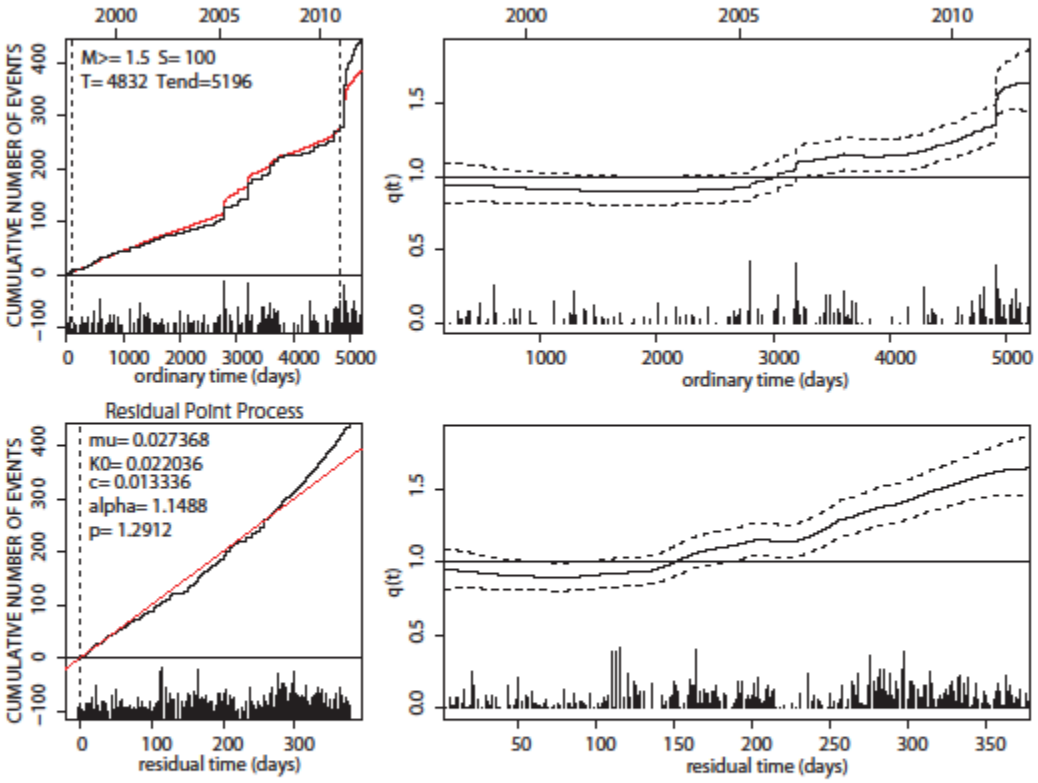

Figure 3-10.

(left): reference ETAS estimate from [S,T]=[100, 11320], corresponding to year 1980 to 2010.

(right): misfit function $q_{\lambda}(t)$ under respectively ordinary (upper) and transformed (lower) time. The dashed lines show one σ error bars.

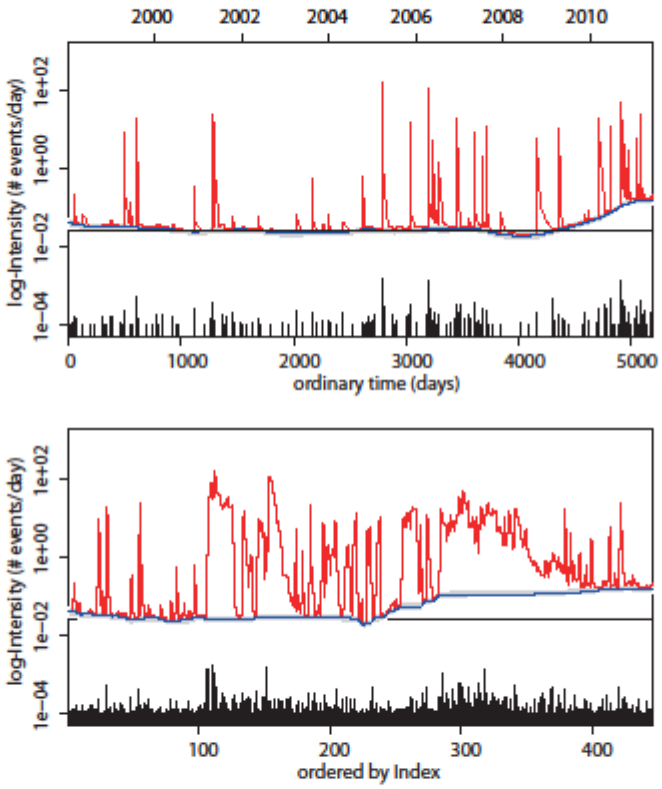

Figure 3-11. Estimated time variant background seismicity $\mu(t)$ in blue curve with gray band of one σ error bar, and the intensity $\lambda(t)$ in red curve, on the normal time (upper) and in the index order (lower).

Now we take the reference parameters from the period before 2005 ([S,T]=, considering that the seismicity in this region was normal in that period. In the left panels of Fig. 3-12, the cumulative count of the event (black curve) indeed shows no anomalies occurred during the period. The misfit function $q_{\lambda}(t)$ in the right panels of Fig. 3-12 now has three peaks from 2005 to 2007, as well as a small peak before the Tohoku earthquake followed closely by a large one reflecting the triggering by the Tohoku earthquake. Apart from the last large peak, each of the other four peaks corresponds to swarm events. The $\mu(t)$ in Fig. 3-13 also shows corresponding increase, although more roughly, during the earlier three swarm period, in addition to the increase from around 2009 which we have seen in Fig. 3-11. Thus by taking parameters which thought to be "normal" to the focal region, we are potentially able to detail anomalies further.

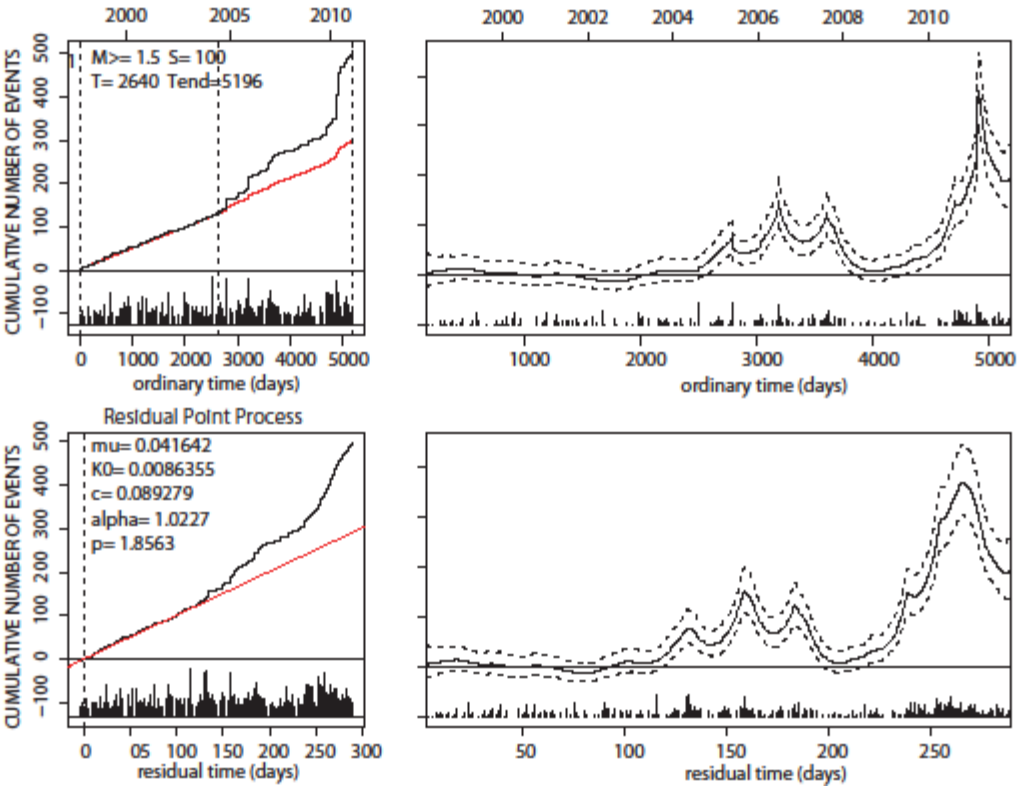

Figure 3-12.

(left): reference ETAS estimate from [S,T]=[100, 4832], corresponding to the period from Oct 1997 to 2004.

(right): misfit function $q_{\lambda}(t)$ under respectively ordinary (upper) and transformed (lower) time. The dashed lines show one σ error bars.

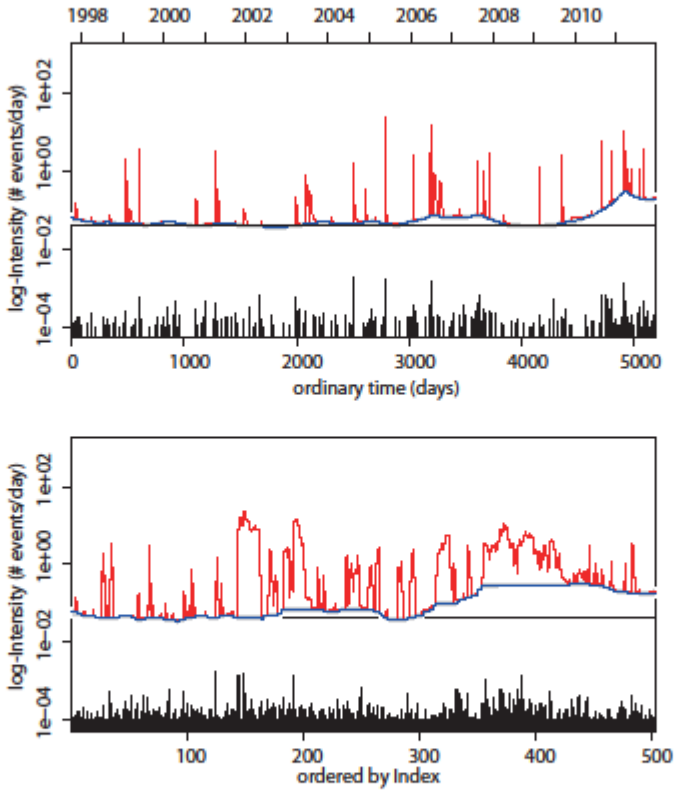

Figure 3-13. Estimated time variant background seismicity $\mu(t)$ in blue curve with gray band of one σ error bar, and the intensity $\lambda(t)$ in red curve, on the normal time (upper) and in the index order (lower).

3-5. Seismic anomalies before M9.0 Tohoku earthquake

In these applications we examine what anomalies can be revealed before the earthquake of so large a magnitude of M9.0, during long period of time over wide region. The data are taken from the rectangular regions of Fig. 3-14, from 1923 to the end of 2010, with minimum magnitude of M=5.0 and shallower than 200 km deep. The data are then combined with the Utsu catalog of the same region, from 1885 to 1925. The Utsu catalog part of the data is then used as the preliminary period to estimate the reference parameters. Ogata [2011] reported that, by declustering with space-time ETAS model, there was significantly observable quiescence all over Japan region. This section is to confirm this wide-ranging quiescence with our methods.

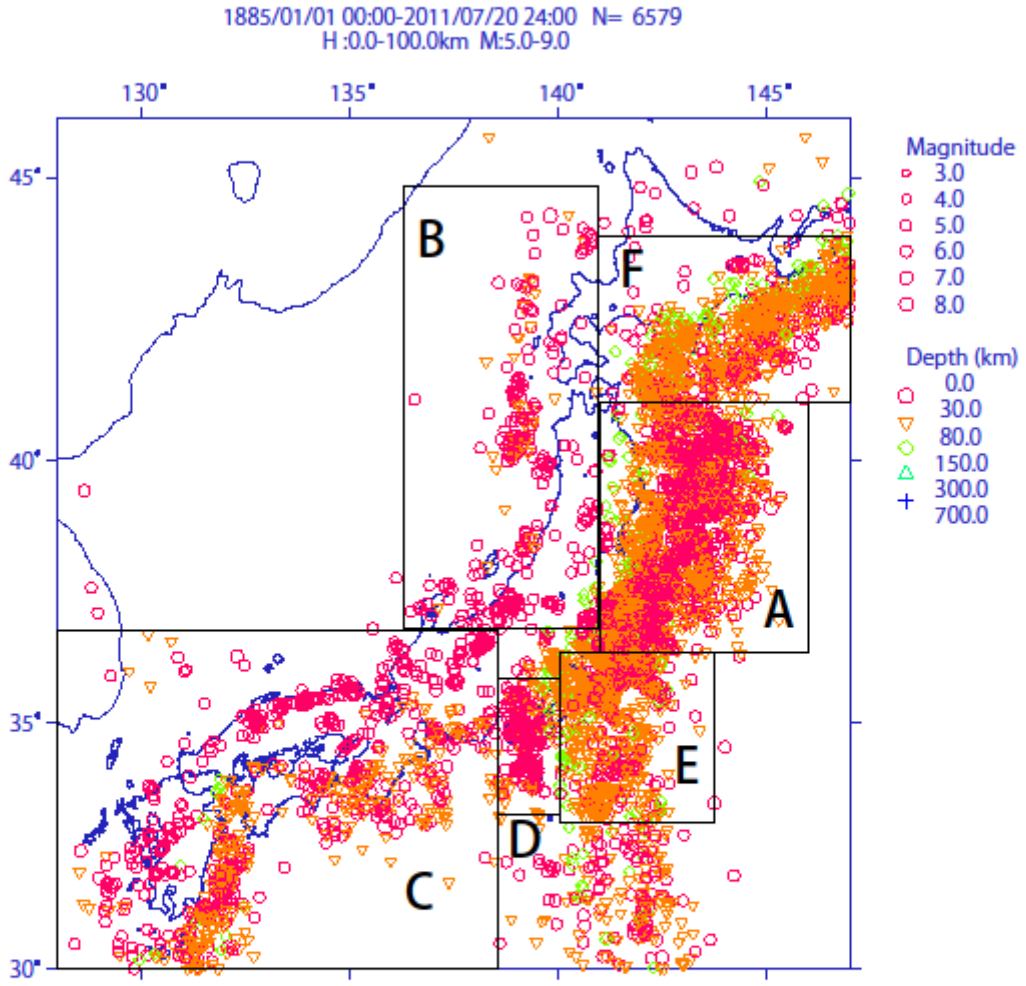

Figure 3-14. Zoning of the Japan main islands, into seven rectangular regions of A ~ F

3-5-1. Region A: Tohoku offshore

The region A covers Pacific offshore of the Tohoku district. According to the misfit function $q_{\lambda}(t)$ in Fig. 3-15, there are several misfits of the reference model. Most of the positively spiked misfits seem to correspond to large earthquakes, with an interesting exception that occurs around 1933. The swarm-like events in 1933 are ascribed to the 1933 Sanriku earthquake of M=8.1, arose in the outer rise area to the east of our focal region. This misfit disappears if we add its main shock into the data. One should note a large and a decade-long drop in $q_{\lambda}(t)$ at the end, from mid 1990s. It indicates there had been long quiescent period before the Tohoku earthquake. The time-variant background $\mu(t)$ in Fig. 3-16 also shows decrease during the corresponding period.

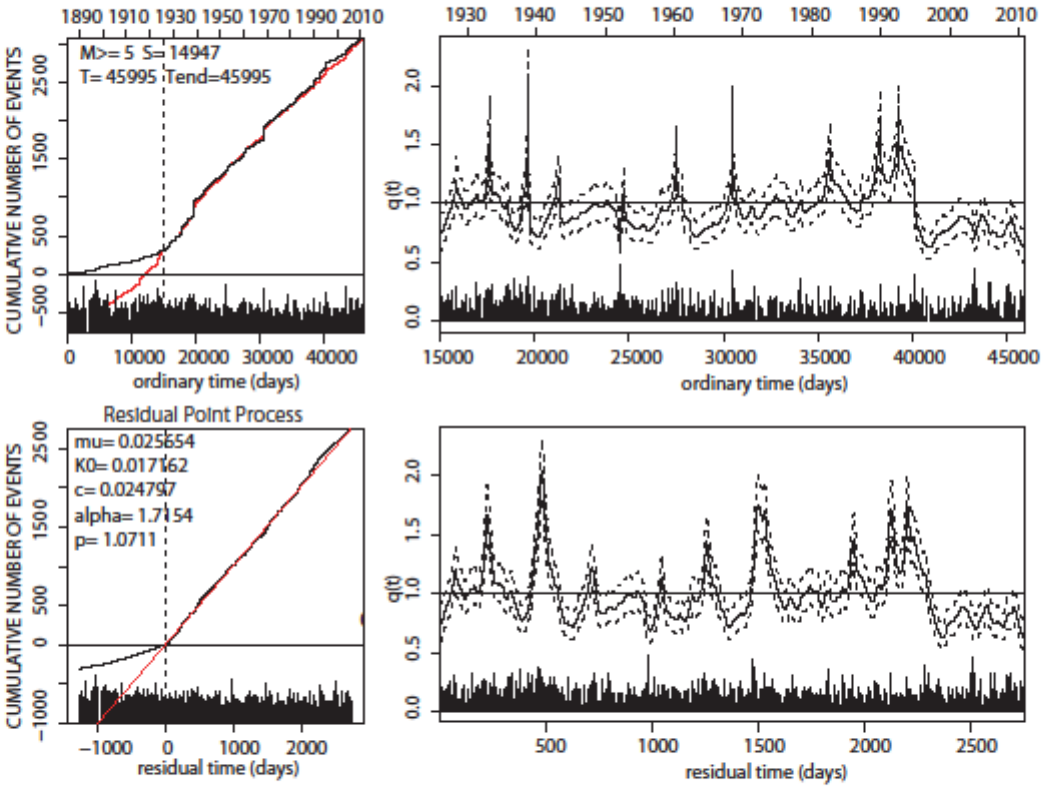

Figure 3-15.

(left): reference ETAS estimate from [S,T]=[14947, 45995], corresponding to the period from the beginning of 1926 to the end of 2010.

(right): misfit function $q_{\lambda}(t)$ under respectively ordinary (upper) and transformed (lower) time. The dashed lines show one σ error bars.

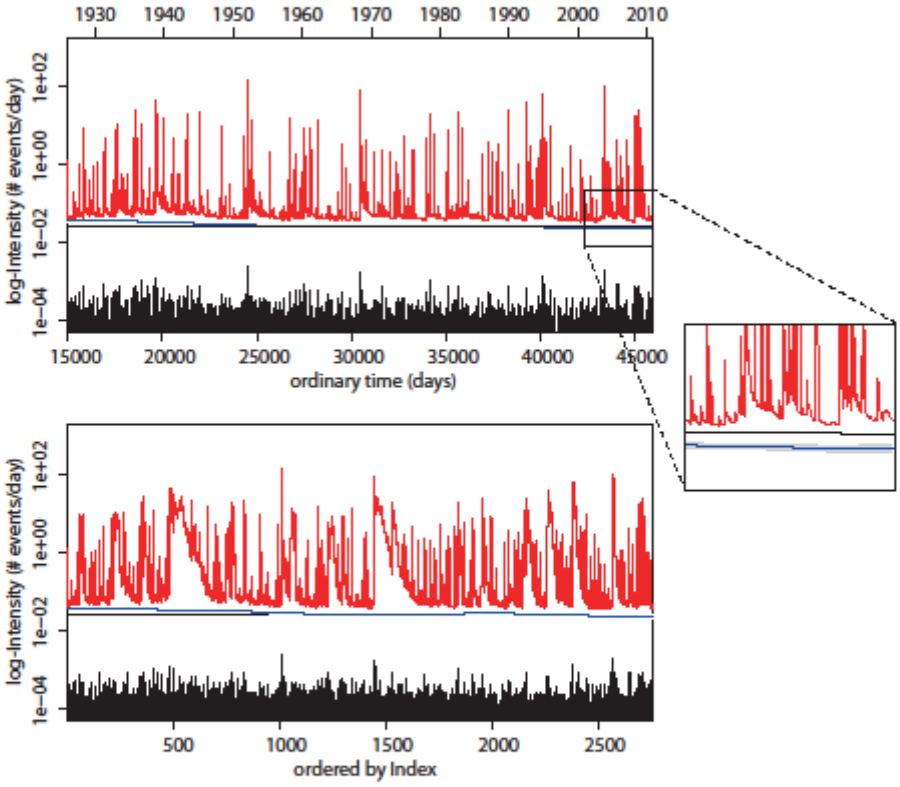

Figure 3-16. Estimated time variant background seismicity $\mu(t)$ in blue curve with gray band of one σ error bar, and the intensity $\lambda(t)$ in red curve, on the normal time (upper) and in the index order (lower). A small square in the upper panel is magnified in the right.

3-5-2. Region B: Inland Tohoku and Japan sea area

The region B covers some part of inland Tohoku district and northern Japan Sea. The misfit functions $q_{\lambda}(t)$ in Fig. 3-17 shows ostensible peak in the earlier half of 1980s, the peak of which corresponds to the 1983 central Japan Sea earthquake of M=7.7, and one can observe a drop in $q_{\lambda}(t)$ (i.e. quiescence) for more than 10 years before it. The next small peak corresponds to the 2004 Chuetsu earthquake, and one can also observe a preceding quiescence. The $\mu(t)$ in Fig. 3-18 however remains flat, either because changes, if any, are too delicate for this method with this long period, or because the changes in the background seismicity are actually small.

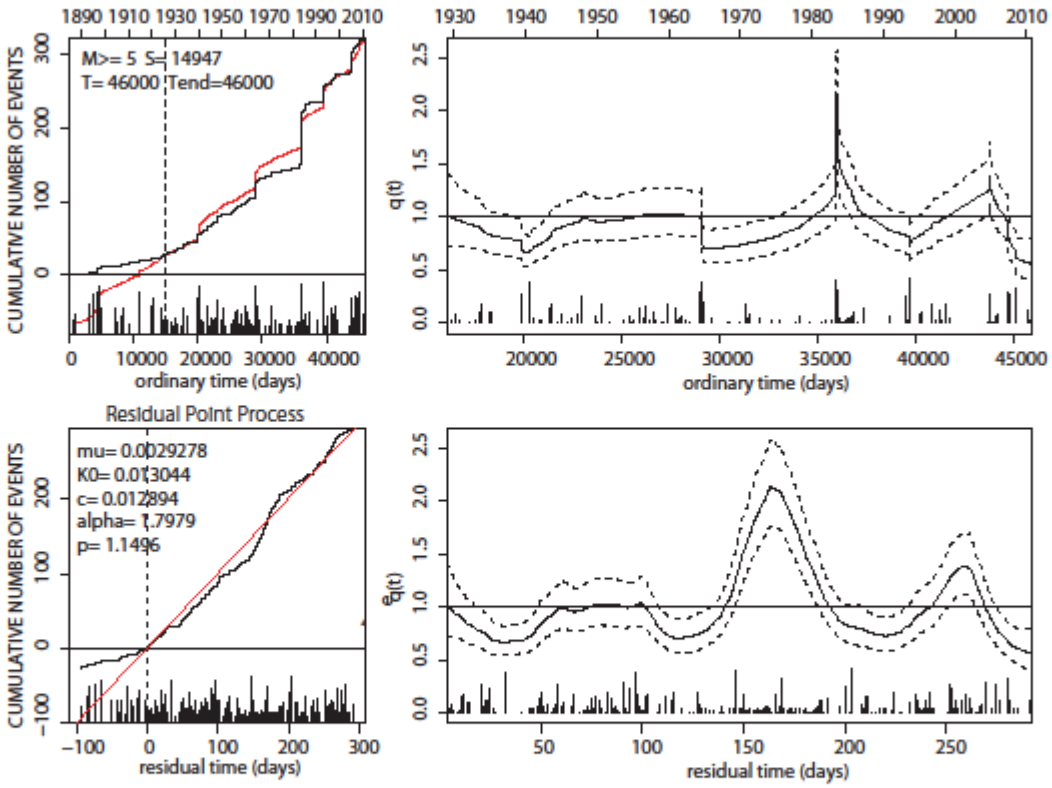

Figure 3-17.

(left): reference ETAS estimate from [S,T]=[14947, 46000], corresponding to the period from the beginning of 1926 to the end of 2010.

(right): misfit function $q_{\lambda}(t)$ under respectively ordinary (upper) and transformed (lower) time. The dashed lines show one σ error bars.

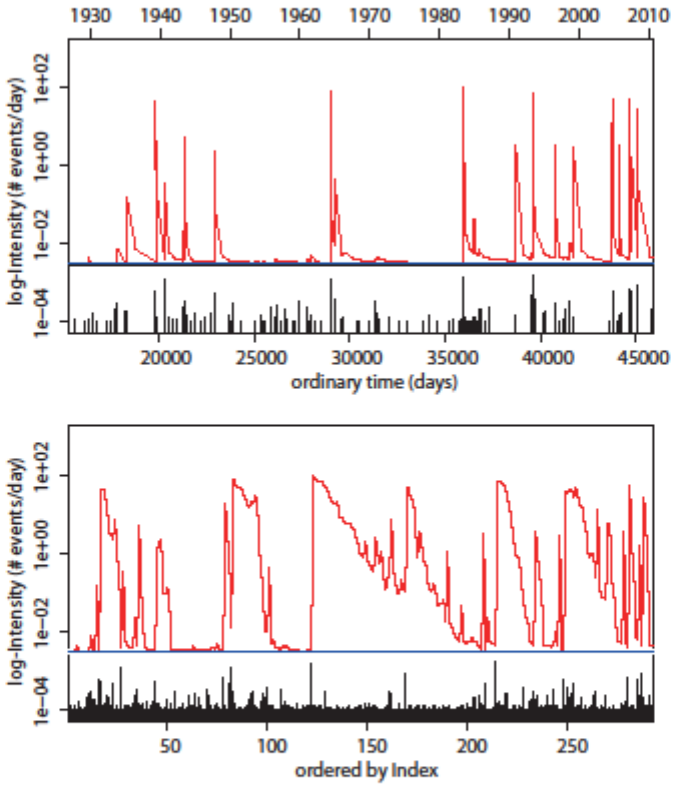

Figure 3-18. Estimated time variant background seismicity $\mu(t)$ in blue curve with gray band of one σ error bar, and the intensity $\lambda(t)$ in red curve, on the normal time (upper) and in the index order (lower).

3-5-3. Region C: West Japan

The region C covers all over the west part of Japan. Fig. 3-19 in the right panel shows the misfit functions $q_{\lambda}(t)$. It has two peaks in the 1940s, corresponding to Nankai and Tonankai earthquakes of 1944 and 1946 respectively. It has a decade's drop in the 1970s, then another and larger drop from 1995, right after the Southern Hyogo prefecture earthquake. This large quiescence is also be seen in Fig. 3-20.

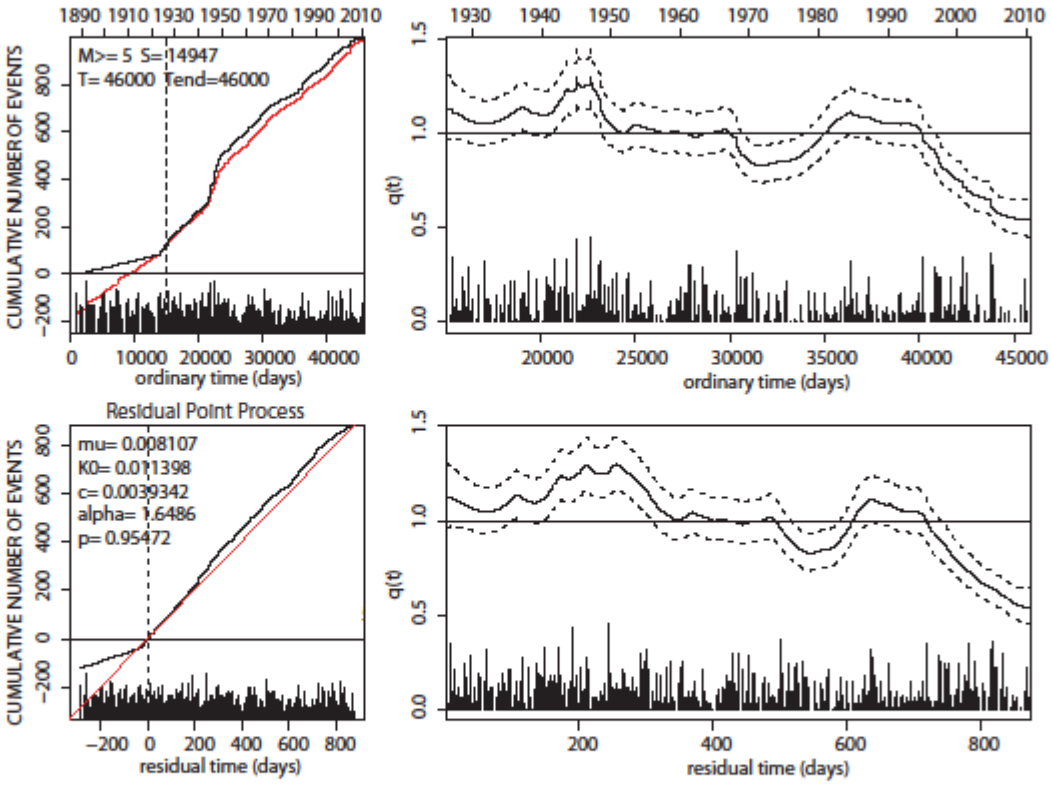

Figure 3-19.

(left): reference ETAS estimate from [S,T]=[14947, 46000], corresponding to the period from the beginning of 1926 to the end of 2010.

(right): misfit function $q_{\lambda}(t)$ under respectively ordinary (upper) and transformed (lower) time. The dashed lines show one σ error bars.

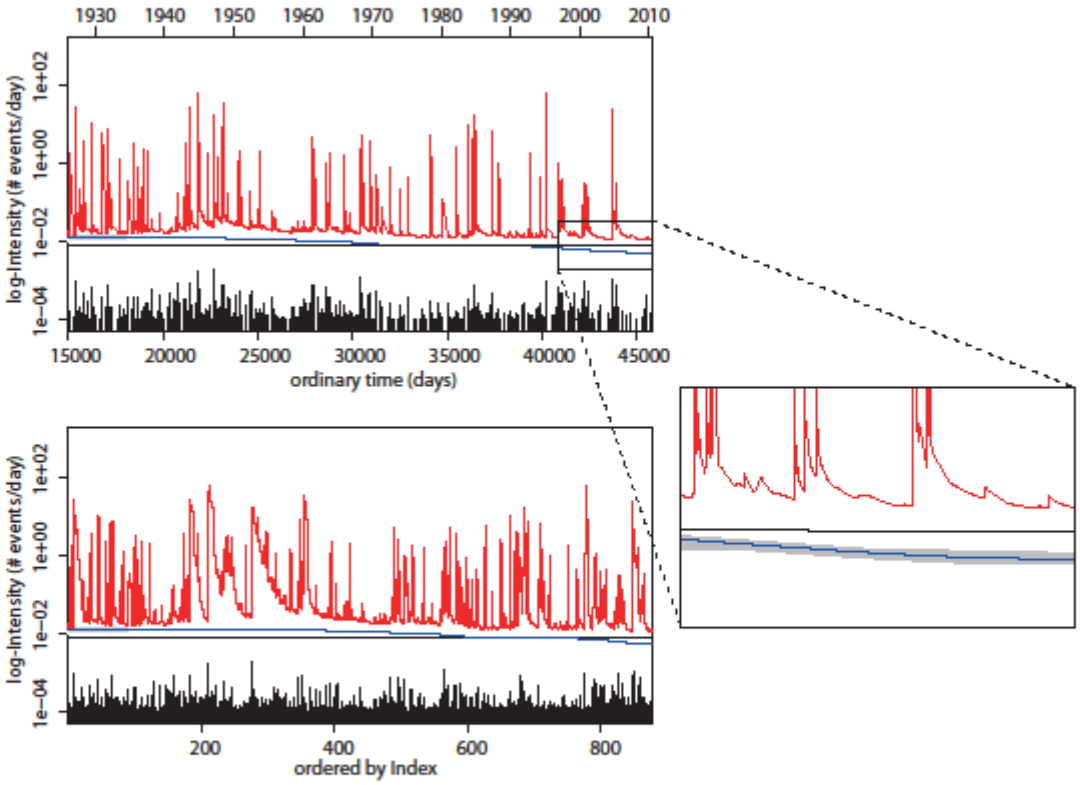

Figure 3-20. Estimated time variant background seismicity $\mu(t)$ in blue curve with gray band of one σ error bar, and the intensity $\lambda(t)$ in red curve, on the normal time (upper) and in the index order (lower). A small square in the upper panel is magnified in the right.

3-5-5. Region D: Izu

Region D covers Izu peninsula and northern Izu archipelago including Miyake islands. The misfit function $q_{\lambda}(t)$ in the right panel of Fig. 3-21 has large peak in 2000, which corresponds to the swarms due to volcanic eruption of Miyake island in 2000. Quiescence after that is also noticeable. The $\mu(t)$ in Fig. 3-22 shows, although much less clearly, a quiescence after 2000. As the reference we used the period before the 2000 swarm, for including it makes the reference α unnaturally small of the order of around minus seventeenth.

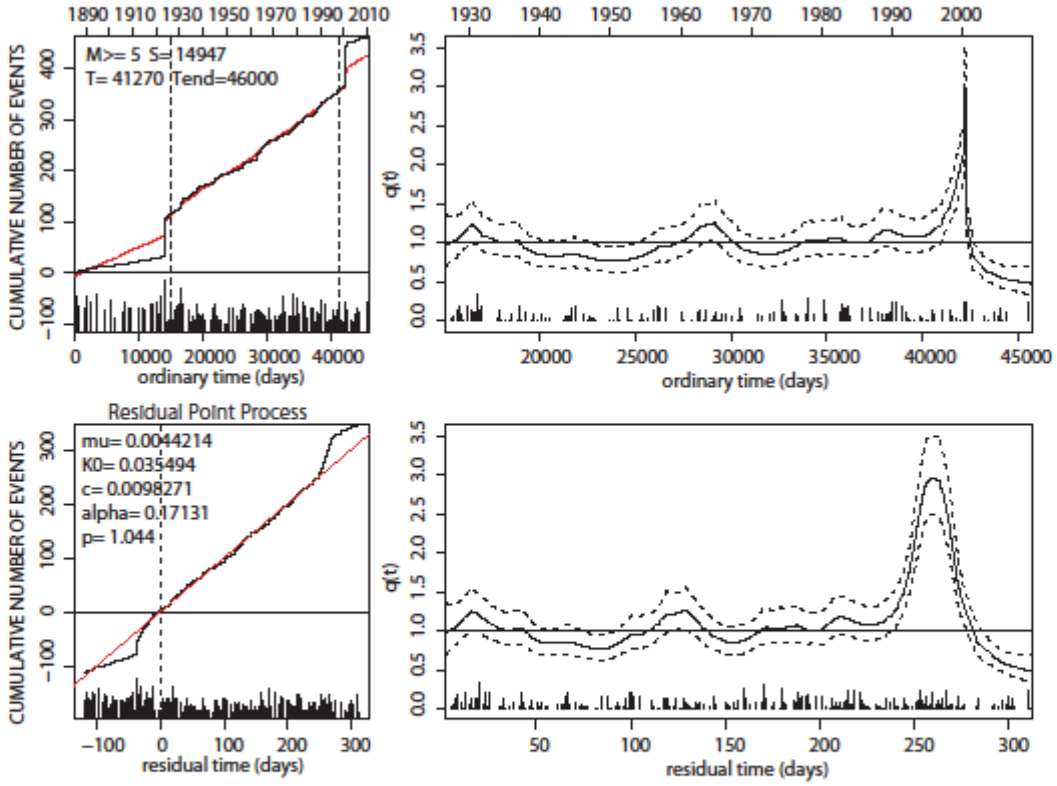

Figure 3-21.

(left): reference ETAS estimate from [S,T]=[14947, 41270], corresponding to the period from the beginning of 1926 to the end of 1997.

(right): misfit function $q_{\lambda}(t)$ under respectively ordinary (upper) and transformed (lower) time. The dashed lines show one σ error bars.

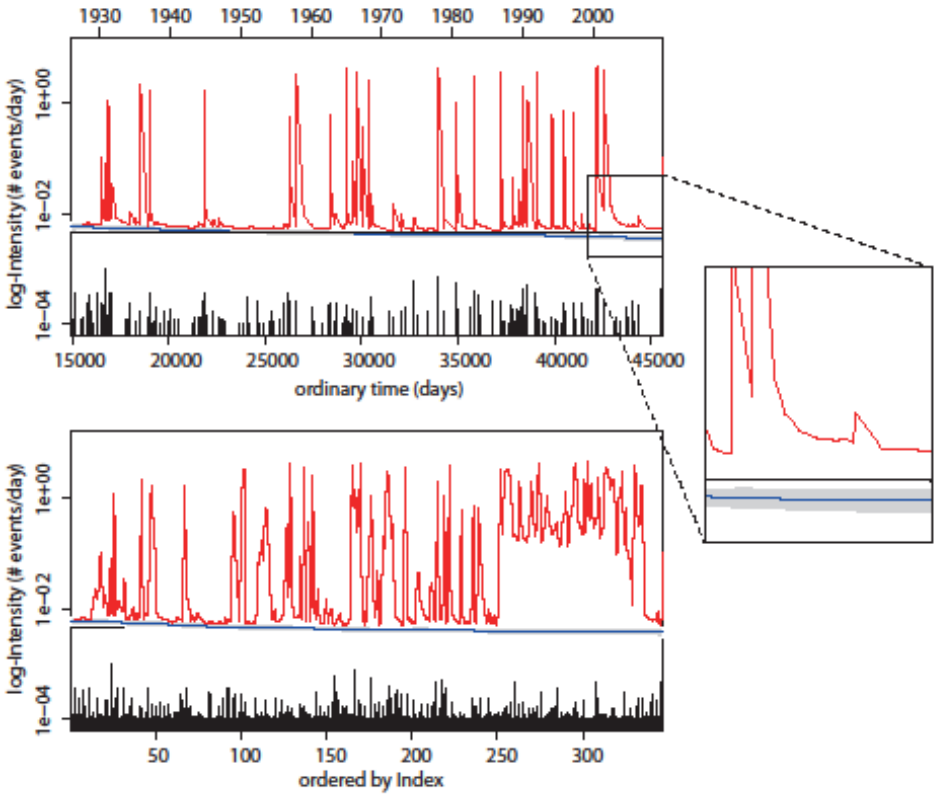

Figure 3-22. Estimated time variant background seismicity $\mu(t)$ in blue curve with gray band of one σ error bar, and the intensity $\lambda(t)$ in red curve, on the normal time (upper) and in the index order (lower). A small square in the upper panel is magnified in the right.

3-5-6. Region E: Kanto

The region E covers Kanto area, including Tokyo Bay and Boso offshore. Fig. 3-23 shows short period of quiescence in-between broken and solid lines at the very end. In Fig. 3-24, the misfit function $q_{\lambda}(t)$ shows slight decrease during the corresponding period. The earlier hump of misfit is due to the aftershocks of 1923 Kanto earthquake. The $\mu(t)$ also detect slight decrease at the end of the period (Fig. 3-25).

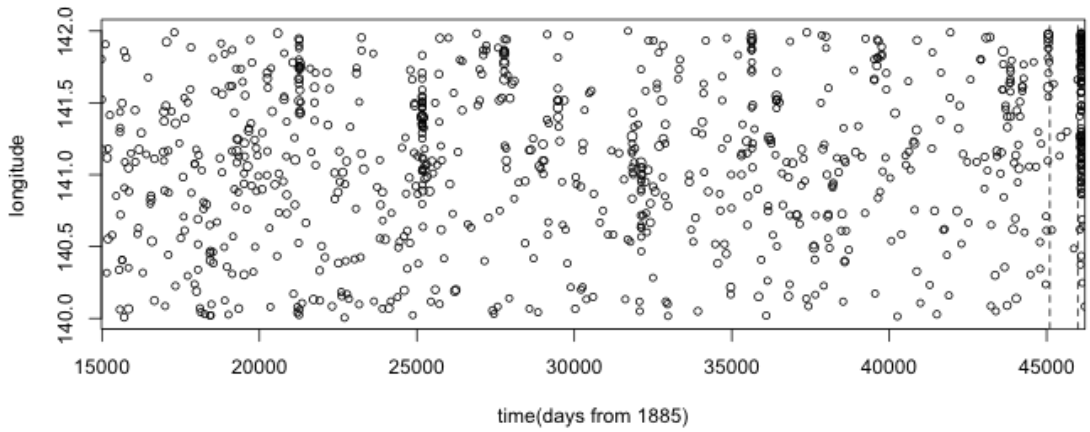

Figure 3-23. West-East distribution (Y-axis) of events in region F over time (X-axis, in days from 1885). The solid line corresponds to the M9.0 Tohoku Earthquake, and the broken line illustrates the beginning of the quiescence, roughly decided by the eye.

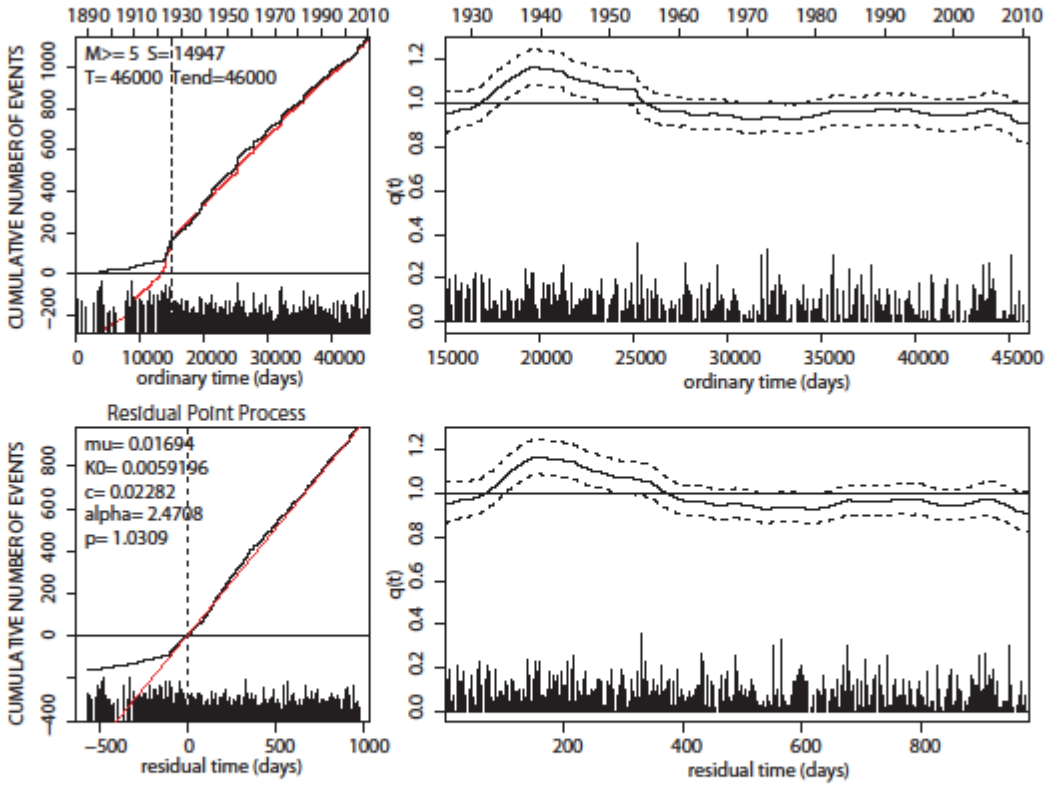

Figure 3-24.

(left): reference ETAS estimate from [S,T]=[14947, 46000], corresponding to the period from the beginning of 1926 to the end of 2010.

(right): misfit function $q_\lambda(t)$ under respectively ordinary (upper) and transformed (lower) time. The dashed lines show one σ error bars.

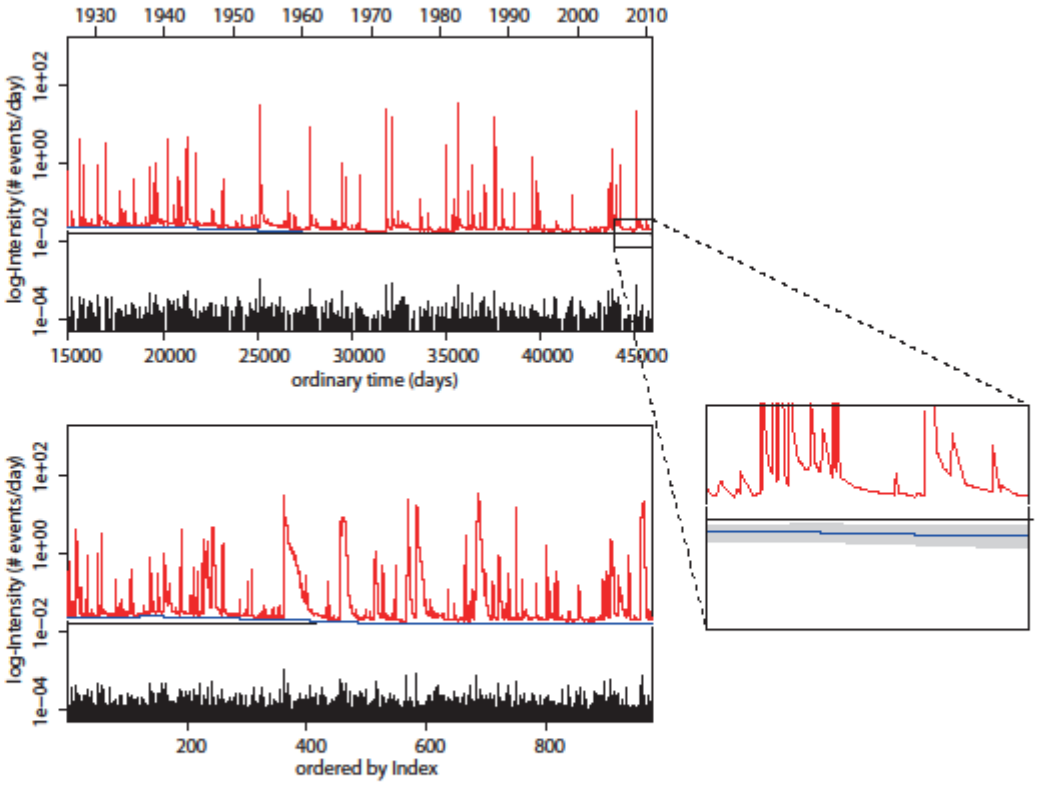

Figure 3-25. Estimated time variant background seismicity $\mu(t)$ in blue curve with gray band of one σ error bar, and the intensity $\lambda(t)$ in red curve, on the normal time (upper) and in the index order (lower). A small square in the upper panel is magnified in the right.

3-5-7. Region F: Hokkaido

The region F covers offshore of northern Tohoku district and southern Hokkaido. In Fig. 3-26, each peak of the misfit function $q_\lambda(t)$ corresponds, from the earliest since 1960, to 1968 Tokachi-Oki earthquake of M7.9, 1973 Nemuro-Oki earthquake of M7.4, 1994 Sanriku far offshore earthquake of M7.4, and 2003 Tokachi-Oki earthquake of M8.0, respectively. The largest peak in 1994 is due mainly to the data missing the main shock while cover some of its aftershocks. One can observe quiescence before each of those large events, and during several years at the end of the period. The $\mu(t)$ in Fig. 3-27 too shows weak decrease at the end, but none of the other misfits in *q(t)* probably because they are too detailed for the method.

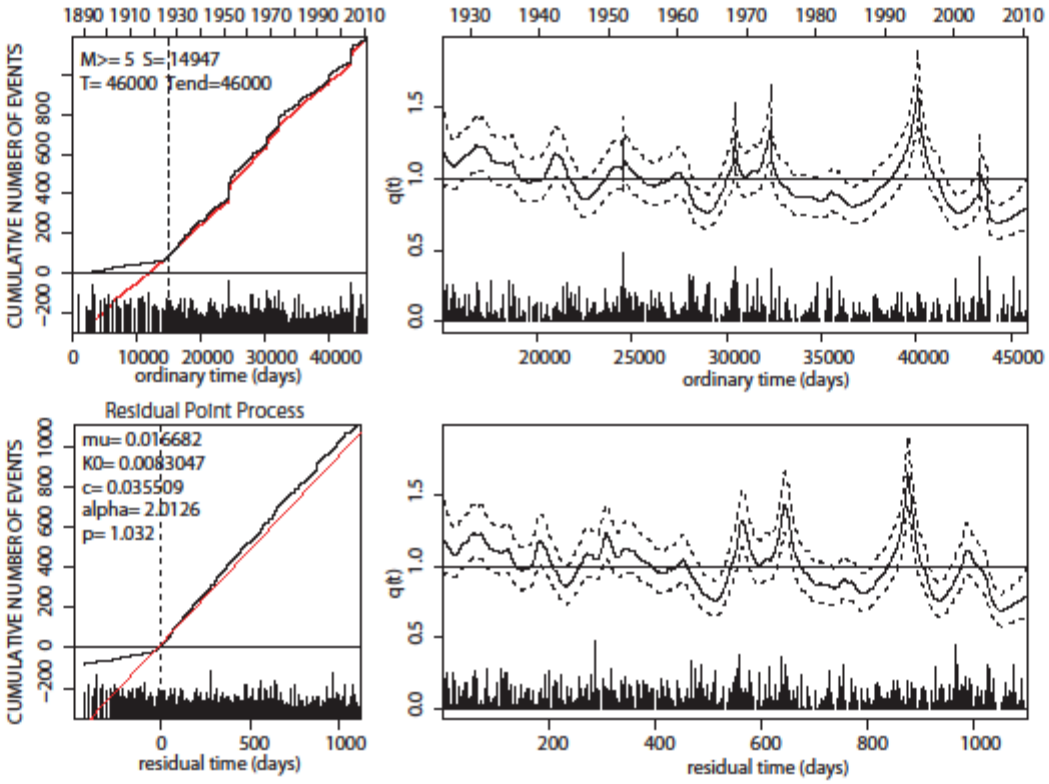

Figure 3-26.

(left): reference ETAS estimate from [S,T]=[14947, 46000], corresponding to the period from the beginning of 1926 to the end of 2010.

(right): misfit function $q_{\lambda}(t)$ under respectively ordinary (upper) and transformed (lower) time. The dashed lines show one σ error bars.

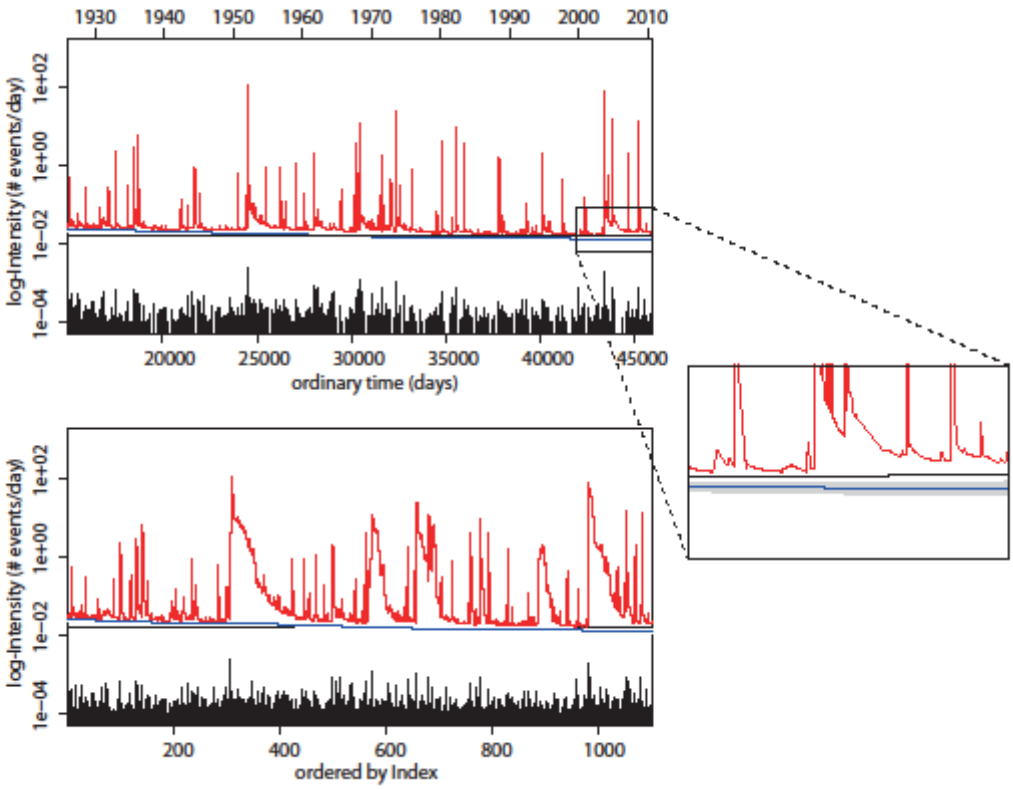

Figure 3-27. Estimated time variant background seismicity $\mu(t)$ in blue curve with gray band of one σ error bar, and the intensity $\lambda(t)$ in red curve, on the normal time (upper) and in the index order (lower). A small square in the upper panel is magnified in the right.

3-6. Seismicity triggered by the M9.0 Tohoku-Oki earthquake

The M9.0 Tohoku earthquake caused measurable crustal deformation throughout northeastern part of Japan as the result of slip on the 500 km long and 200 km wide seismic source [Wei et al., 2011]. Numbers of aftershocks, including four M>=7 and in-between seventy and eighty of M>=6 shocks have occurred during a month, and two M>=7 and around twenty of M>=6 in the following four months. The concern for triggered earthquake is paramount. To evaluate the potential impact of the Tohoku earthquake, we apply our methods to the earthquake data in selected small regions, to see if there were any seismic anomalies. The earlier report by Ogata and Kumazawa [2011] showed, with observing the first one month data after the M=9.0, normal activities (with respect to the ETAS model) in East Shizuoka, West Fukushima, and northern cluster of North Nagano, whereas some quiescence in Fukushima, Hamadoori

region. Here we extend the period a little more to cover the whole 2011.

3-6-1. East Shizuoka

An earthquake of magnitude 6.4 was occuured two days after the Tohoku earthquake. The data are taken from the rectangular region of Fig. 3-28, from the triggered earthquake to the end of 2011, with magnitude larger than 2.0.

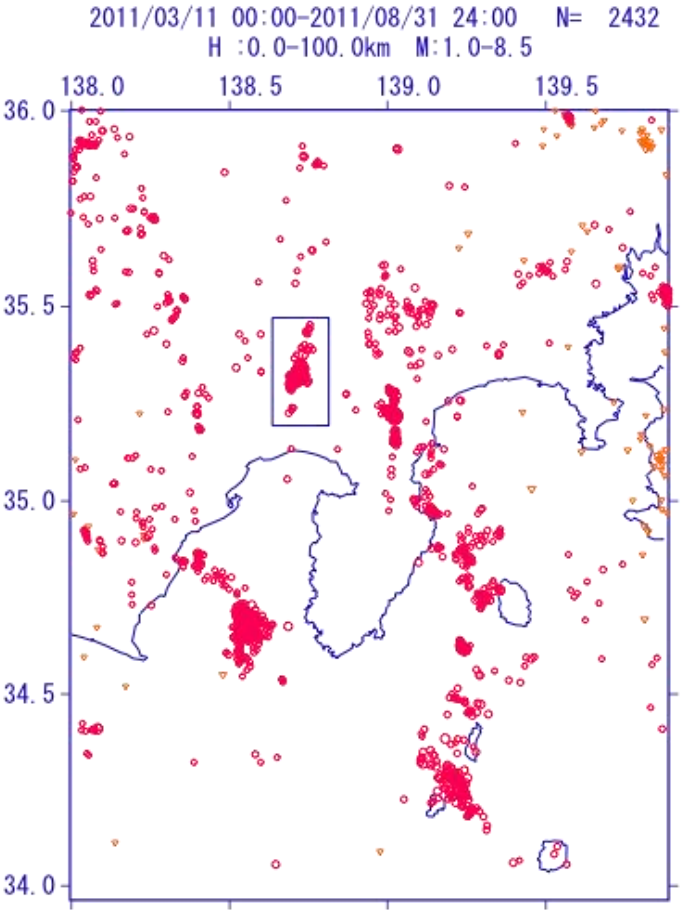

Figure 3-28. Earthquakes from 11 Mar 2011 to the end of 2011. The rectangle region is used in the analysis.

The left panel of Fig. 3-29 shows estimated reference ETAS. The ETAS fits well the observed triggered aftershocks. The misfit function $q_{\lambda}(t)$ remains one all over the period, meaning there is no misfit detected. The $\mu(t)$ in Fig. 2-30 also remains unchanged. Thus we could assume that the aftershocks are decaying normally as expected.

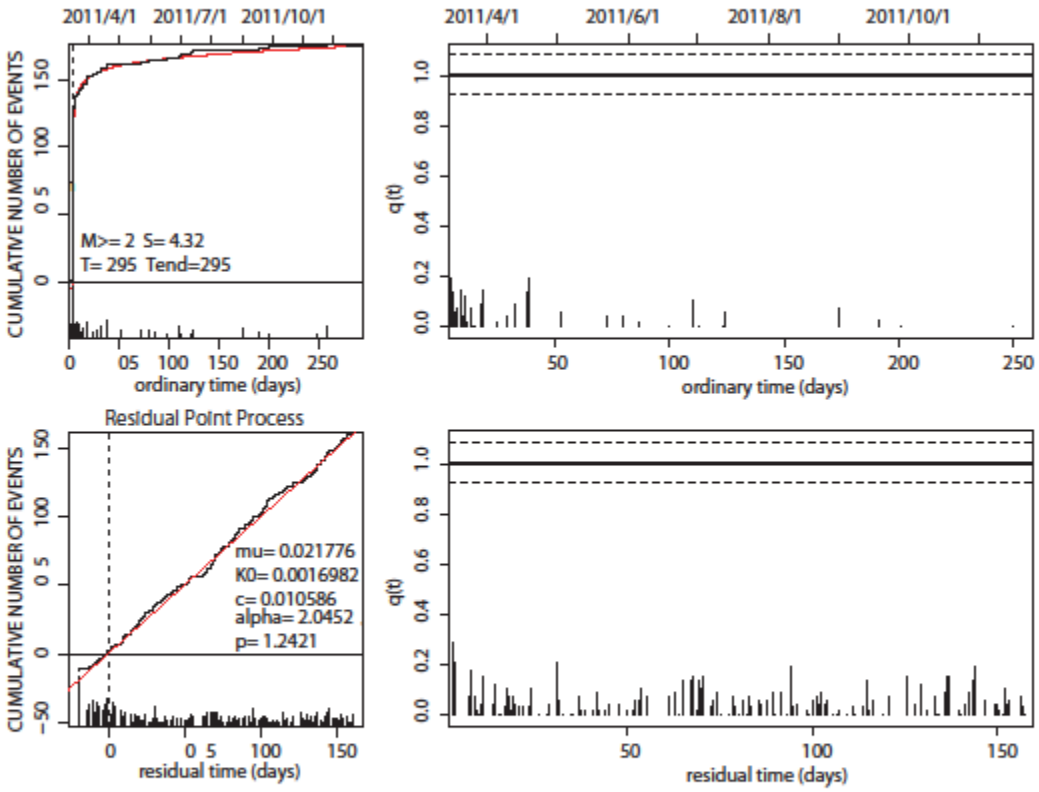

Figure 3-29.

(left): reference ETAS estimate from [S,T]=[4.32,295], corresponding to the period from 15 Mar 2011 to the end of 2011.

(right): misfit function $q_{\lambda}(t)$ under respectively ordinary (upper) and transformed (lower) time. The dashed lines show one σ error bars.

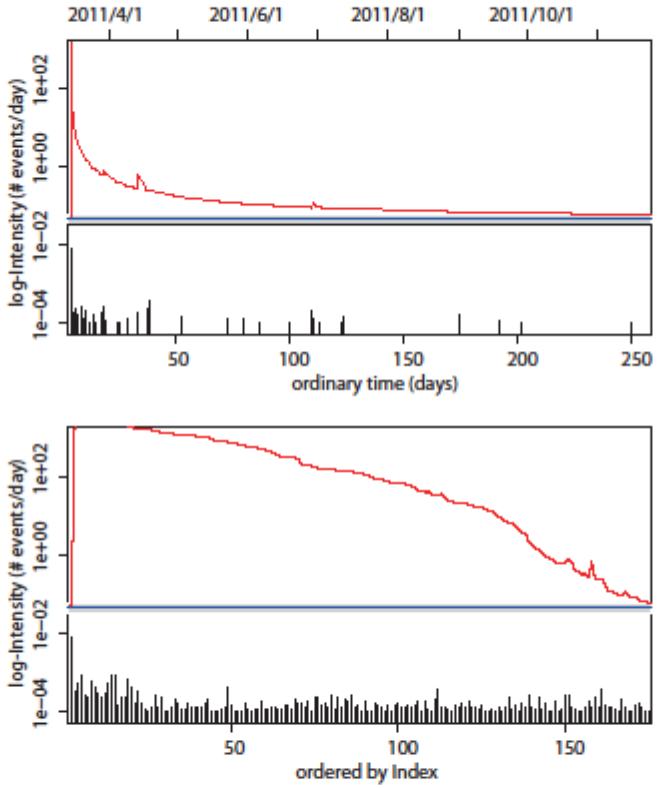

Figure 3-30. Estimated time variant background seismicity $\mu(t)$ in blue curve with gray band of one σ error bar, and the intensity $\lambda(t)$ in red curve, on the normal time (upper) and in the index order (lower). A small square in the upper panel is magnified in the right.

3-6-2. Western Fukushima

The data is taken from the rectangular region in Fig. 3-31, with the minimum Magnitude of 2.0 from 11 Mar 2011 to the end of 2011. Most of the earthquakes have magnitudes less than 3.0, with the largest being 4.5 on 12 Mar. Taking the reference parameters from around two months after the Tohoku earthquake; [S,T]=[75,295], one can see that the seismicity is notably high in the earlier a few months (Fig. 3-32), then stays normal in the remaining period. The $\mu(t)$ also show similar changes in Fig. 3-33.

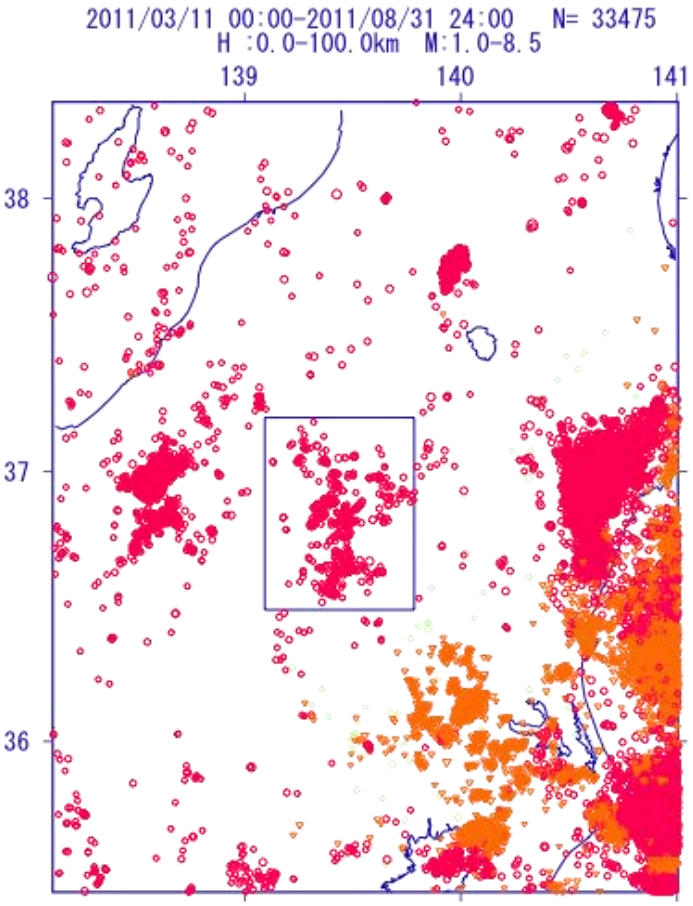
2011/03/11 00:00-2011/08/31 24:00 N= 33475
H :0.0-100.0km M:1.0-8.5
139
140
141
38
37
36

Figure 3-31. Earthquakes from 11 Mar 2011 to 2011. The rectangle region is used for the analysis.

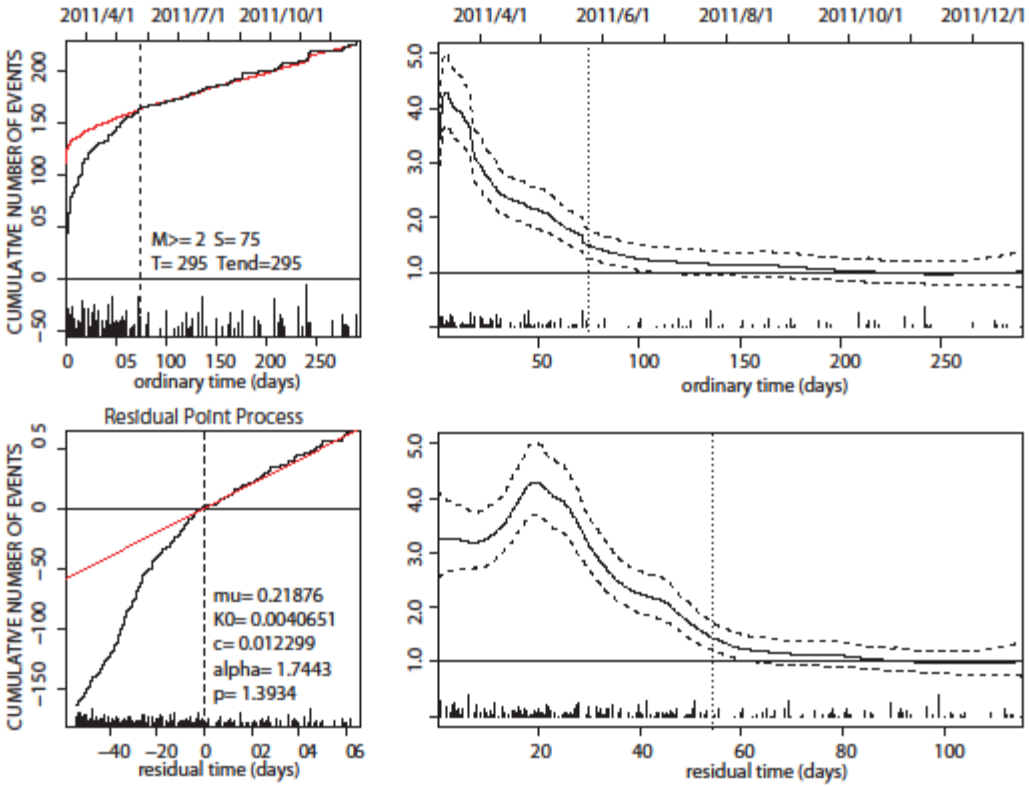

Figure 3-32.

(left): reference ETAS estimate from [S,T]=[75,295], corresponding to the period from the end of May to the end of 2011.

(right): misfit function $q_{\lambda}(t)$ under respectively ordinary (upper) and transformed (lower) time. The dashed lines show one σ error bars. The vertical dotted lines show the beginning of the reference period.

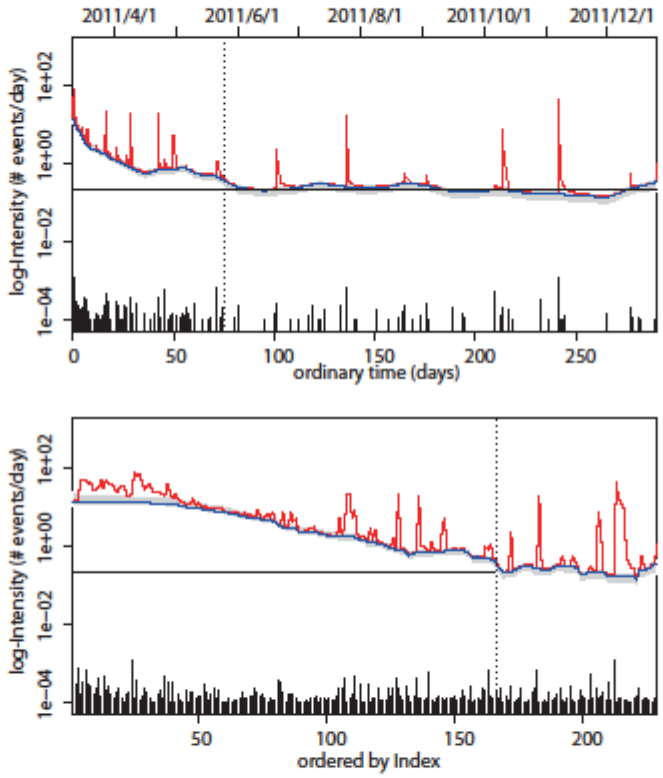

Figure 3-33. Estimated time variant background seismicity $\mu(t)$ in blue curve with gray band of one σ error bar, and the intensity $\lambda(t)$ in red curve, on the normal time (upper) and in the index order (lower). The vertical dotted lines show the beginning of the reference period.

3-6-3. Northern Nagano

The cluster in the northern Nagano is divided into two, north and south cluster (Fig. 3-34). The largest shock is of Magnitude 6.7 on 12 Mar, occurred in the north cluster. Most of the aftershocks in both clusters start after that. The cluster in the south, around mid April, shown in the time series of N-S cross-section (Fig 3-32 (c)) is due to the M5.6 on 12 Apr occurred in the south cluster.

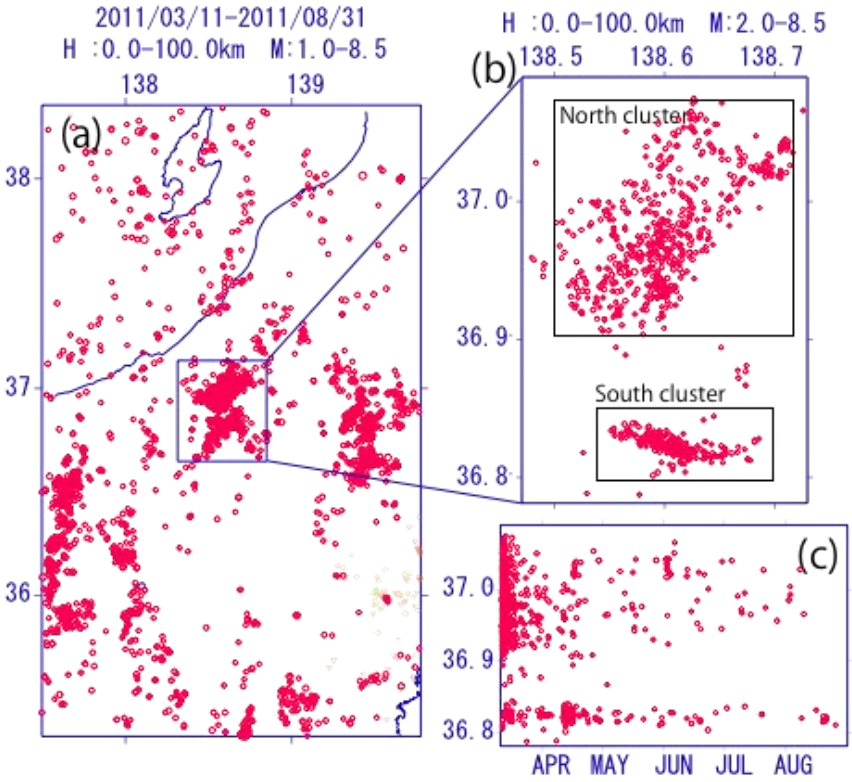

Figure 3-34. (a) Earthquakes of M>1.0. (b) Magnified view of earthquakes with M>2.0 from the rectangle region in the left panel. (c) Time series of North-South cross section of the upper panel.

3-6-3a. North cluster

First we examine the north cluster. The reference ETAS parameters estimated from the beginning of May to the end of 2011 fits quite well (Fig. 3-35 left), and the misfit function $q_{\lambda}(t)$ remains close to one over the corresponding period, indicating no anomalies observed. The $\mu(t)$ in Fig. 3-36 also shows no anomalies.

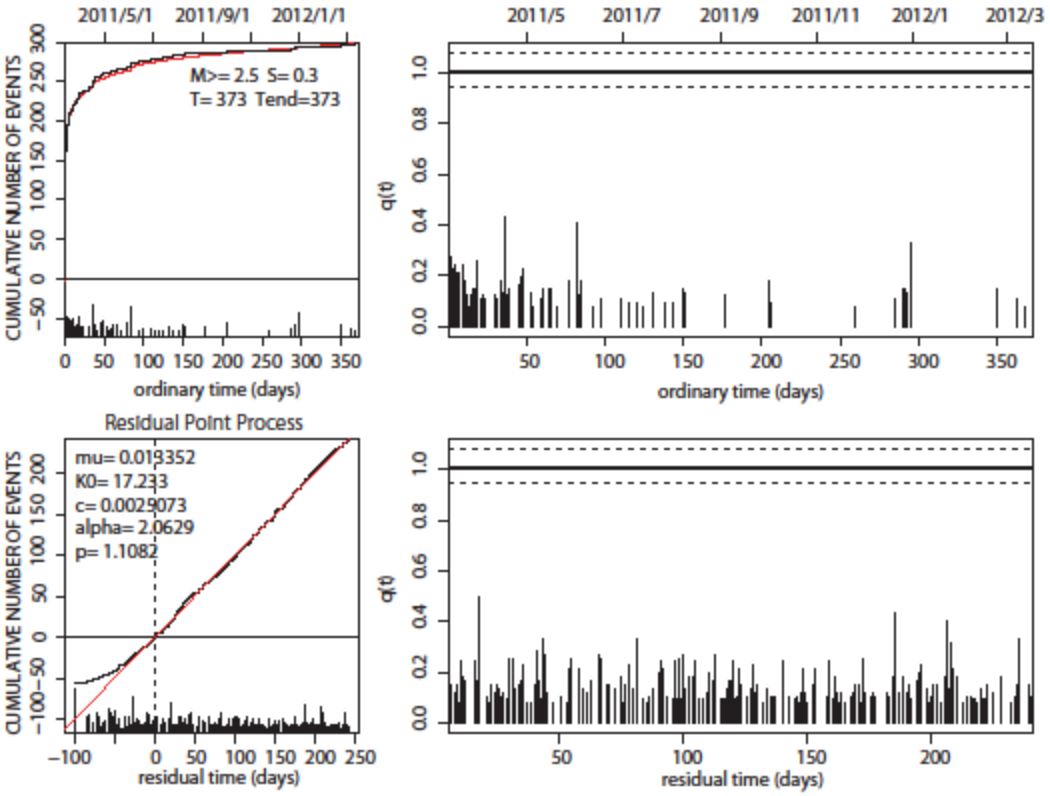

Figure 3-35.

(left): reference ETAS estimate from [S,T]=[50,295], corresponding to the period from the end of May to the end of 2011.

(right): misfit function $q_{\lambda}(t)$ under respectively ordinary (upper) and transformed (lower) time. The dashed lines show one σ error bars. The vertical dotted lines show the beginning of the reference period.

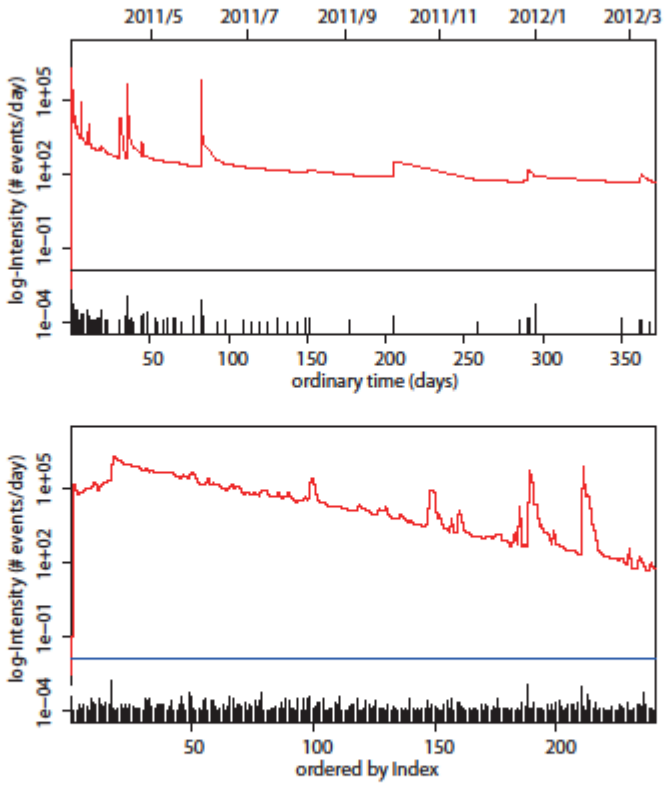

Figure 3-36. Estimated time variant background seismicity $\mu(t)$ in blue curve with gray band of one σ error bar, and the intensity $\lambda(t)$ in red curve, on the normal time (upper) and in the index order (lower). The vertical dotted lines show the beginning of the reference period.

3-6-4. North Nagano, south cluster

Fig. 3-37 left panel shows the reference ETAS fit, estimated from the same period as the previous example, from the beginning of May to the end of 2011. The misfit function $q_\lambda(t)$ with this reference in Fig. 3-37 shows steep increase in the seismicity in the first 50 days, then remains normal after that. The $\mu(t)$ in Fig. 3-38 has similar trend; the seismicity is high right after the Tohoku earthquake and after M5.6 at around 30.

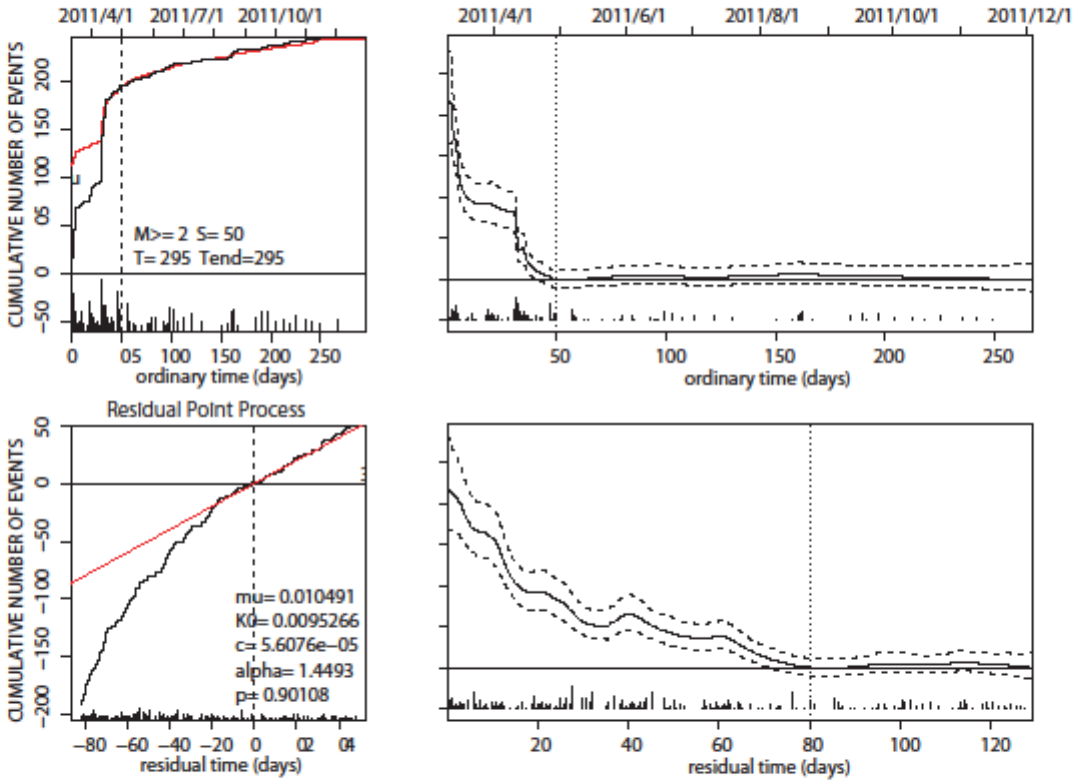

Figure 3-37.

(left): reference ETAS estimate from [S,T]=[50,295], corresponding to the period from the end of May to the end of 2011.

(right): misfit function $q_{\lambda}(t)$ under respectively ordinary (upper) and transformed (lower) time. The dashed lines show one σ error bars. The vertical dotted lines show the beginning of the reference period.

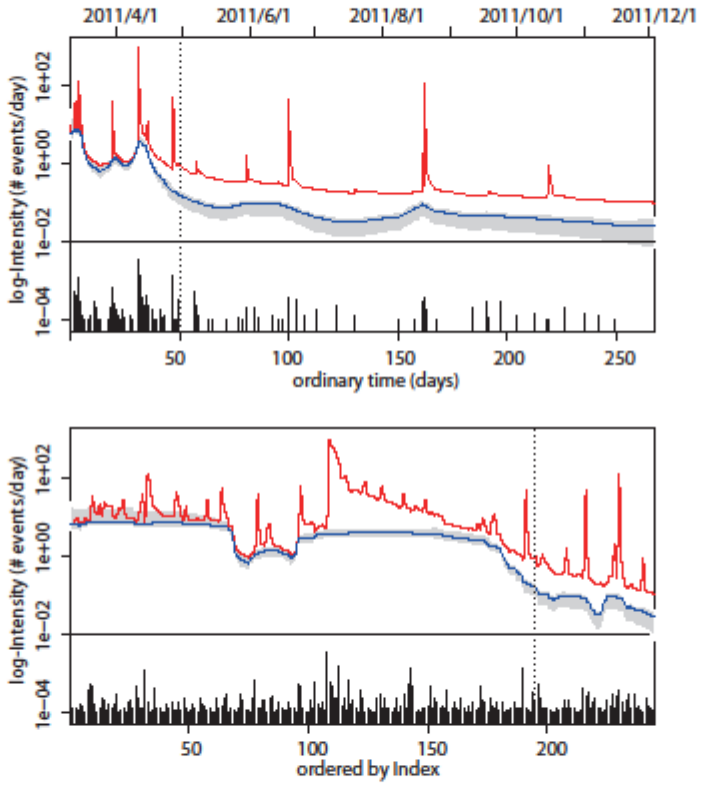

Figure 3-38. Estimated time variant background seismicity $\mu(t)$ in blue curve with gray band of one σ error bar, and the intensity $\lambda(t)$ in red curve, on the normal time (upper) and in the index order (lower). The vertical dotted lines show the beginning of the reference period.

3-6-5. Near the Lake Inawashiro

The data is taken from the rectangle region in Fig. 3-39. The suddenly started swarm on 18 Mar consists mostly of small earthquakes with magnitude less than 3.0. At around 50 days later, on 7 May, a relatively large shock with M4.6 occurred, and after that the aftershocks seems to have decayed normally. Assuming the sequence after the M4.6 as the normal seismicity in this region, the fit of reference ETAS estimate is shown in the left panel of Fig. 3-40. The misfit function $q_{\lambda}(t)$ in the right panel shows that the seismicity before the M4.6 is significantly higher. The changes in $\mu(t)$ in Fig. 3-41 is very close to it . For the earlier period before M4.6, Fig. 3-42 shows that the ETAS fits poorly, with small α value. This suggests the events lack noticeable triggering relationships. Such behavior is characteristic to swarm events.

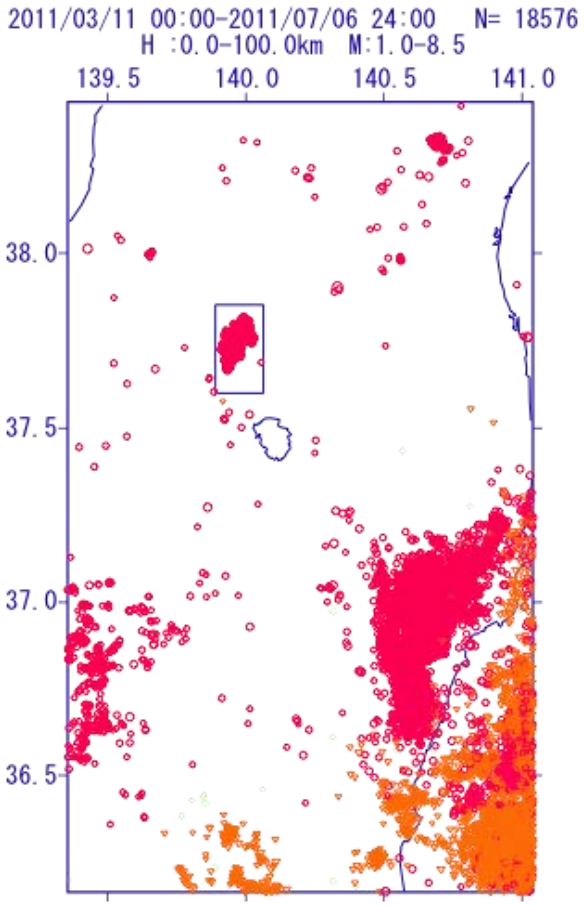

Figure 3-39. The earthquakes around lake Inawashiro.

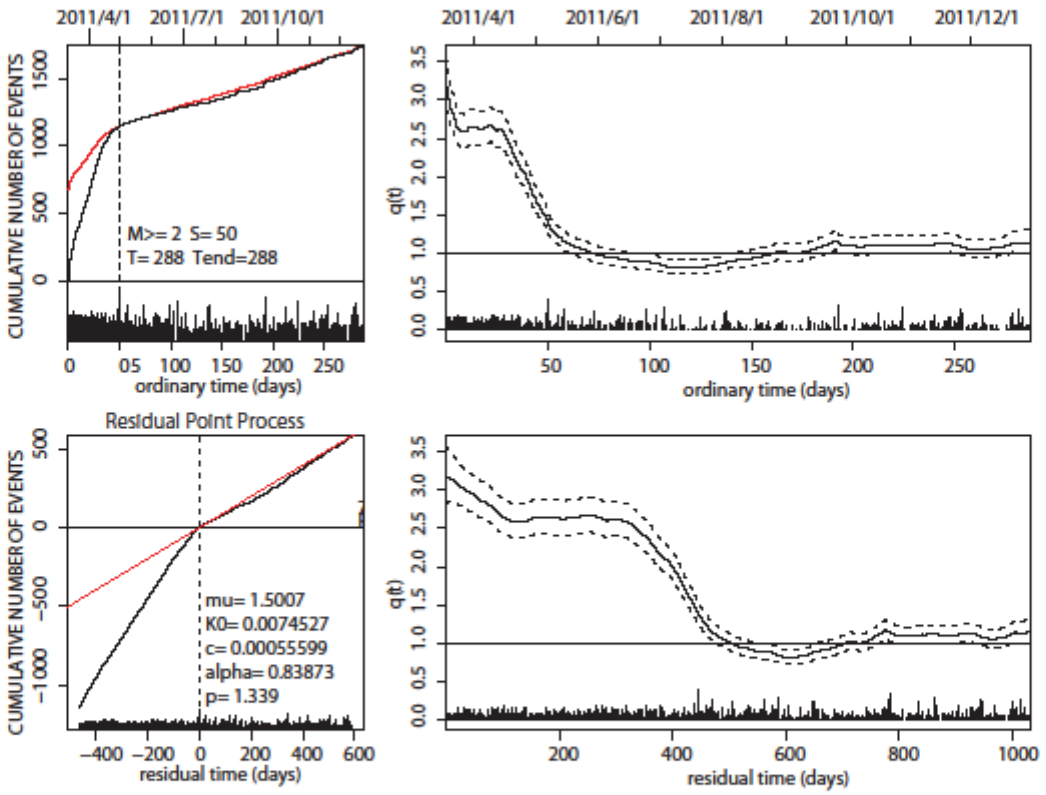

Figure 3-40.

(left): reference ETAS estimate from [S,T]=[50,288], corresponding to the period from the end of May to the end of 2011.

(right): misfit function $q_{\lambda}(t)$ under respectively ordinary (upper) and transformed (lower) time. The dashed lines show one σ error bars. The vertical dotted lines show the beginning of the reference period.

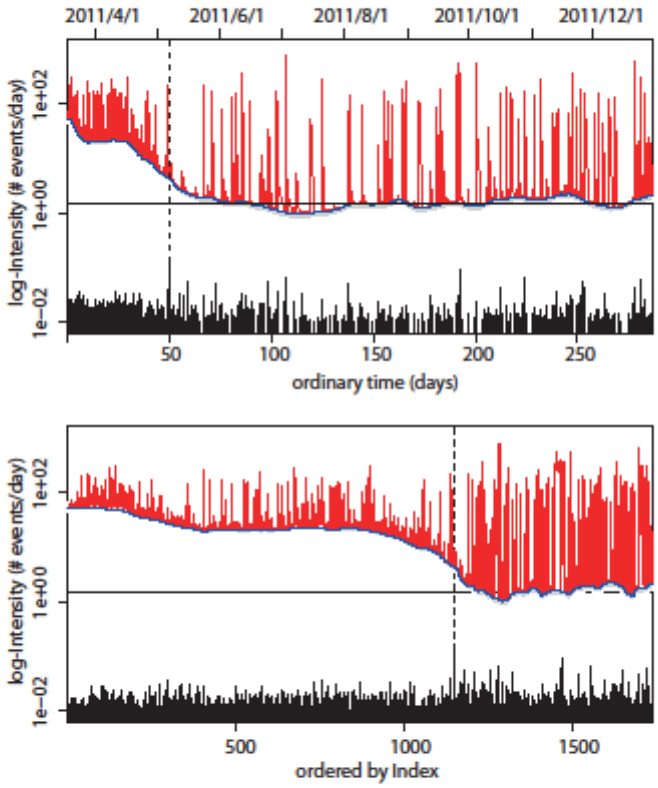

Figure 3-41. Estimated time variant background seismicity $\mu(t)$ in blue curve with gray band of one σ error bar, and the intensity $\lambda(t)$ in red curve, on the normal time (upper) and in the index order (lower). The vertical dotted lines show the beginning of the reference period.

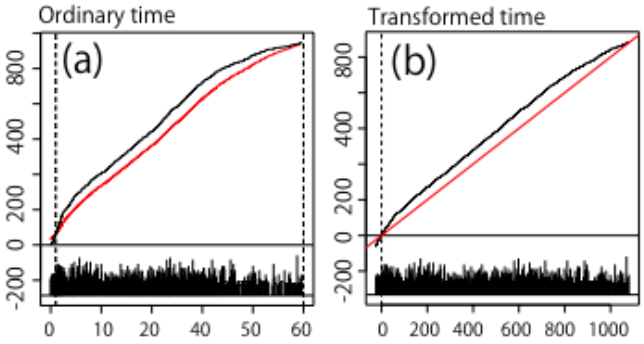

Figure 3-42. The parameter set (μ, K, c, α, p) = (0.0, 0.135, 0.243, 0.00542 1.000) is estimated from [S,T]=[1, 50].

3-6-6. Fukushima Hamadoori, or aftershocks of Iwaki earthquake of M7.0

This has been one of the most actively triggered region and there occurred numerous aftershock right after the M9.0 Tohoku earthquake, where formerly only limited number has been observed. The largest aftershock was so called the Iwaki earthquake of M7.0,

on 11 Apr, in the midst of this region in Fig. 3-43. Unlike the majority of earthquakes in inland Tohoku district (they usually have reverse faulting mechanisms), this event occurred on a normal fault.

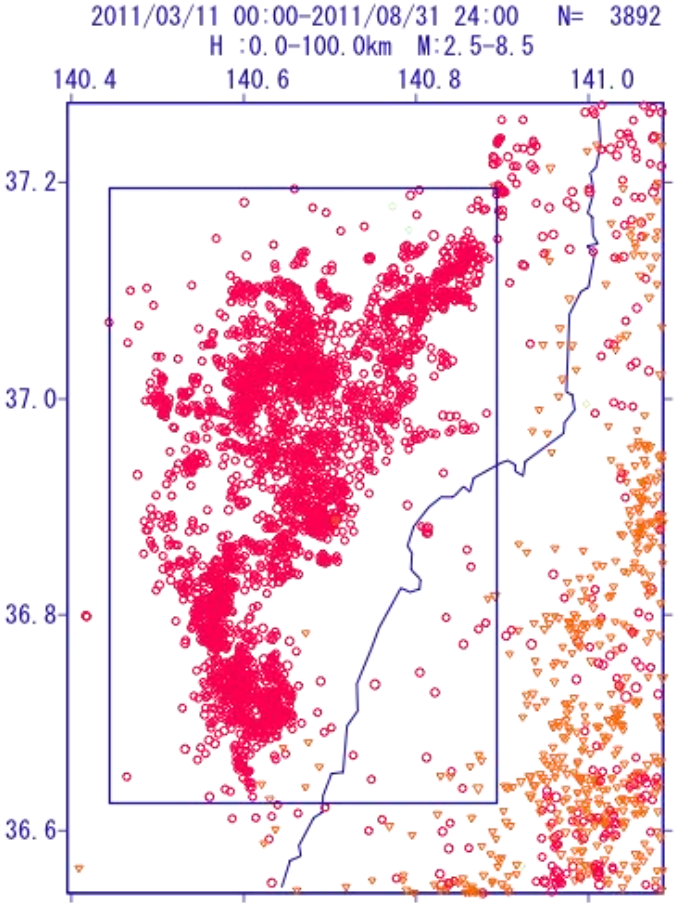

Figure 3-43. Earthquakes of M>2.5, in Fukushima Hamadoori.

The data to be examined is taken from the rectangular region in Fig. 3-43, with M >= 2.5. The ETAS estimation after the M7.0, at t=31.1, fits quite well and show little diversion (Fig. 3-44). Hence hereafter we narrow down our interest into the period before the M7.0.

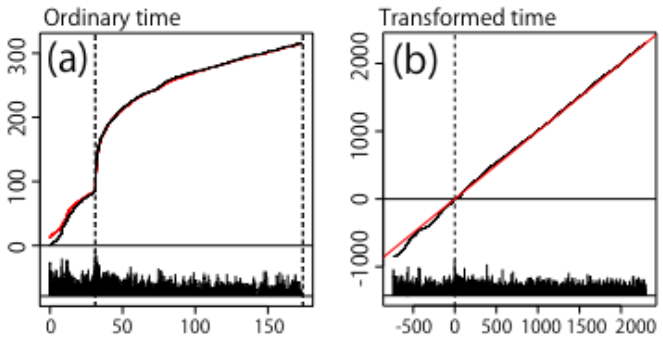

Figure 3-44. The parameter set (μ, K, c, α, p) = (1.0481, 21.667, 0.036732, 1.4513, 1.1780) is estimated from [S,T]=[31.1, 174].

Since this whole region spreads over the normal fault of M7.0, we separated the region into the upper and lower side of the fault, or into north and south cluster (Figure 3-45).

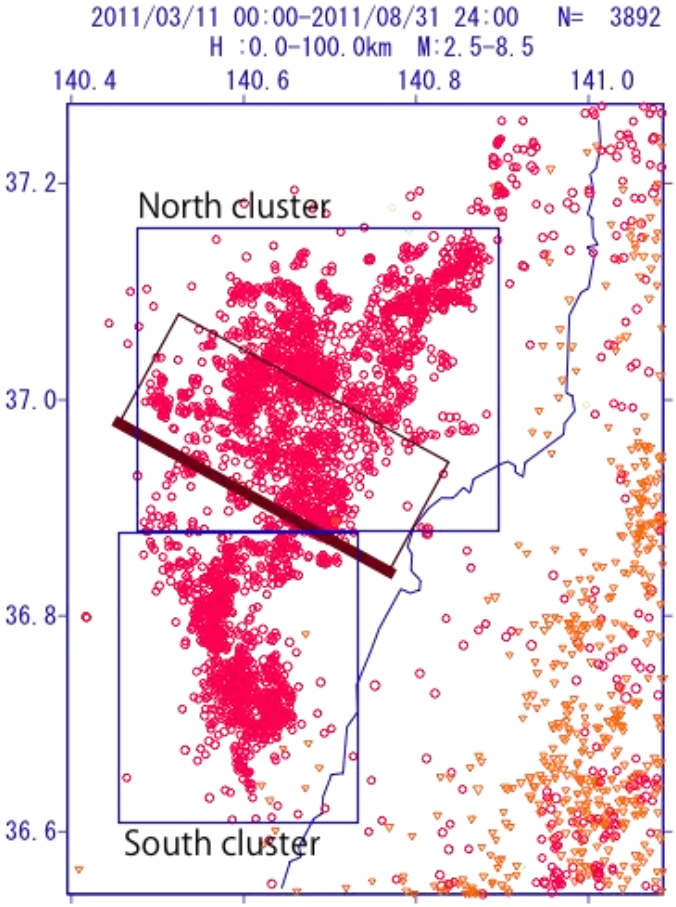

Figure 3-45. Zoning of north and south cluster. The brown rectangle represent rough location of the fault for the M7.0.

3-6-6a. North cluster

The change-point analysis shows that the change-point at T=23 is significant, with the AIC improvement by 2. Taking the period before the change-point as the reference, the $q_{\lambda}(t)$ and the $\mu(t)$ both decrease after the change-point (Fig. 3-46 and 47). The jump in the cumulative count (Fig. 3-46, upper left) correspond to M6.0 on 23 Mar.

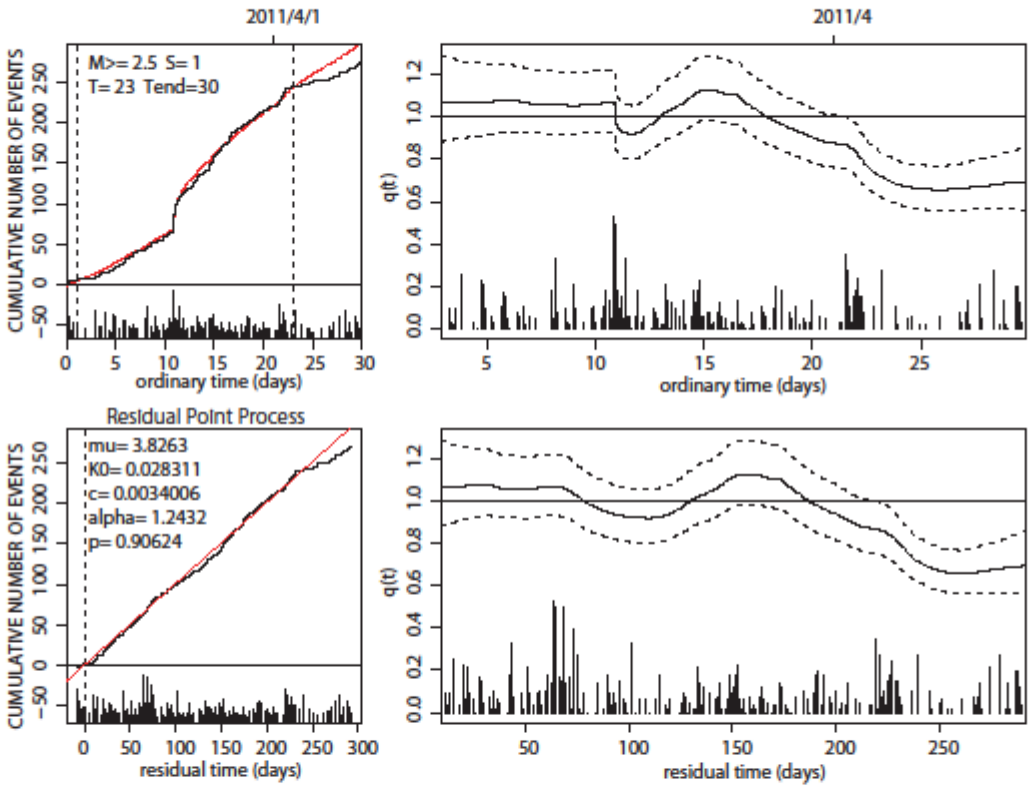

Figure 3-46.

(left): reference ETAS estimate from [S,T]=[0,23], corresponding to the period from 11 Mar 2011 to 3 Apr 2011.

(right): misfit function $q_{\lambda}(t)$ under respectively ordinary (upper) and transformed (lower) time. The dashed lines show one σ error bars. The vertical dotted lines show the beginning of the reference period.

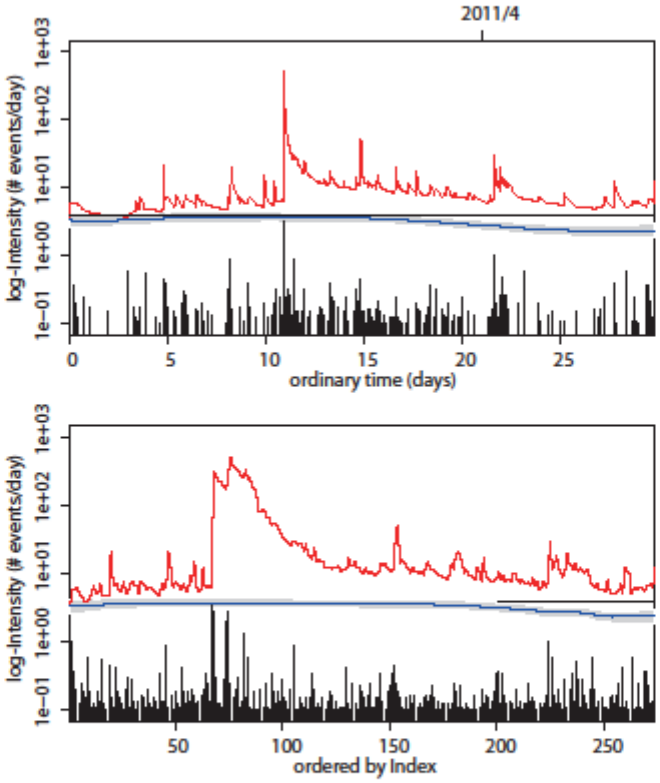

Figure 3-47. Estimated time variant background seismicity $\mu(t)$ in blue curve with gray band of one σ error bar, and the intensity $\lambda(t)$ in red curve, on the normal time (upper) and in the index order (lower).

3-6-6b. South cluster

The change point analysis shows that the change-point at T=18 is significant with improving the AIC by 3. Using the period before the change-point as the reference period, the $q_{\lambda}(t)$ and the $\mu(t)$ both decrease after the change-point (Fig. 3-48 and 49). The earlier jump in the cumulative curve (Fig 3-48, upper left) corresponds to M6.1 on 19 Mar. Before it, both misfit functions show slight quiescence.

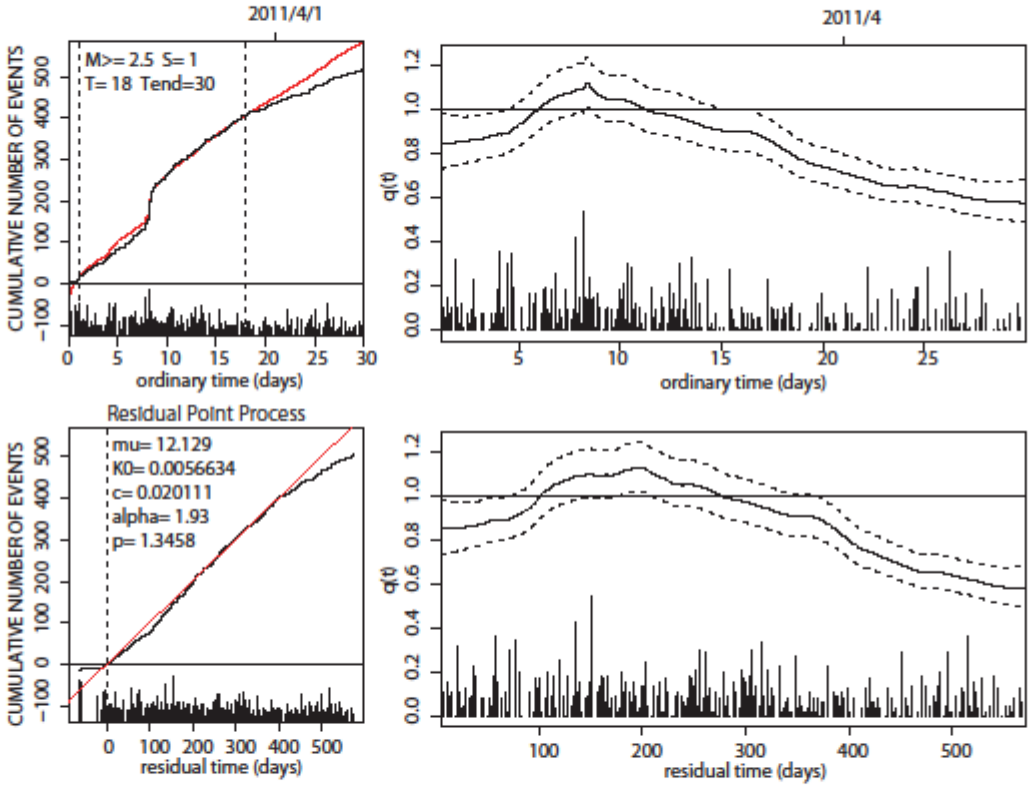

Figure 3-48.

(left): reference ETAS estimate from [S,T]=[0,30], corresponding to the period from 11 Mar 2011 to 11 Apr 2011.

(right): misfit function $q_{\lambda}(t)$ under respectively ordinary (upper) and transformed (lower) time. The dashed lines show one σ error bars. The vertical dotted lines show the beginning of the reference period.

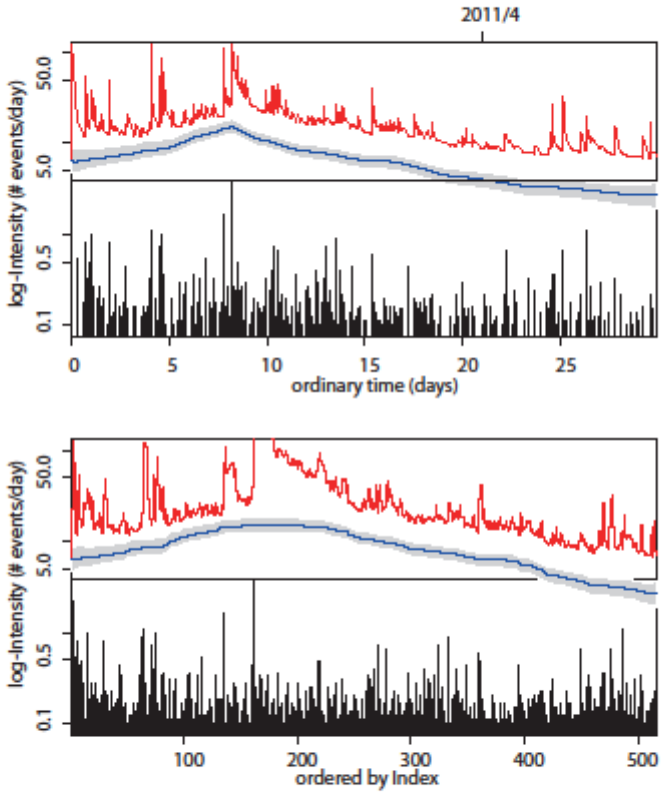

Figure 3-49. Estimated time variant background seismicity $\mu(t)$ in blue curve with gray band of one σ error bar, and the intensity $\lambda(t)$ in red curve, on the normal time (upper) and in the index order (lower).

3-7. Examination by Simulation

We have seen that, while the misfit function *q(t)* of the first method responds well to misfits in short periods as long as the periods contain enough number of events, the misfit function of the second method, or *μ(t)*, fails to capture those misfits when the optimal weight is also be estimated. This is mainly due to relatively short length of misfitted period, and the optimal weight *w* imposed upon roughness of the misfit function does not allow such short fluctuation. The question is, for gaining non-flat misfit function with optimal weight, what length of misfit (or anomaly) is required.

Using the parameters in the earlier example of Boso peninsula, (μ, K, c, α, p) = (0.032213, 0.02759, 0.0033756, 0.77455, 1.0479), we generated sequences of events from T=0 till T=5000 (days), that length of period is close to that of the Boso case. In addition, around the middle of that period, the background seismicityμis inflated. Fig. 3-50 is an example with 100 timesμin [3000, 3010], for 10 days. This period, 10 days out of 5000, and the amount of inflation roughly match the relative length and intensity

of swarms observed there. With 10 simulated data sets, with reference ETAS parameters estimated from [0,5000] for each data set, none shows non-flatμ(t). Even with 100 (days) of inflated period (Figure 3-51), none out of 10 shows such anomalies.

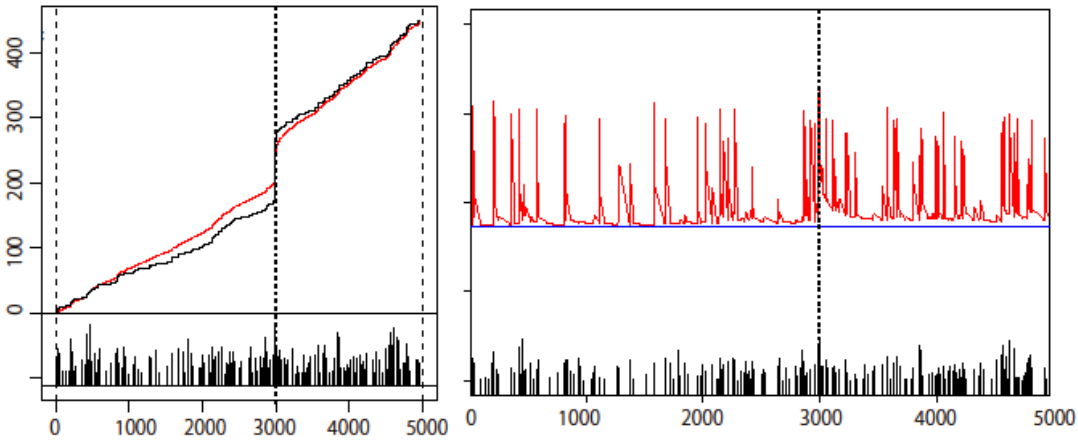

Figure 3-50. Simulated data with parameter of Boso peninsula. μis inflated 100 times in [3000, 3010]. (Left) Cumulative count in black curve and reference ETAS estimation in red. (Right) μ(t) (in blue) with the reference ETAS parameters. The dashed vertical lines around T=3000 are starting and ending of inflated period.

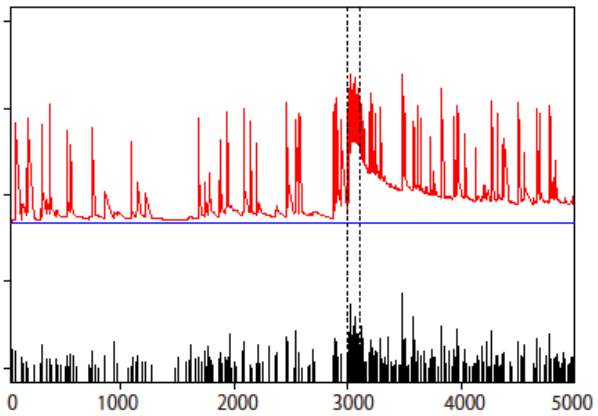

Figure 3-51. The result of μ(t) when μis inflated 100 times, for 100 days from T=3000 till 3100.

With the inflation period of one tenth of the entire period (500 days of 5000), 10 cases out of 10 simulations give μ(t)'s that reflect some of inflated background seismicity. One example is shown in Fig. 3-52. It turned out that the strength of inflation does not matter as much as relative length of the period, we used 10 time μfor the inflated periods, for keeping the computation fast enough.

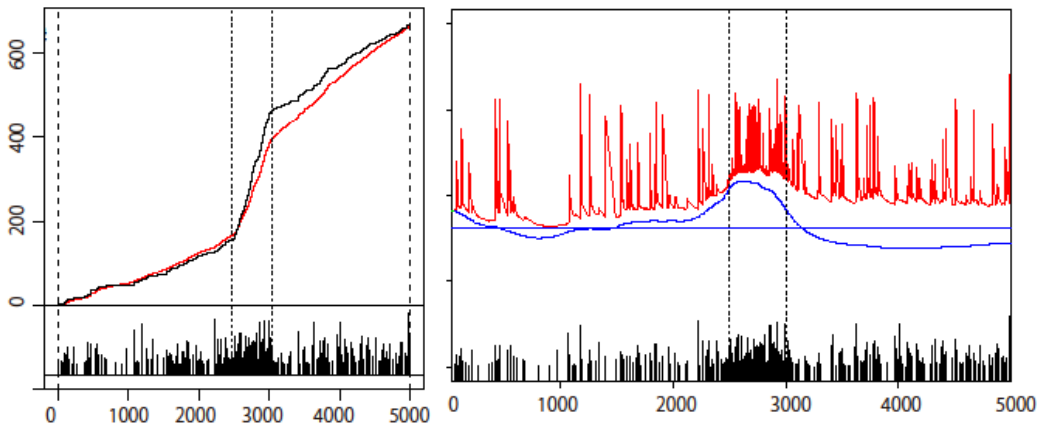

Figure 3-52. μ is inflated 10 times, for 100 days from T=2500 till 3000.

With the reference parameters estimated from the normal period (that is, non-inflation period), the μ(t) reacts anomaly of much shorter period. Fig. 3-53 shows μ(t) with reference parameters estimated before the inflation, which lasts only 30 days from T=3000. With such reference parameters, the length of 1/100 ensuresμ(t) to reflect inflations.

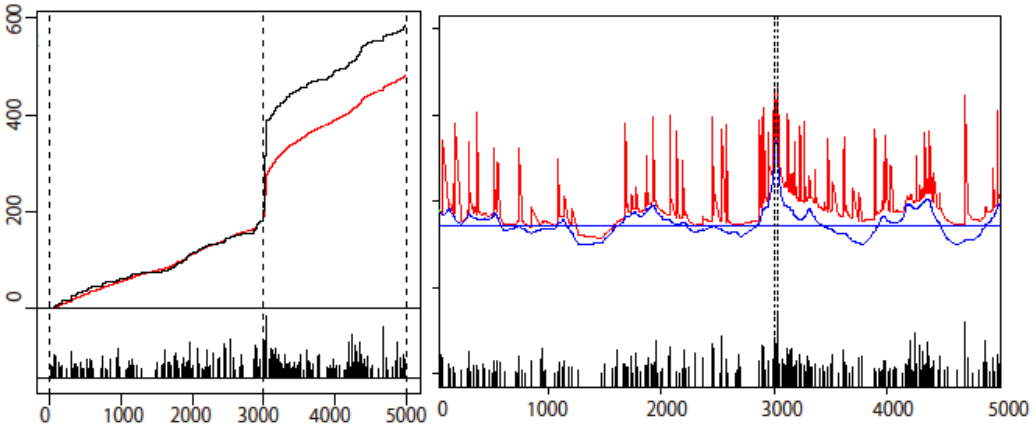

Figure 3-53. μ is inflated 100 times, for 30 days from T=3000 till 3030. The red curve in the right panel is the reference ETAS estimation from [0,3000].

Thus it turned out that in Boso case and many other cases, the periods of anomalies are too short for theμ(t)'s to react. In case we know what is normal, theμ(t) reflect anomalies much easily. The example of Tokyo Bay is an example for the latter case, in which the reference parameters are taken from the earlier period of what seems "normal".

3-8. Conclusions and discussions

In this chapter we have introduced two types of misfit functions which measure how a reference (or a baseline) ETAS model deviates from data. The misfit functions are estimated as the best modifiers within their own frameworks to the referencing models so that the models improve their fits in the best ways.

As the first misfit function, we consider a function $q_{\lambda}(t)$ that modifies the misfit of a referencing ETAS model by multiplying its intensity function $\lambda(t)$ by some numbers at points of event occurrences. Hence the $q_{\lambda}(t)$ in essence consists of a set of numbers which shall be multiplied to the reference intensity at points of events. We estimated this $q_{\lambda}(t)$ by Bayesian smoothing, under transformed time line so that we could evaluate the misfit within short period of time where events are dense. This extra step also makes the process of estimation a bit easier. One of the obvious weakness in this misfit function is that we could not identify by itself which parameter in the set of ETAS parameters is the major source of the misfit. All we could say is the intensity as a whole is strengthened or weakened at certain periods of time.

As the second misfit, we use a time variant background seismicity $\mu(t)$ as the modifier to a reference ETAS model. Although it would be possible to adopt time-dependence to each of the ETAS parameters simultaneously and independently, the background seismicity μalone would be a plausible choice because this parameter is most likely to vary and sensitive to unusual events such as slow slips and volcanic activities. As such, a change in this parameter is most easily connected to or explained by physical events. The estimation is by Bayesian smoothing on normal time line. The method estimates both the $\mu(t)$ and the optimal weight of smoothness together, hence it tends to make the estimated $\mu(t)$ flat in compensation for very heavy weight of smoothness, especially when there is a misfit in short period. Narrowing down the period of interest or choosing “normal” period for the reference estimation can get around this problem.

In the applications to the data with swarms in Boso peninsula, in section 3-4, the first type of misfit function $q_{\lambda}(t)$ showed clear peaks at known swarms, for example in 2002 and 2007. The time variant background seismicity $\mu(t)$ merely showed more rough trend.

Narrowing the period of interest allowed us to see the details of background changes. The applications to the data of Tokyo Bay showed increase in seismicity in recent a few years with both of the methods. By narrowing down the period of interest or choosing better reference, the methods showed more detailed changes.

The method then applied to the data sets before the M9.0 Tohoku earthquake, from largely divided regions all over Japan, with magnitude equal or larger than 5.0 for over 100 years. Since the data sets range over very long period, they potentially contain multiple change points. This may make the change-point method in chapter 2 difficult to be applied here. The misfit function $q_{\lambda}(t)$ in each region showed relative quiescence before the M9.0 Tohoku earthquake. They showed to some extent peaks at some of large earthquake. This is probably because the region does not covers main shock or the reference parameters are estimated as an average of a long period, or maybe because there is a true activation. The $\mu(t)$ also showed the quiescence, but failed to capture the detailed changes or misfit which the $q_{\lambda}(t)$ showed, probably because the period of those changes are relatively too short.

Lastly the method is used to some of the clusters triggered by the Tohoku earthquake, in the northwestern region of Japan. The change-point method is used to a few cases too. The main purpose for these applications is to check if there are any noticeable anomalies in seismicity, and to raise caution or pat attention if any. The cluster in east Shizuoka shows normal decay of aftershock sequence triggered by M6.4. The cluster in west Fukuoka showed high seismicity at first then dropped .

The northern and southern clusters in north Nagano had opposite trend. The northern cluster had lowered seismicity at first. This is probably due to missing of small events. The southern cluster showed high seismicity at first, probably due to the triggering by a large event in the north. The seismicity in the both had been normal in the later period. The cluster in Inawashiro has an interesting property. The swarm started a week after the Tohoku earthquake. In fifty days a M4.6 occurred and then the seismicity has been back to normal. During the time lag of a week, underground water might have sneaked inside the fault there and lowered its friction, thus the following swarms might have triggered. In Hamadoori, Fukushima, the aftershocks of M7.0 on 11 Apr have decayed

normally without anomalies. Before the M7.0, the north cluster or the cluster on the upper side of the fault shows quiescence in both of the misfit functions, and it is also significant by the change-point method.

Thus the misfit functions could indicate potential anomalies based on a reference ETAS model, or on what thought to be a normal seismicity. Note these functions do not point out that an anomaly is there, for example by consulting statistical significance or a test. They simply describe what should be suspected, hence according support, physical or another statistical method, must be followed to confirm an anomaly. The functions can tell if there is a swarm, for example. But to relate this swarm to a slow slip event requires analysis of crustal deformation.

4. Conclusion

We have seen the cases when the ETAS model fails to fit to the data of earthquake sequence. By considering the way the fit could be improved, by the change-point method in chapter2 and by two types of misfit functions in chapter3, we could tell when and how the misfit is involved. The ETAS model is a well-build model that fits an earthquake sequence very well if the triggering effects are in some sense stable and closed within the data, hence any misfit of it should be attributed to either internal or external disturbances, ΔCFS or change in friction rate for example, to those triggering mechanisms or the way the data are taken. Capturing such disturbances are key ingredients for the forecasting purpose. As such examining misfits in the ETAS model serves its own essential part in understanding the earthquake triggering mechanisms, and such a difficult problem as earthquake forecasting,

Acknowledgements

It is my great pleasure and privilege to express my sincere gratitude to my revered supervise Professor Yosihiko Ogata of the Department of Statistical Science, the Graduate University for Advanced Studies (SOKENDAI) and the Institute of Statistical Mathematics (ISM) for his indispensable supervision, constant encouragement, untiring efforts, hearty support and thoughtful suggestions during the entire phase of my PhD

normally without anomalies. Before the M7.0, the north cluster or the cluster on the upper side of the fault shows quiescence in both of the misfit functions, and it is also significant by the change-point method.

Thus the misfit functions could indicate potential anomalies based on a reference ETAS model, or on what thought to be a normal seismicity. Note these functions do not point out that an anomaly is there, for example by consulting statistical significance or a test. They simply describe what should be suspected, hence according support, physical or another statistical method, must be followed to confirm an anomaly. The functions can tell if there is a swarm, for example. But to relate this swarm to a slow slip event requires analysis of crustal deformation.

4. Conclusion

We have seen the cases when the ETAS model fails to fit to the data of earthquake sequence. By considering the way the fit could be improved, by the change-point method in chapter2 and by two types of misfit functions in chapter3, we could tell when and how the misfit is involved. The ETAS model is a well-build model that fits an earthquake sequence very well if the triggering effects are in some sense stable and closed within the data, hence any misfit of it should be attributed to either internal or external disturbances, ΔCFS or change in friction rate for example, to those triggering mechanisms or the way the data are taken. Capturing such disturbances are key ingredients for the forecasting purpose. As such examining misfits in the ETAS model serves its own essential part in understanding the earthquake triggering mechanisms, and such a difficult problem as earthquake forecasting,

Acknowledgements

It is my great pleasure and privilege to express my sincere gratitude to my revered supervise Professor Yosihiko Ogata of the Department of Statistical Science, the Graduate University for Advanced Studies (SOKENDAI) and the Institute of Statistical Mathematics (ISM) for his indispensable supervision, constant encouragement, untiring efforts, hearty support and thoughtful suggestions during the entire phase of my PhD

normally without anomalies. Before the M7.0, the north cluster or the cluster on the upper side of the fault shows quiescence in both of the misfit functions, and it is also significant by the change-point method.

Thus the misfit functions could indicate potential anomalies based on a reference ETAS model, or on what thought to be a normal seismicity. Note these functions do not point out that an anomaly is there, for example by consulting statistical significance or a test. They simply describe what should be suspected, hence according support, physical or another statistical method, must be followed to confirm an anomaly. The functions can tell if there is a swarm, for example. But to relate this swarm to a slow slip event requires analysis of crustal deformation.

4. Conclusion

We have seen the cases when the ETAS model fails to fit to the data of earthquake sequence. By considering the way the fit could be improved, by the change-point method in chapter2 and by two types of misfit functions in chapter3, we could tell when and how the misfit is involved. The ETAS model is a well-build model that fits an earthquake sequence very well if the triggering effects are in some sense stable and closed within the data, hence any misfit of it should be attributed to either internal or external disturbances, ΔCFS or change in friction rate for example, to those triggering mechanisms or the way the data are taken. Capturing such disturbances are key ingredients for the forecasting purpose. As such examining misfits in the ETAS model serves its own essential part in understanding the earthquake triggering mechanisms, and such a difficult problem as earthquake forecasting,

Acknowledgements

It is my great pleasure and privilege to express my sincere gratitude to my revered supervise Professor Yosihiko Ogata of the Department of Statistical Science, the Graduate University for Advanced Studies (SOKENDAI) and the Institute of Statistical Mathematics (ISM) for his indispensable supervision, constant encouragement, untiring efforts, hearty support and thoughtful suggestions during the entire phase of my PhD

research. He taught me the basic concept of point process, seismology, programming by Fortran, and everything that was indispensable of my work. He also supported me financially by offering a position of research assistance for the almost entire duration of my study. With his own heavy research workload, he generously spent much time in instructing me; without it I could hardly finish my PhD program. To his generosity my gratitude is unbound. His sincere attitude toward his research subjects, his tireless hard work and his pragmatism against difficult problems are what stroke me the most.

I am grateful to Professor Zhuang Jiancang of SOKENDAI and ISM for his various academic suggestions and timely advices especially when I was in trouble in my work. I am very thankuful to Ms. Akiko Kutsuna, technical staff of ISM, for her support on office works, and nice cups of coffee in every evening. I am also thankful to Professor Mitsuhiro Matsu-ura for his evocative suggestions and advices on seismology around the coffee breaks. I cannot thank enough to Koichi Katsura of technical engineer for his professional support on my poor programming.

I am very much grateful to Professor Shinji Toda of Kyoto University, Disaster Prevention Research Institute, for his invaluable advices and suggestions to my paper and dissertation thesis on his professional view on Coulomb stress changes and on mechanisms of seismicity. I am grateful to Professor Satoshi Ide of Tokyo Univercity, school of science, for his critical advices in the preliminary screening of my dissertation. I cannot show enough of my gratitude to Professor Yoshiyasu Tamura of SOKENDAI and ISM, Professor Toda, Professor Ide, and Professor Zhuang for joining my committee of my PhD program and for sparing much of their overloaded time to come a long way to attend my dissertation.

We have used hypocenter data provided by JMA, together with the TSEIS visualization program package [*Tsuruoka*, 1996] for their visualization and also the PC program MICAP-G [*Naito and Yoshikawa*, 1996] for spatial visualization of Coulomb stress changes. For the crustal changes, we used the daily-measured GPS data provided by the Geographical Survey Institute of Japan [*GSI*, 2009]. Kunihiko Shimazaki, the chair person of the Earthquake Prediction Coordinating Committee, and the GSI kindly let us know about the geodetic anomaly at Kurikoma2 station. This study is partly supported by the Japan Society for the Promotion of Science under Grant-in-Aid for Scientific Research no. 20240027; and by the 2009 to 2011 projects of

the Institute of Statistical Mathematics and the Research Organization of Information and Systems at the Transdisciplinary Research Integration Center, Inter-University Research Institute Corporation.

<Inference>

Akaike, H. (1973), Information theory and an extension of the maximum likelihood principle, *2nd International Symposium on Information Theory*, Petrov and Csaki, eds., Akademiai Kiado, Budapest, 267-281.

Akaike, H. (1974), A new look at the statistical model identification. *IEEE Transactions* **AC-19**, 716–723.

Akaike, H. (1977), On entropy miximisation principle. *Proc. Symp. on Applications of Statistics*, 27-47.

Akaike, H. (1978a), A Bayesian analysis of the minimum AIC procedure, *Ann. Inst. Statist. Math.*, **30**, Part A, 9-14.

Akaike, H. (1978b), On the likelihood of a time series model, *J. Roy. Statist. Soc. Ser. D* (*The Statistician*), **27**, 217-235

Akaike, H. (1985), Prediction and entropy, in *A Celebration of Statistics, The ISI Centenary Volume,* edited by A. C. Atkinson and S. E. Feinberg. Springer-Verlag, New York. 1-24.

Aki, K., Maximum likelihood estimate of *b* in the formula log *N=a-bM* and its confidence limits, *Bull. Earthq. Res. Inst.*, **43**, 237-239, 1965.

Adelfio, Giada and Ogata, Yosihiko (2010), Hybrid kernel estimates of space-time earthquake occurrence rates using the epidemic-type aftershock sequence model, *Ann Inst Stat Math 62:127-143*.

Asano, K. and T. Iwata (2008), Kinematic source rupture process of the 2008 Iwate-Miyagi Nairiku earthquake, a M_W 6.9 thrust earthquake in northeast Japan, using strong motion data, *EOS Trans. Am. Geophys. Union*, **89** (53), Fall meeting Suppl. Abstract S23B-1890.

Beeler, N.M. and D.A. Lockner (2003), Why earthquakes correlate weakly with the solid Earth tides: Effects of periodic stress on the rate and probability of earthquake occurrence, *J. Geophys. Res. 108*, B8, 2391, doi:10.1029/2001JB001518.

Boltzmann, L. (1878), Weitere Bemerkungen uber einige Plobleme der mechanischen Warmetheorie, *Wiener Berichre.* **78**. 7-46.

Chernoff, H. and H. Rubin (1956), *The estimation of the location of a discontinuity in density. Proc. Third Berkeley Symp. On Math. Statist. And Prob.,* **1,** *Univ. of Calif. Press,* 19-37

Daley, D. J., and D. Vere-Jones (2003), *An Introduction to the Theory of Point Processes*, vol. 1, 2nd ed., Springer, New York.

Dieterich, J.H. (1988), Nucleation and triggering of earthquake slip: Effect of periodic stresses, *Tectonophysics 144*, 127– 139.

Dieterich, J. (1994), A constitutive law for rate of earthquake production and its application to earthquake clustering, *J. Geophys. Res.*, 99, 2601-2618.

Dieterich, J., V. Cayol and P. G. Okubo (2000), The use of earthquake rate changes as a stress meter at Kilauea volcano, *Nature*, 408, 457-460.

Evison, F. F. (1977), The precursory earthquake swarm, *Phys. Earth Planet. Inter*. *15*, 19-23.

GSI (2004), Crustal movement in Tohoku District, *Rep. Coord. Comm. Earthq. Predict*., 71, 279–329, Tsukuba, Japan.

GSI (2008), *GPS stations detect crustal deformation caused by the Iwate-Miyagi Nairiku Earthquake in 2008*. http://www.gsi.go.jp/ENGLISH/page_e30283.html

GSI (2009a), Crustal Movement of Japan Web Page. http://mekira.gsi.go.jp/ENGLISH/, http://mekira.gsi.go.jp/.

GSI (2009b), Crustal Movements in the Tohoku District, *Rep. Coord. Comm. Earthq. Predict*., 81, 208–263, Tsukuba, Japan.

GSI (2010), Crustal movement in Tohoku District, *Rep. Coord. Comm. Earthq. Predict*., 83, 59-81, Tsukuba, Japan.

Harris, R. A. (1998), Introduction to special section: Stress triggers, stress shadows, and implications for seismic hazard, *J. Geophys. Res.*, 103, 24347-24358.

Harris, R. A., and R. W. Simpson (1998), Surpression of large earthquakes by stress shadows: A comparison of Coulomb and rate-state failure, *J. Geophys. Res*., 103, 24,439-24,451.

Hirose, H. (2008), A simple fault model of the 2008 Iwate-Miyagi inland earthquake based on a permanent displacement estimated from a KiK-net accelerogram and GEONET GPS displacements, *Rep. Coord. Comm. Earthq. Predict*., 81, 156–157, Tsukuba, Japan.

Ichikawa, M. (1971), Reanalyses of mechanism of earthquakes which occurred in and near Japan, and statistical studies on the nodal plane solutions obtained, 1926-1968, *Geophys. Mag.* (Tokyo), *35*, 207-274.

Iinuma, T., M. Ohzono, Y. Ohta, S. Miura, M. Kasahara, H. Takahashi, T., Sagiya,3 T. Matsushima, S. Nakao, S. Ueki, K. Tachibana, T. Sato, H. Tsushima, K. Takatsuka, T. Yamaguchi, M. Ichiyanagi, M. Takada, K. Ozawa, M. Fukuda, Y. Asahi, M. Nakamoto, Y. Yamashita, and N. Umino (2009), Aseismic slow slip on an inland active fault triggered by a nearby shallow event, the 2008 Iwate-Miyagi Nairiku Earthquake (Mw6.8), *Geophys. Res. Lett*. 36, L20308, doi:10.1029/2009GL040063.

Inouye, W. (1965), On the seismicity in the epicentral region and its neighborhood before the Niigata earthquake (in Japanese), *Kenshin-jiho* (*Q. J. Seismol.*), *29*, 139-144.

JMA (2008), Report for the interview of the chairperson of the Coordinating Committee for Prediction of Volcanic Eruptions (8 October 2008), http://www.jma.go.jp/jma/press/0910/05a/yochiren091005.html, Otemachi, Tokyo.

JMA (2009), *The Annual Seismological Bulletin of Japan for 2008*.

Kanamori, H., and L. Astiz (1985), The Akita-Oki earthquake (Mw= 7.8) and its implications for systematics of subduction earthquakes, *Earthq. Pred. Res*., 3, 305–317.

Keilis-Borok, V. I., and L. N. Malinovskaya (1964), One regularity in the occurrence of strong earthquakes, *J. Geophys. Res*., 70: 3019-3024.

King, G. C. P., R. S. Stein and J. Lin (1994), Static stress changes and the triggering of earthquakes, *Bull. Seismol. Soc. Am.*, 84, 935 - 953.

Kisslinger, C. (1988), An experiment in earthquake prediction and the 7th May 1986 Andreanof Islands Earthquake. *Bull. Seismol. Soc. Am*., *78*, 218-229.

Kumazawa, T., Y. Ogata, and S. Toda (2009a), Seismicity rate changes prior to the 2008 Iwate-Miyagi Nairiku Earthquake of M7.2 in the neighboring area, *The 6th International Workshop on Statistical Seismology, April 12-16, 2009*, Granlibakken Conference Center, Lake Tahoe, CA, USA.

Kumazawa, T., Y. Ogata, and S. Toda (2009b), Seismicity changes in northern Tohoku District before the 2008 Iwate-Miyagi Nairiku Earthquake, *Rep. Coord. Comm. Earthq. Predict*., 74, 83–88, Tsukuba, Japan.

Kumazawa, T., Y. Ogata, and S. Toda (2009c), Seismicity changes in northern Tohoku District before the 2008 Iwate-Miyagi Nairiku Earthquake, *The 2009 Japanese Joint Statistical Meeting, September 10 (7-10), 2009*, Doshisha University, Kyoto, Japan..

Kumazawa, T., Y. Ogata, and S. Toda (2009d), Seismicity changes in northern Tohoku District before the 2008 Iwate-Miyagi Nairiku Earthquake, *The 2009 Seismological Society of Japan Meeting*, September 10 (7-10), 2009, Kyoto University, Kyoto, Japan.

Matu'ura R. S. (1986), Precursory quiescence and recovery of aftershock activities before some large aftershocks, *Bull. Earthq. Res. Inst*. Univ. Tokyo, 61, 1-65.

Naito, H., and S. Yoshikawa (1996), A *program to assist crustal deformation analysis, J. Seismol. Soc. Japan*., 52, 101-103.

NIED (2010), *Full range seismograph network* (F-net), http://www.fnet.bosai.go.jp/

Nishimura, T., S. Fujiwara, M. Murakami, M. Tobita, H. Nakagawa, T. Sagiya, and T. Tada (2001), The M6.1 earthquake triggered by volcanic inflation of Iwate volcano, northern Japan, observed by satellite radar interferometry, *Geophys. Res. Lett*., 28, 635-638.

Nishimura, T., S. Tanaka, T. Yamawaki, H. Yamamoto, T. Sano, M. Sato, H. Nakahara, N. Uchida, S. Hori, and H. Sato (2005), Temporal changes in seismic velocity of the crust around Iwate volcano, Japan, as inferred from analyses of repeated active seismic experiment data from 1998 and 2003, *Earth Planets Space*, 57, 491-505.

Ogata, Y., and K. Shimazaki (1984), Transition from aftershock to normal activity: The Rat Islands earthquake aftershock sequence, *Bull. Seismol. Soc. Am*., 74, 1757-1765.

Ogata, Y. (1988), Statistical models for earthquake occurrences and residual analysis for point processes, *J. Amer. Stat. Assoc*., 83, 9-27.

Ogata, Y. (1989), Statistical model for standard seismicity and detection of anomalies by residual analysis, *Tectonophysics*, 169, 159-174.

Ogata, Y. (1992), Detection of precursory relative quiescence before great earthquakes through a statistical model, *J. Geophys. Res*., 97, 19,845-19,871.

Ogata, Y. and K. Katsura (1993), Analysis of temporal and special heterogeneity of magnitude frequency distribution inferred from earthquake catalogues, *Geophys. J. Int* 113, 727-738.

Ogata, Y. (1999a), Increased probability of large earthquakes near aftershock regions with relative quiescence, *J. Geophys. Res.*, 106, B5, 8729-8744.

Ogata, Y. (1999b), Seismicity analysis through point-process modeling: A review, *Pure Appl. Geophys*., 155, 471-507.

Ogata, Y. (2001), Increased probability of large earthquakes near aftershock regions with relative quiescence, *J. Geophys. Res.*,106, B5, 8729-8744.

Ogata, Y., L. M. Jones, and S. Toda (2003), When and where the aftershock activity was depressed: Contrasting decay patterns of the proximate large earthquakes in southern California, *J. Geophys. Res.*, 108, B6, 2318, doi:10.1029/2002JB002009 (1-12).

Ogata, Yosihiko, Koichi Katsura and Masahara Tanemura (2003), Modelling heterogeneous space-time occurrences of earthquakes and its residual analysis, *Appl. Statist. 52, Part4, pp. 499-509*

Ogata, Y. (2004a), Space-time model for regional seismicity and detection of crustal stress changes, *J. Geophys. Res.*, 109, B03308, doi: 10.1029/2003JB002621.

Ogata, Y. (2004b), Seismicity quiescence and activation in western Japan associated with the 1944 and 1946 great earthquake near the Nankai Trough, *J. Geophys. Res*., 109, B04305, doi: 10.1029/2003JB002634.

Ogata, Y. (2005), Detection of anomalous seismicity as a stress change sensor, *J. Geophys. Res*. 110, B05S06, doi:10.1029/2004JB003245.

Ogata, Y. (2006a), Monitoring of anomaly in the aftershock sequence of the 2005 earthquake of M7.0 off coast of the western Fukuoka, Japan, by the ETAS model, *Geophys. Res. Let.*, 33, L01303, doi:10.1029/2005GL024405.

Ogata, Y. (2006b), Fortran programs statistical analysis of seismicity - updated version, (SASeis2006**)**, *Computer Science Monograph*, No. 33, The Institute of Statistical Mathematics, Tokyo, Japan (http://www.ism.ac.jp/editsec/csm/index_j.html)

Ogata, Y. (2007), Seismicity and geodetic anomalies in a wide preceding the Niigata-Ken-Chuetsu earthquake of 23 October 2004, central Japan, *J. Geophys. Res*., 112, B10301, doi: 10.1029/2006JB004697.

Ogata, Y. (2010), Space-time heterogeneity in aftershock activity, *Geophys. J. Int.*, **181**, 1575-1592, doi: 10.1111/j.1365-246X.2010.04542.x.

Ogata, Y., and S. Toda (2010), Bridging great earthquake doublets through silent slip: On- and off-fault aftershocks of the 2006 Kuril Island subduction earthquake toggled by a slow slip on the outer-rise normal fault the 2007 great earthquake, *J. Geophys. Res.*, doi:10.1029/2009JB006777, in press.

Ogata, Y. (2011), 東北地方太平洋沖地震の前震活動と広域的静穏化について 「地震予知連絡会会報」、2011年11月, 第86巻(3-20), pp.134-141.

Ogata, Y. and T. Kumazawa (2011), 東北地方太平洋沖地震の余震と連鎖地震 「地震予知連絡会会報」、2011年11月, 第86巻(3-19), pp.126-133.

Okada, Y. (1992), Internal deformation due to shear and tensile faults in a half-space, *Bull. Seism. Soc. Am*., 82, 1018-1040.

Ohta, Y., M. Ohzono, S. Miura, T. Iinuma, K. Tachibana, K. Takatsuka, K. Miyao, T. Sato, and N. Umino (2008), Coseismic fault model of the 2008 Iwate-Miyagi Nairiku earthquake detected by a dense GPS network, *Earth Planets Space,* 60, 1197-1201.

Ohtake, M., T. Matumoto, and G. V. Latham (1977), Seismicity gap near Oaxaca, southern Mexico as a probable precursor to a large earthquake. *Pure Apple. Geophys*., *115*, 375-385.

Research Group for Active Fault of Japan (1991), *Active Fault in Japan – Sheet Maps and Inventories* (revised edition), Tokyo University Press, 437pp.

Reasenberg, P. A., and R. W. Simpson, (1992), Response of regional seismicity to the static stress change produced by the Loma Prieta earthquake, *Science*, 255, 1687-1690.

Sekiya, H. (1976), The seismicity preceding earthquakes and its significance in earthquake prediction (in Japanese), *Zisin II* (*J. Seismol. Soc. Japan*), *29*: 299-312.

Simpson, R.W., and P.A. Reasenberg (1994), Earthquake-induced static-stress changes on central California faults, *U.S.G.S. Professional Paper* 1550-F, F55-F89.

Sykes, L. R., and S. C. Jaume (1990), Seismic Activity on Neighboring faults as a Long-term Precursor to Large Earthquakes in the San Francisco Bay Area, *Nature*, *348*: 595-599.

Takada, Y., T. Kobayashi, M. Furuya, and M. Murakami (2009), Coseismic displacement due to the 2008 Iwate-Miyagi Nairiku earthquake detected by ALOS/PALSAR: preliminary results, *Earth Planets Space,* 61, e9-e12.

Toda, S., and R. S. Stein (2002), Response of the San Andreas fault to the 1983 Coalinga-Nunez earthquakes: An application of interaction-based probabilities for Parkfield, *J. Geophys. Res*., 107(B6), 2126, doi:10.1029/2001JB000172.

Toda, S., and R. Stein (2003), Toggling of seismicity by the 1997 Kagoshima earthquake couplet: A demonstration of time-dependent stress transfer, *J. Geophys. Res*., 108, doi:10.1029/2003jb002527.

Toda, S., Stein, R.S., and Lin, J. (2011), Widespread seismicity excitation throughout central Japan following the 2011 M=9.0 Tohoku earthquake, and its interpretation in terms of Coulomb stress transfer

Tsuruoka, H. (1996), Development of seismicity analysis software on workstation (in Japanease), *Tech. Res. Rep*. 2, pp. 34-42, Earthq. Res. Inst., Univ. of Tokyo, Tokyo

Utsu, T. (1968), Seismic activity in Hokkaido and its vicinity (in Japanese). *Geophys. Bull. Hokkaido Univ.*, 13, 99-103.

Ueki, S. and S. Miura (2002), Volcanic and Seismic Activities Observed around Iwate Volcano in 1998. *Journal of Geography* (in Japanease), 111(2) 154-166.

Utsu, T., Y. Ogata, and R. S. Matsu'ura (1995), The centenary of the Omori formula for a decay law of aftershock activity, *J. Seismol. Soc. Japan*., 7, 233-240.

Utsu, T., and Y. Ogata (1997), Statistical Analysis of point processes for Seismicity (SASeis), *IASPEI Software Library*, vol.6, pp. 13-94, Int. Assoc. Seismol. Phys. Earth's Inter., Trieste, Italy.

Wyss, M., and R. O. Burford (1987), Occurrence of a predicted earthquake on the San Andreas fault, *Nature*, *329*: 323-325.